LEVEL II

12 SC

SYSTEMS, SCIENCE AND SOFTWARE

SSS-R-78-3653

ANALYSIS OF EXPLOSION GENERATED SURFACE WAVES IN AFRICA, RESULTS FROM THE DISCRIMINATION EXPERIMENT AND SUMMARY OF CURRENT RESEARCH

W. L. Rodi
J. M. Savino
T. G. Barker
S. M. Day
T. C. Bache

Quarterly Technical Report
For Period January 1 - March 31, 1978

Sponsored by
Advanced Research Projects Agency
ARPA Order No. 2551

This research was supported by the Advanced Research Projects Agency of the Department of Defense and was monitored by AFTAC/VSC, Patrick Air Force Base, Florida, 32925, under Contract No. F08606-76-C-0041.

April 1978

P. O. BOX 1620, LA JOLLA, CALIFORNIA 92038, TELEPHONE (714) 453-0060

AFTAC Project Authorization No. VELA/T/7712/B/ETR

ARPA Order 2551, Program Code 8F10

Effective Date of Contract: October 1, 1976

Contract Expiration Date: September 30, 1978

Amount of Contract: $435,087

Contract No. F08606-76-C-0041

Principal Investigator and Phone No.
Dr. Thomas C. Bache, (714) 453-0060, Ext. 337

Project Scientist and Phone No.
Captain Michael J. Shore, (202) 325-7581

Unclassified

SECURITY CLASSIFICATION OF THIS PAGE (When Data Entered)

REPORT DOCUMENTATION PAGE

READ INSTRUCTIONS BEFORE COMPLETING FORM

1. REPORT NUMBER	2. GOVT ACCESSION NO. / 3. RECIPIENT'S CATALOG NUMBER
(9) Quarterly rept. 1 Jan - 31 Mar 78	
4. TITLE (and Subtitle) (6) ANALYSIS OF EXPLOSION GENERATED SURFACE WAVES IN AFRICA, RESULTS FROM THE DISCRIMINATION EXPERIMENT AND SUMMARY OF CURRENT RESEARCH.	5. TYPE OF REPORT & PERIOD COVERED: Quarterly Report 1-1-78 to 3-31-78
	6. PERFORMING ORG. REPORT NUMBER: (14) SSS-R-78-3653
7. AUTHOR(s) (10) W. L. Rodi, S. M. Day, J. M. Savino, Thomas C. Bache, T. G. Barker,	8. CONTRACT OR GRANT NUMBER(s): (15) F08606-76-C-0041
9. PERFORMING ORGANIZATION NAME AND ADDRESS: Systems, Science and Software, P. O. Box 1620, La Jolla, California 92038	10. PROGRAM ELEMENT, PROJECT, TASK AREA & WORK UNIT NUMBERS: ~~Program Code No. 8F10~~ ARPA Order No. 2551
11. CONTROLLING OFFICE NAME AND ADDRESS: VELA Seismological Center, 312 Montgomery Street, Alexandria, Virginia 22314	12. REPORT DATE: (11) Apr 1978
	13. NUMBER OF PAGES: 92
14. MONITORING AGENCY NAME & ADDRESS (if different from Controlling Office): (12) 101 p.	15. SECURITY CLASS. (of this report): Unclassified
	15a. DECLASSIFICATION DOWNGRADING SCHEDULE

16. DISTRIBUTION STATEMENT (of this Report)

Approved for Public Release; Distribution Unlimited.

17. DISTRIBUTION STATEMENT (of the abstract entered in Block 20, if different from Report)

18. SUPPLEMENTARY NOTES

19. KEY WORDS (Continue on reverse side if necessary and identify by block number)

Seismic Surface Waves
Seismic Discrimination
Nuclear Explosion Seismology

78 11 06 101

20. ABSTRACT (Continue on reverse side if necessary and identify by block number)

Brief summaries of work currently underway or recently completed during the period from 1 January 1978 to 31 March 1978 are given in four topic areas: Source Studies, Data Analysis, Surface Wave Studies and Body Wave Studies.

The remainder of the report presents research results not previously reported from four research projects. The first is entitled "Discrimination Experiment - Digital short-

DD FORM 1 JAN 73 1473 EDITION OF 1 NOV 65 IS OBSOLETE

388507

Unclassified (over) 4/6

SECURITY CLASSIFICATION OF THIS PAGE (When Data Entered)

20. ABSTRACT (continued)

and long-period body and surface wave data for Eurasian events recorded at a global network of stations are being provided for event discrimination. Efforts to date have focused on the application of the VFM (variable frequency magnitude) discriminant to the short period P waves at four stations. Thirteen events have been analyzed and tentative identification has been made.

The second project is entitled, "Analytic Continuation of the Elastic Field from a Complex Source in a Halfspace." We present the mathematical development of a method for linking finite difference numerical source calculations in a halfspace with analytical techniques for propagating elastic waves in layered media.

The third detailed discussion, "Theoretical Computation of Lg," is concerned with the theoretical generation of Lg in a continental earth model. Synthetic seismograms are shown for several ranges and source depths. The fourth topic is, "Analysis of Surface Waves from the French Test Site in the Sahara." For an underground explosion in Algeria surface wave recordings from five stations in or near Africa were analyzed to determine the phase and group dispersion. Using formal linear inversion, these data were inverted to obtain preliminary models for the crust and upper mantle along the five paths. Using these models, synthetic seismograms were computed and were found to be in good agreement with the observations at most of the stations.

TABLE OF CONTENTS

TABLE OF CONTENTS (continued)

LIST OF ILLUSTRATIONS

LIST OF ILLUSTRATIONS (continued)

LIST OF ILLUSTRATIONS (continued)

LIST OF TABLES

I. INTRODUCTION AND SUMMARY

1.1 BACKGROUND

The objective of the Systems, Science and Software (S^3) research program is to examine the parameters that affect the seismic signals from underground explosions and earthquakes. Attention is primarily directed to those features of the seismic waveforms that discriminate between the two classes of events and that reliably indicate the explosion yield. Current research includes empirical studies of the available data, time signal analysis, and the development and application of theoretical and numerical methods for modeling earthquakes and explosions. Emphasis is on the last of these. In particular, we are applying techniques for theoretically simulating the far-field signatures of simple and complex seismic sources.

This report summarizes the work done during the sixth three-month period of the current contract.

1.2 SUMMARY OF RESEARCH DURING THIS QUARTER

Our work during this quarter has included research in a number of areas. Research projects currently underway or completed during the quarter are briefly summarized below.

Source Studies

A. Analysis of Small-Scale Explosions in Grout

A final report, SSS-R-77-3349, "Seismic Ground Motion from Free-Field and Underburied Explosive Sources," by J. T. Cherry, T. G. Barker, S. M. Day and P. L. Coleman was submitted during this quarter. The abstract is reproduced below:

Small-scale laboratory experiments were conducted and analyzed to study the effect of the proximity of the free

surface on the seismic ground motions. Two classes of experiments were done. In one the charges were far from the free-surface and the free-field displacement-time histories were measured. In the second class the charges were near the surface and were either fully contained or formed a crater. The charges were 0.25 g of PETN in concrete cylinders, 120 cm in diameter and 33 to 60 cm thick. In all experiments displacements were measured 30.5 cm directly below the charges. The experiments produced consistent and repeatable data. A striking feature of the ground motions for the near surface experiments is a large long-period negative pulse which is present whether or not cratering occurred.

The results were studied by comparing to numerical simulations of the experiments using a Lagrangian finite difference program and published properties of the concrete and PETN. The calculations are in good agreement with the laboratory data, providing verification of both the constitutive models and the methods.

The large, long-period negative pulse can be explained in the context of linear elasticity. It is due to the near-field interaction of the spherical wave front with the free surface. Therefore, it does not propagate to the far-field and is not important for teleseismic magnitudes.

B. Analysis of Decoupling Calculations Done by Applied Theory, Inc. (ATI)

A topical report SSS-R-78-3627, "Analysis of Two Decoupled Explosion Simulations" by T. C. Bache and J. F. Masso was submitted in draft form in April. The abstract is reproduced below:

Two axisymmetric ground motion calculations were carried out by Applied Theory, Inc. to simulate 25 kt decoupled nuclear explosions in mined cavities in salt. One cavity was spherical

with a radius of 66 meters while the other was a 3/1 aspect ratio ellipsoid of revolution. Both had the same volume. Results of the two calculations were analyzed to determine the character of the teleseismic body and surface waves.

The spherically symmetric portion of the field is slightly (20 to 25 percent) smaller for the spherical cavity. Comparing to results of tamped explosions, the decoupling factor for this case is about 140 at one Hertz. The radiation from the ellipsoidal cavity is substantially perturbed from spherical symmetry; the maximum S wave amplitudes are nearly three times as large as maximum P wave amplitudes at 1.0 Hz. However, theoretical body and surface wave seismograms indicate that the m_b and M_s values are not substantially different for the two cavities.

C. Transmitting Boundary for Finite Difference Calculations

We have recently implemented a transmitting boundary condition for finite different stress wave calculations, based on paraxial approximations to the wave equation given in, for example, Engquist and Majda (1977) and Clayton and Engquist (1977). Our approach has been to first separate the field near the boundary into its irrotational and solenoidal components, and then to apply a second order paraxial approximation to each of these components. The method has been tested for two-dimensional plane boundaries and has been found to be quite satisfactory for transmitting the P wave and the initial S wave arrival. However, boundary displacement suffers from a spurious drift at late time. The size of the late-time drift is sensitive to details of the difference scheme used. After much experimentation, we believe we have minimized its contribution for the second-order approximation. Higher order approximations may be required to remove its effect.

The method has not yet been extended to curved boundaries like those parallel to the axis in axisymmetric problems. We plan to attempt this extension. We also plan to test the method for three-dimensional grids.

D. Earthquake Modeling on the ILLIAC IV Computer

A three-dimensional finite different program for modeling earthquake faulting has been made operational on the ILLIAC IV computer. The current version is capable of handling a bilateral fault in a homogeneous medium. Our initial set of calculations is designed to study the importance of plastic material behavior on the fault zone and determine the scaling of the radiation field with the fault parameters.

The first calculation was completed during this quarter. This is for a 3 km x 3 km bilateral fault in a linear elastic space. The output tapes were sent to S^3 where they were read and selected quantities were plotted. Considerable effort was required to develop the software to convert and plot these data tapes.

Unfortunately, detailed analysis of the output revealed some strange behavior in a region of the fault plane that was eventually traced to a coding error. The calculation is being repeated. Processing of output data from this and subsequent calculations will be much easier due to the availability of the recently developed software.

E. Representation Theorem for Analytic Continuation of Finite Difference Source Calculations

This work is summarized in Section 1.4 and described in detail in Section III.

F. One-Dimensional Source Calculations

One-dimensional source calculations done at S^3 in the past were initiated with a rock-gas filled cavity at the

vaporization radius (approximately 70 metric tons of rock are vaporized per kiloton yield). An ideal gas equation of state was used. We have recently developed complete state equations for tuff and granite, valid up to many megabars, so the calculation can be initiated at the wall of the original cavity. These equations of state give a more realistic cavity driving pressure over the entire time of the calculation. Results from the old and new methods for handling the cavity region are being compared.

With a complete equation of state we can compute the decoupling effect of varying the initial radius of an air filled cavity. We are currently beginning a series of decoupling calculations in granite, tuff and salt. These calculations will also use a better one-dimensional treatment of the overburden pressure than was used in previous calculations.

Data Analysis

A. Discrimination Experiment

This work is summarized in Section 1.3 and described in detail in Section II.

B. Development of Spectral m_b and M_s

The variable frequency magnitude (VFM) discriminant being applied in the discrimination experiment (see Section II) is based on the use of narrow band filter magnitudes, called $\overline{m}_b(f)$. These magnitudes reflect the amplitude of the arriving energy at a particular period and a particular arrival time. In essence, they represent the spectral energy of a specific phase arrival. We have long recognized that measurements of this kind might provide a more convenient, stable and reliable signal amplitude indicator than the conventional m_b.

A set of HNME recordings of eleven Pahute Mesa recordings was provided in digital form and is being examined to test the utility of the $\overline{m}_b(f)$. A similar value, $\overline{M}_s(f)$, is defined for the surface waves. Single frequency values are no improvement on the conventional time domain magnitudes. However, $\hat{m}_b(f)$ and $\hat{M}_s(f)$ values defined by averaging the $\overline{m}_b(f)$ and $\overline{M}_s(f)$ over a frequency band are very attractive in terms of such qualities as the scatter when plotted versus yield. We are continuing to evaluate this measurement and will report the results to VSC in the near future.

Surface Wave Studies

A. Analysis of Surface Waves from the French Test Site in the Sahara

This work is summarized in Section 1.6 and described in detail in Section V.

B. Surface Wave Amplitudes of NTS Explosions Recorded at ALQ and TUC

In previously published work (Bache, Rodi and Harkrider, 1978) we presented crustal models for the NTS-ALQ and NTS-TUC paths that lead to synthetic seismograms that closely match the observations. The amplitudes of the synthetics can then be used, together with the theory, to deduce the long period levels of the source functions for NTS explosions. This work is nearly complete and a report describing the results is in preparation.

C. Theoretical Study of the Lg Phase

This work is summarized in Section 1.5 and described in detail in Section IV.

Body Wave Studies

In the section on "Data Analysis" we mentioned the set of eleven HNME recordings of Pahute Mesa explosions that are being used to test the development of newly defined magnitude measures. These data are also being analyzed with synthetic seismogram methods to isolate the different effects contributing to m_b-log yield and M_s-log yield relations. An important feature of the body wave recordings is a depth-dependent phase that arrives after pP. This may be due to spall slapdown, tectonic release or some other cause. More complex synthetic seismograms are being studied to determine the origin and nature of this phase. We need to learn how to model it for body waves to estimate its effect on the surface wave recordings.

1.3 SUMMARY OF SECTION II: "DISCRIMINATION EXPERIMENT"

During this reporting period, we received digital short- and long-period body and surface wave data for nineteen Eurasian events recorded at a global network of seismic stations. Our initial efforts at event discrimination have focused on the application of narrow-band filtering techniques to the short-period P waves recorded at four of the stations in the network. These four stations are located at epicentral distances between 16 and 98 degrees from the events.

Tentative identifications of thirteen of the larger events are as follows: earthquakes - events 47 and 49; explosion-like events 1, 14, 16, 17, 18, 19, 20, 21, 22, 33 and 53. The event locations are described in Figure 1 and Table 1 of Section II. More definitive results must await the receipt and analysis of additional events and the determination of the extent of the earthquake and explosion populations in the $\overline{m}_b(f)$ plane at each of the reporting stations.

1.4 SUMMARY OF SECTION III: "ANALYTIC CONTINUATION OF THE ELASTIC FIELD FROM A COMPLEX SOURCE IN A HALFSPACE"

An important problem in computing theoretical seismograms for complex deterministic source models is the development of methods for linking the finite difference numerical source models with efficient analytical techniques for propagating elastic waves in layered earth models. When the source is in a homogeneous whole space, accurate techniques are available and have been extensively used at S^3. However, the problem is much harder when there are material interfaces in the source region. In particular, there is a great need for an analytic continuation method for source calculations including the free surface in the source region.

In Section III we outline mathematically an analytic continuation method for a source in a layered halfspace. The method is based on an elastodynamic representation theorem and requires integration of a series of terms involving products of the source generated displacements and tractions with Green's functions representing the elastic response of the medium. The method is now being programmed for computing the body waves at arbitrary range in a plane-layered earth model. The extension to surface waves is straightforward.

1.5 SUMMARY OF SECTION IV: "THEORETICAL COMPUTATION OF Lg"

A brief study of the excitation of the regional phase Lg was conducted at VSC request using a continental earth model provided by VSC. Theoretical Lg phases are associated with stationary phases of the higher mode Rayleigh and Love waves which occur at about 3.5 km/sec in continental structures. Synthetic seismograms illustrating the Lg phase for several source depths and ranges are presented in Section IV. Unfortunately, the structure near the surface is much too simple to give realistic synthetic seismograms. The synthetics are dominated by a nearly undispersed pulse associated with the fundamental mode Rayleigh and Love wave.

1.6 SUMMARY OF SECTION V: "ANALYSIS OF SURFACE WAVES FROM THE FRENCH TEST SITE IN THE SAHARA"

Surface wave recordings from seismometer stations in or near Africa were used to study the French underground nuclear explosion SAPHIRE (27 February 1965) with the objective being to determine the source characteristics of this event. Our first step is to accurately account for the path effects by inverting the observed dispersion to determine average crustal models for the five paths studied. Models fitting Rayleigh wave phase and group velocities were inverted for each path. In addition, Love wave group velocities were simultaneously inverted for two of the five paths. The fit to the observed data is excellent for all but one path where the Love and Rayleigh wave group velocities cannot be fit simultaneously. The inversion models are smooth and give profiles for the crust and upper mantle that are consistent with data from other sources. These models are preliminary in the sense that they have not yet been integrated to give a consistent picture of the structure in northern Africa. This is the next step which is necessary before considering our models to be our final estimates for this region.

The inversion models were used together with a simple source to compute theoretical seismograms for the SAPHIRE event. These seismograms agree very well with the observations at several of the stations, but there is significant disagreement at the east African stations in Ethiopia and Kenya. The problem may be with the path models, the source representation or the anelastic attenuation (Q) model used. These questions require further study. After completing our path model specification, we will use the comparison of synthetic and observed seismograms to infer the long period source characteristics.

II. DISCRIMINATION EXPERIMENT

2.1 INTRODUCTION

Our objective in the discrimination experiment is to analyze seismic waveforms from a large population of Eurasian events in order to identify these events as either earthquakes or explosions. The waveforms that we are concentrating on are short-period P waves recorded by a global network of seismograph stations. In this section of the report we will summarize the work that has been performed to date on this experiment.

2.2 DESCRIPTION OF DATA

As of the end of this reporting period we had received multi-station short- and long-period digital magnetic tape data for nineteen Eurasian events. The event locations are shown in Figure 1 and their dates, origin times and epicentral coordinates, as supplied by Teledyne Geotech, are listed in Table 1. These events are well distributed throughout the Eurasian study region, from Kamchatka and the Kuril Islands in the east to the Caspian Sea in the west. The locations of eight of the Eurasian stations contributing data for this experiment are also indicated on Figure 1.

Upon receipt, the magnetic tapes are converted to a format more convenient for use on the UNIVAC 1108 computer. Once the tape conversion process has been completed, plots of the short-period P wave seismograms are generated for those event-station pairs that are not included in the sets of Xerox copies of seismograms supplied by Geotech. These analog recordings are necessary for culling the data and defining the duration of signal and noise windows. Examples of P-wave seismograms recorded at six different stations for event 19 are shown in Figure 2. As can be seen, the duration

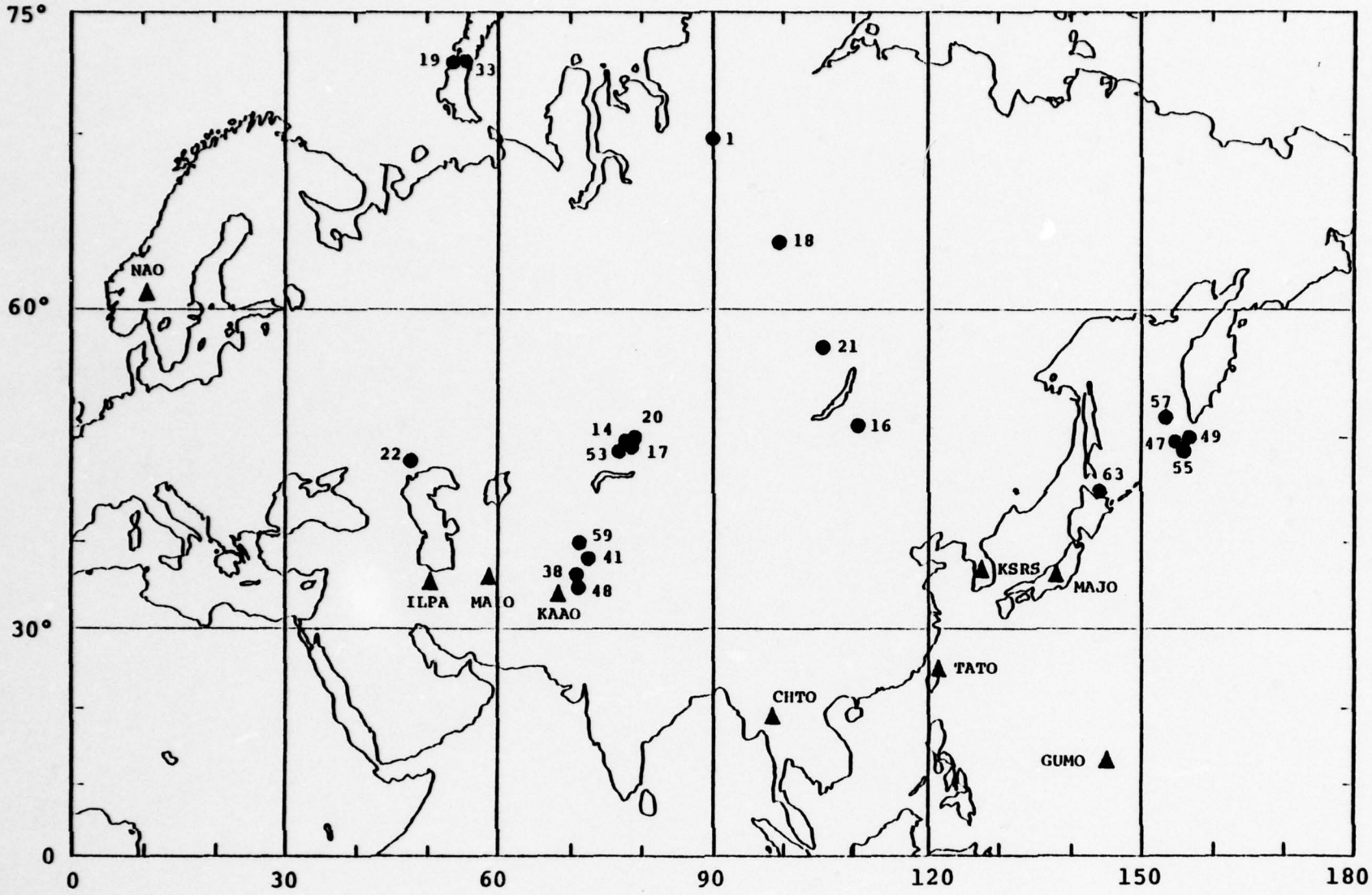

Figure 1. Map of Eurasia showing locations of events and several of the stations included in the discrimination experiment.

TABLE 1

EVENT LOCATION INFORMATION

Event Number	Date Yr	Mo	Dy	Origin Time Hr:Mn:Sec	Coordinates Latitude (°N)	Longitude (°E)
1	77	07	26	16:59:59.9	69.4	90.4
14	77	07	30	01:56:59.9	49.7	78.2
16	77	08	10	22:00:00.7	50.9	111.0
17	77	08	17	04:26:59.8	49.8	78.2
18	77	08	20	22:00:00.6	64.1	99.8
19	77	09	01	03:00:00	73.0	54.0
20	77	09	05	03:03:00	50.0	78.9
21	77	09	10	16:00:00	57.0	106.0
22	77	09	30	06:59:00	48.0	48.0
33	77	10	09	11:00:00	73.0	55.0
38	77	10	16	15:02:49	36.9	71.5
41	77	10	13	20:38:42	38.1	72.8
47	77	10	16	21:05:35	49.7	155.1
48	77	10	19	05:02:00	36.3	71.3
49	77	10	19	21:20:37	49.5	155.4
53	77	10	29	03:07:00	49.0	78.0
55	77	10	26	05:38:52	49.0	155.8
57	77	10	26	13:14:30	51.5	153.4
59	77	10	28	21:15:11	39.8	71.9

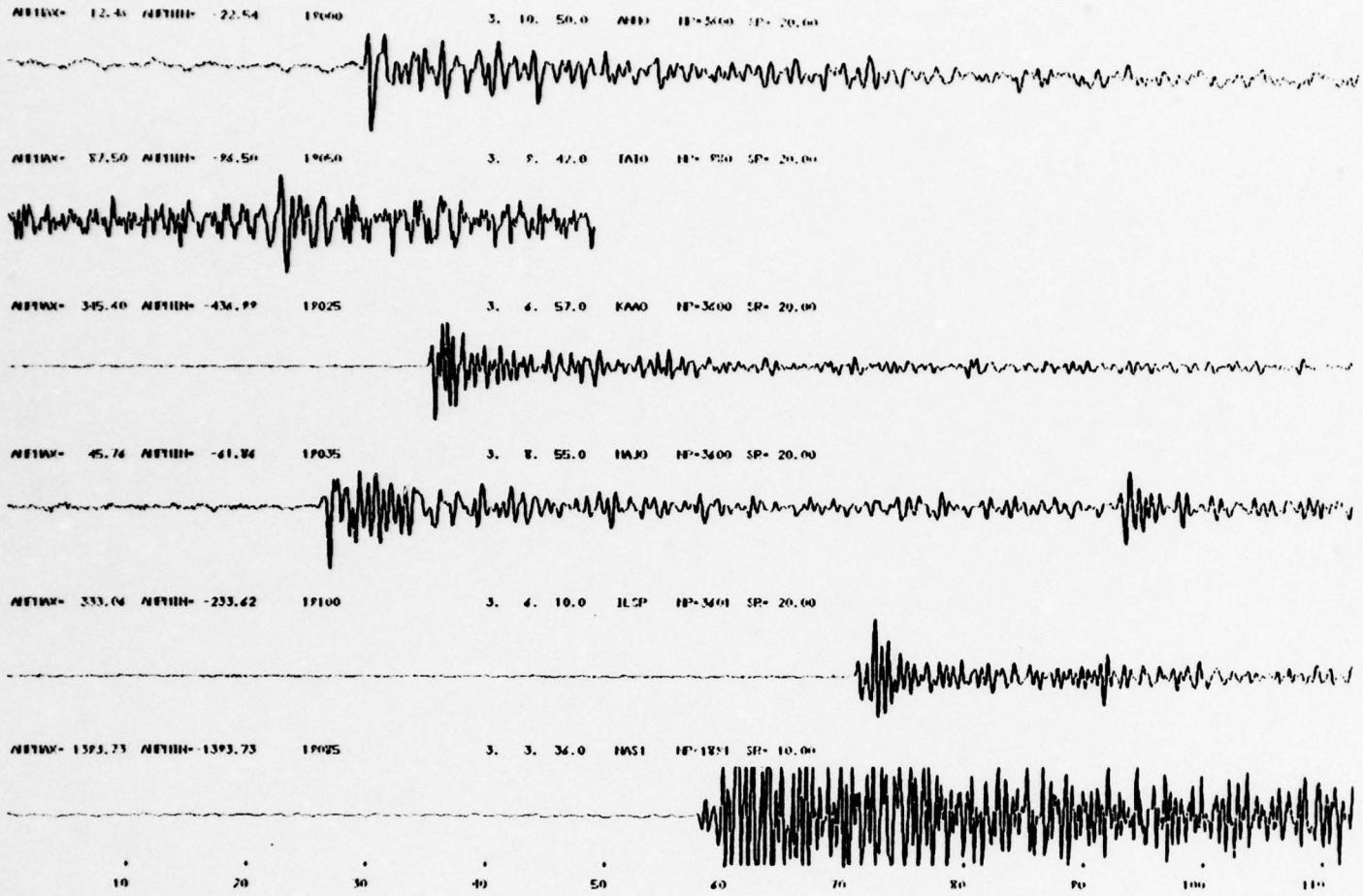

Figure 2. Short-period P-wave seismograms for event 19 recorded at several of the stations included in the discrimination experiment.

of noise preceding these signals is quite variable, ranging from about 20 seconds at TATO (19050) to 70 seconds at ILPA (19100). In addition, these analog playouts help us avoid all or portions of seismograms that contain bad data (clipped signals, digital drop-outs, etc.), such as the NORSAR recording (19085) at the bottom of Figure 2.

2.3 ANALYSIS PROCEDURE

The variable frequency magnitude discriminant, as proposed by Archambeau, et al., (1974) and developed by Savino and Archambeau (1974), is the technique that will be used to identify the Eurasian events in this experiment. The variable frequency magnitudes are outputs of the MARS computer program.

The central feature of the MARS signal analysis program is the use of narrow band frequency filters to break up or decompose a time series consisting of signal plus noise into a set of quasi-harmonic modulated "signals". This set of filtered signals, one for each filter center frequency, can then be used to determine the energy arrival time (the group time, t_g) and amplitude of the signal for each center frequency by analysis of the time modulation of the filter outputs.

Figure 3 summarizes the flow of operations in the MARS program: Figure 3a provides a verbal outline; Figure 3b presents the key mathematical operations performed in this program.

Seismic data are read into the program in the form of time series (Figures 3a and 3b) generally of about 500 to 2000 points in length. The data are then optionally detrended, demeaned and tapered. The program then selects the smallest power of two which is greater than the number

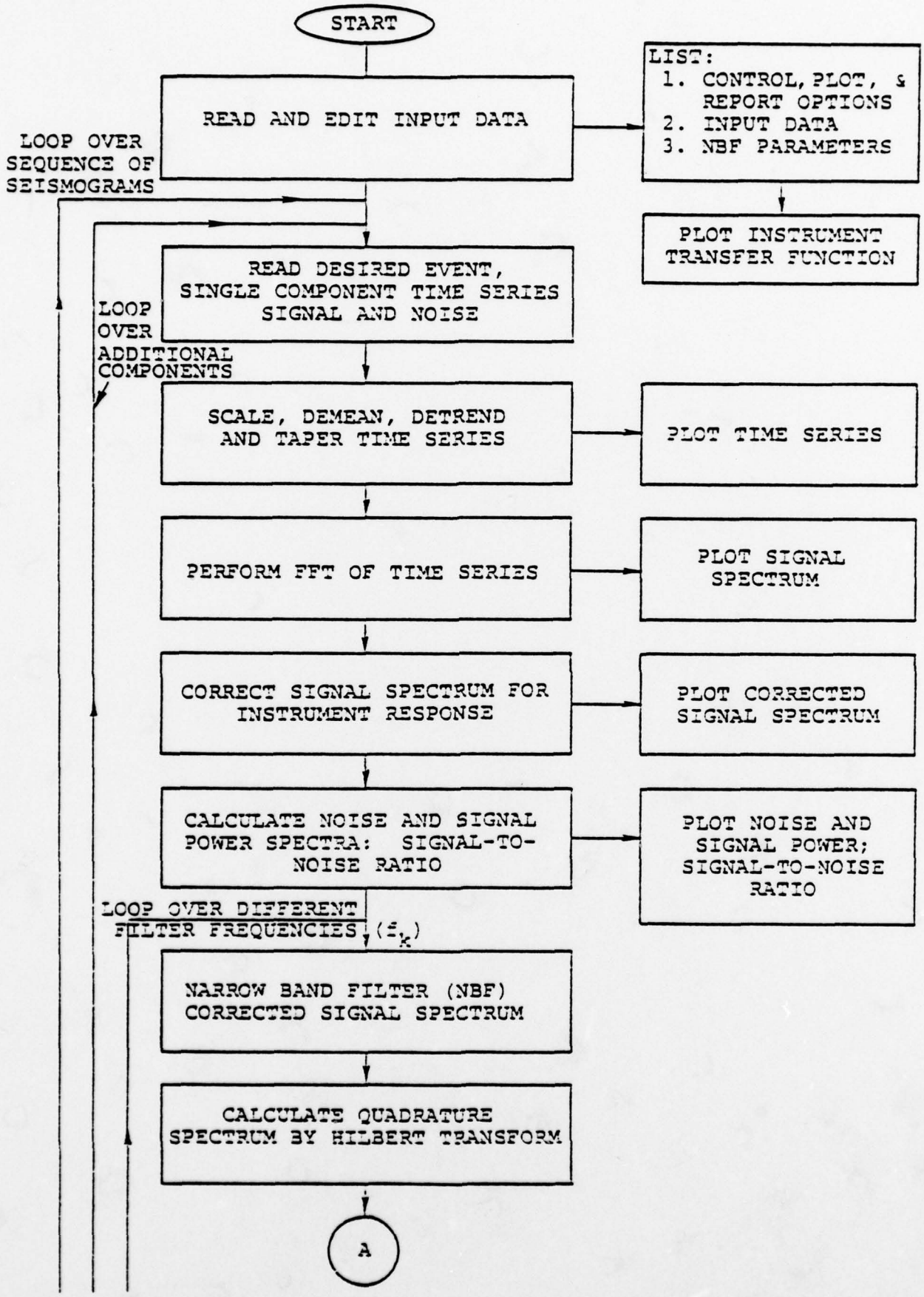

Figure 3a. MARS flowchart.

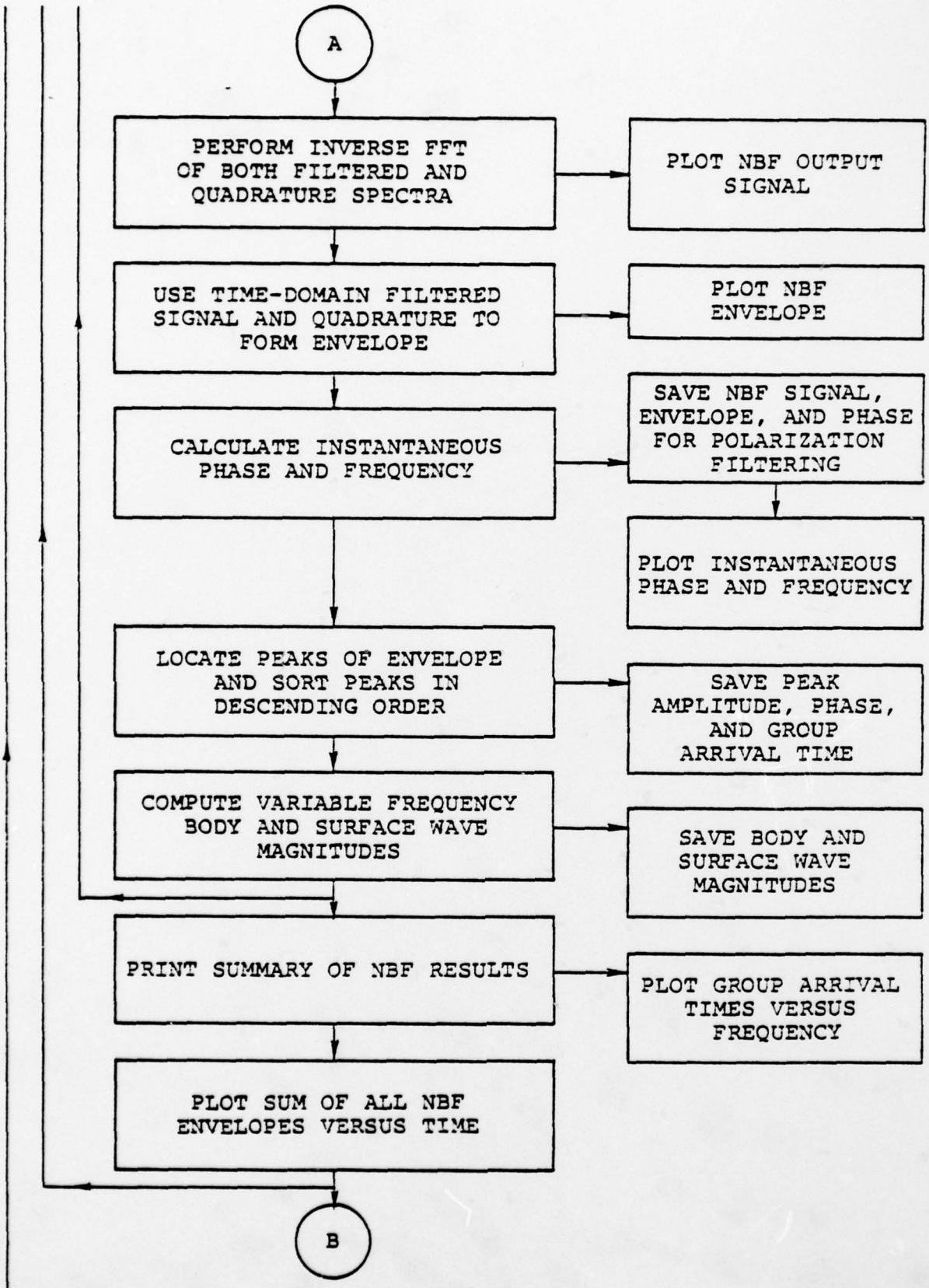

Figure 3a. (continued)

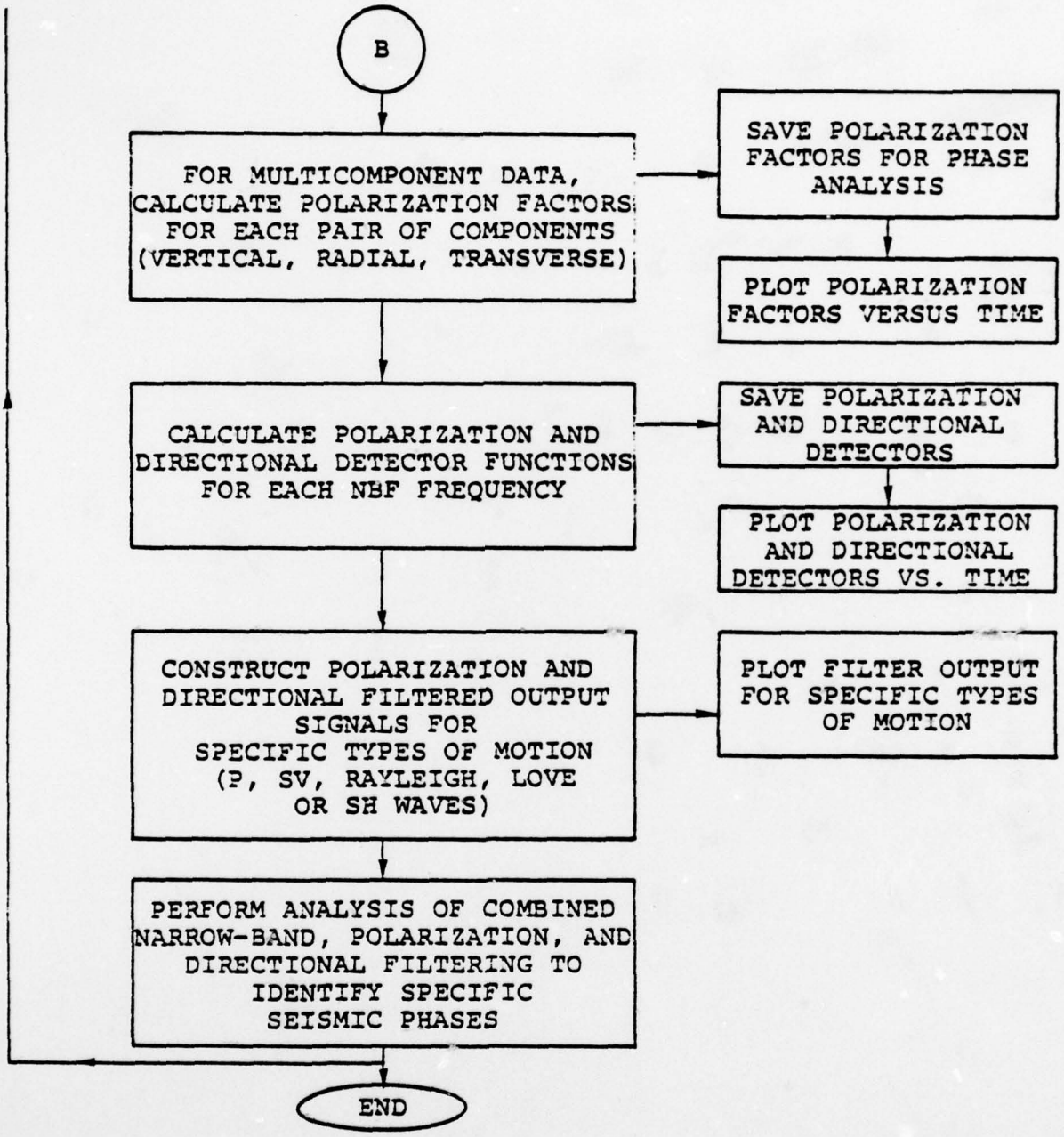

Figure 3a. (continued)

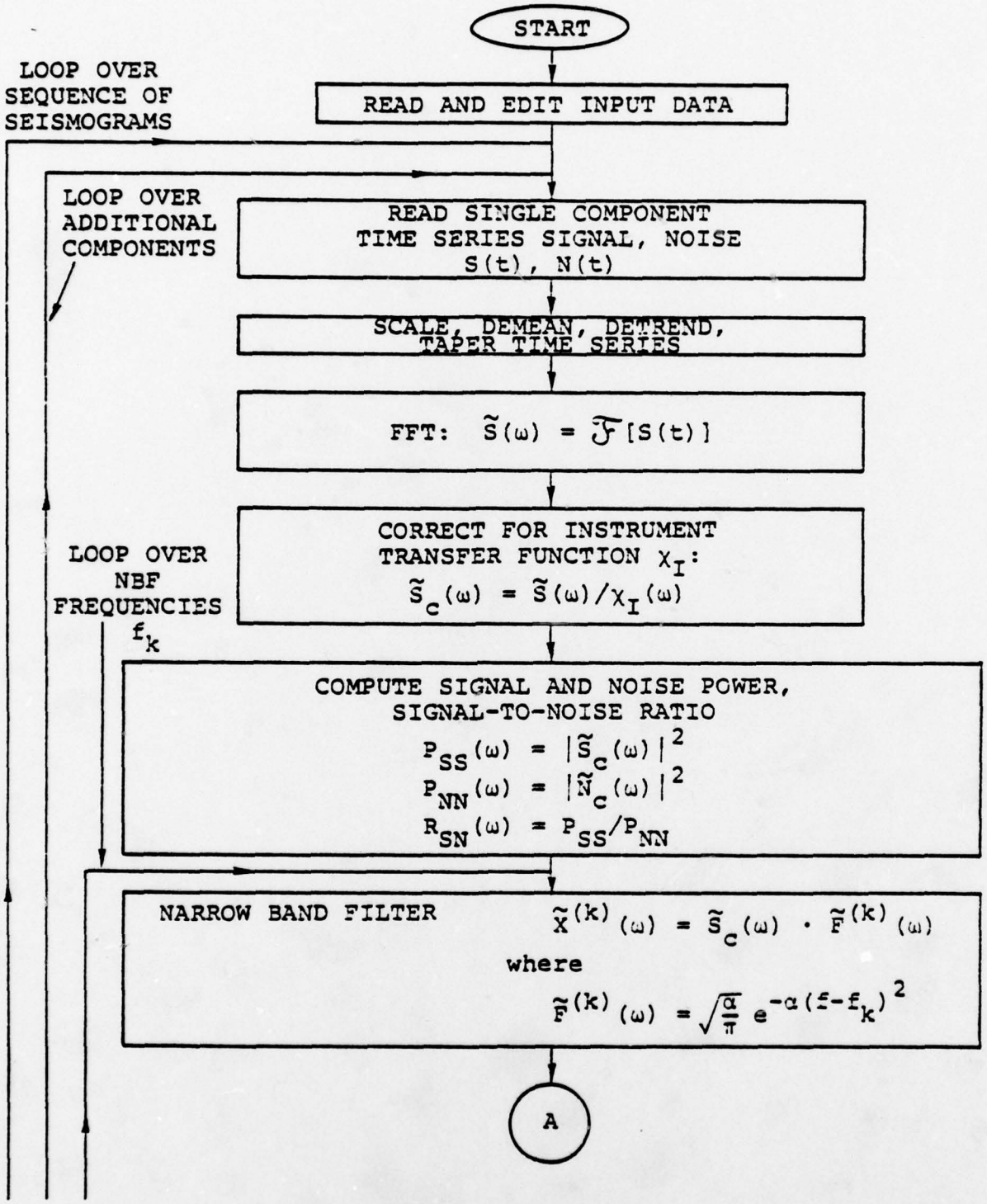

Figure 3b. Flowchart indicating principal mathematical operations in the MARS program.

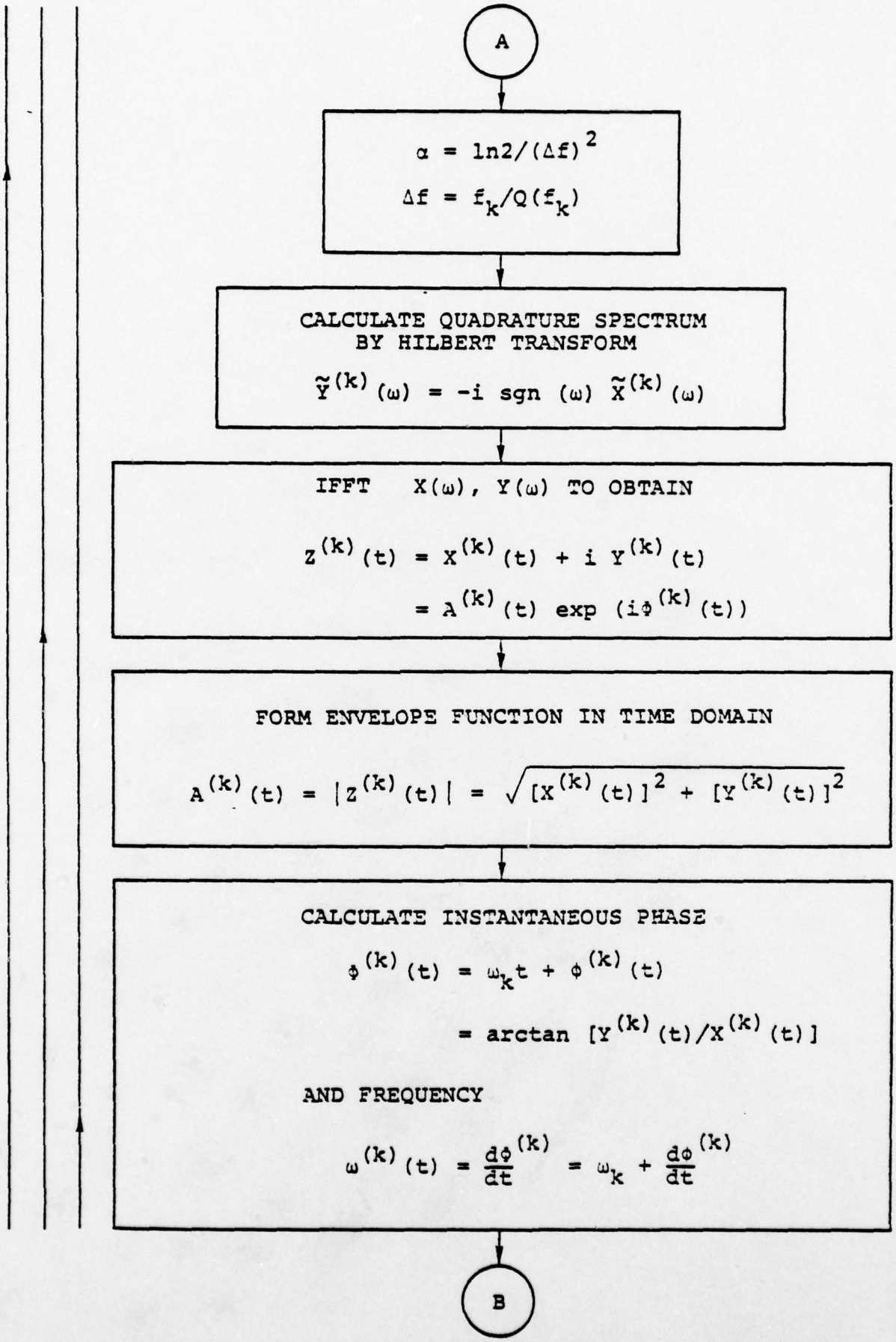

Figure 3b. (continued)

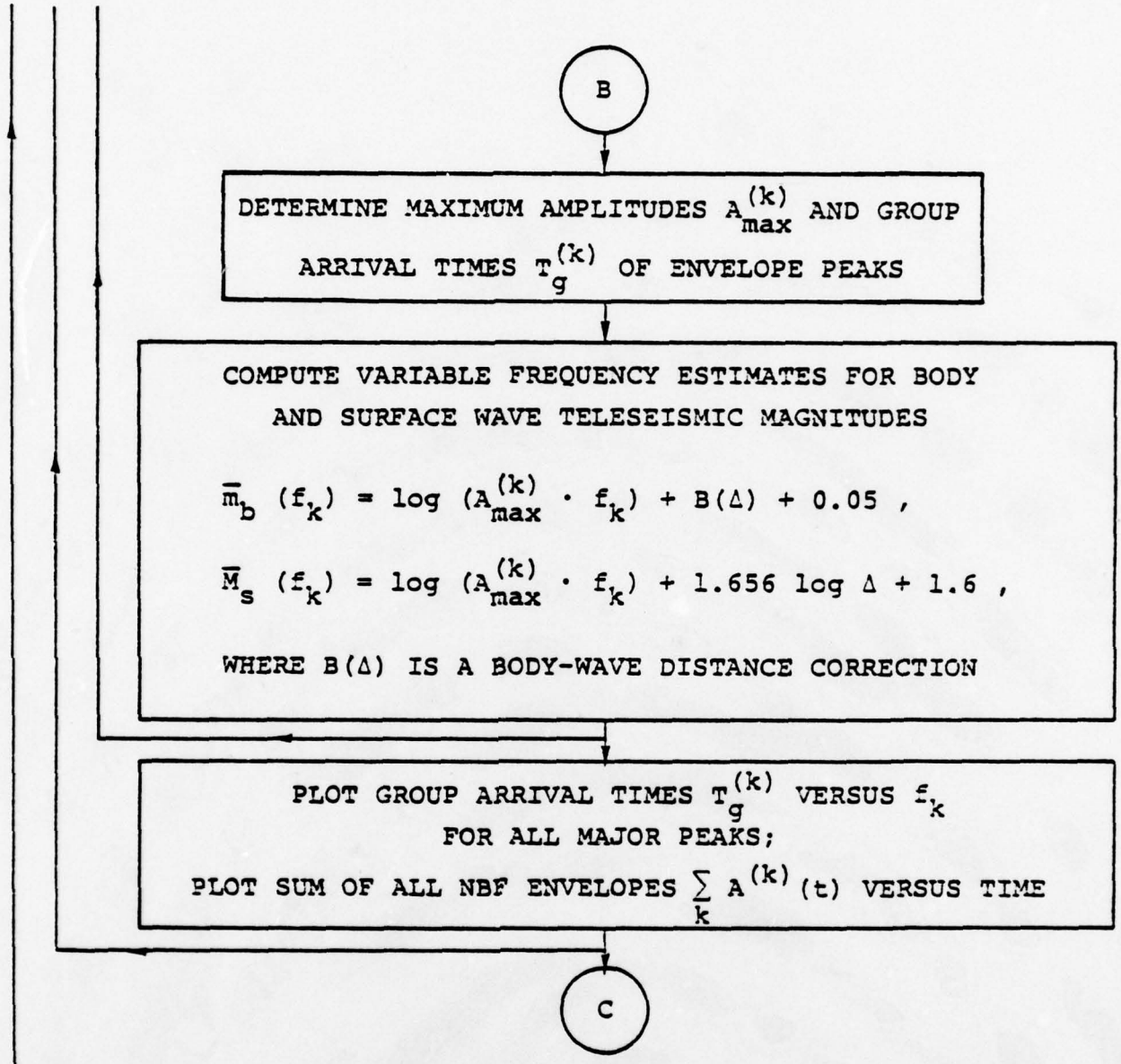

Figure 3b. (continued)

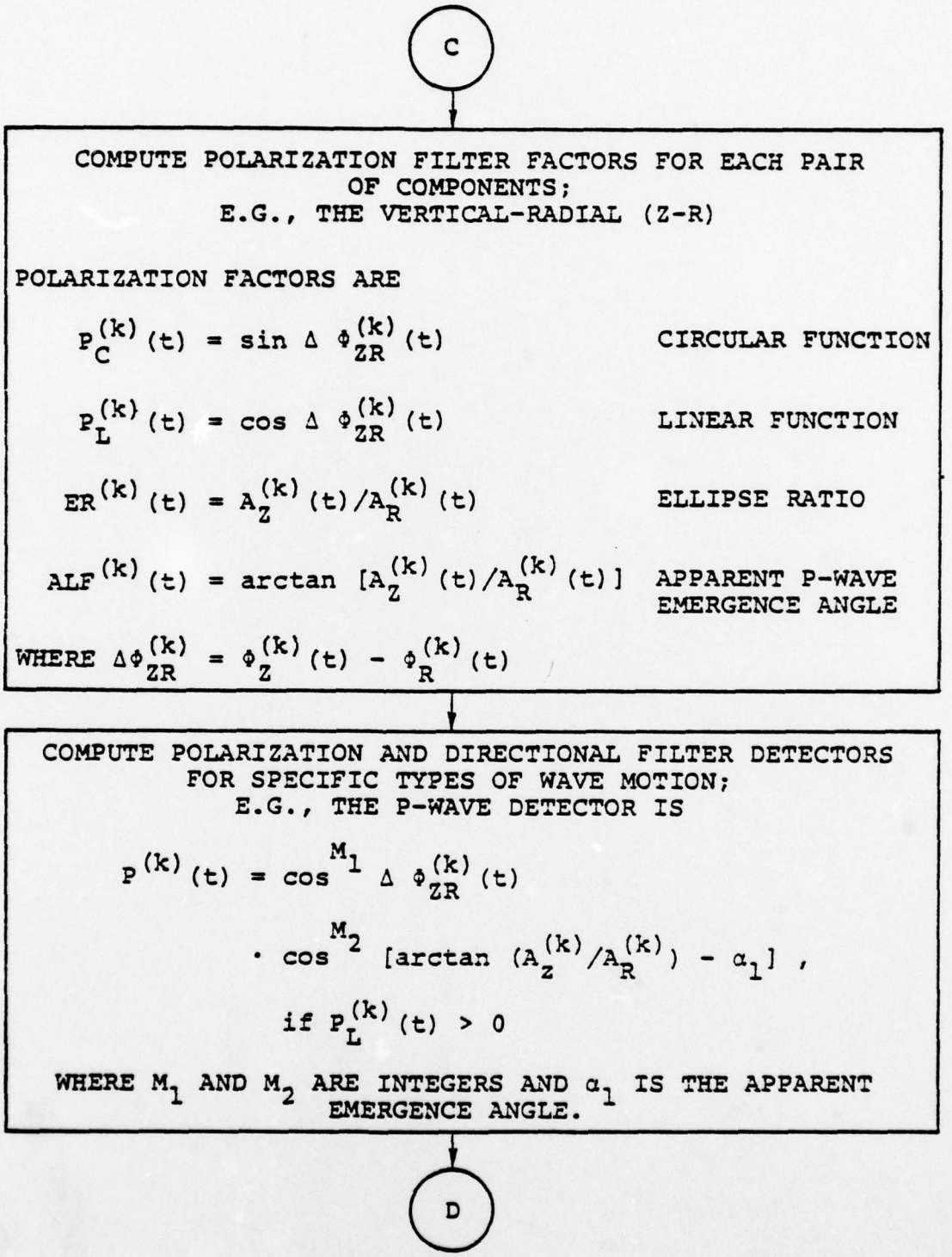

Figure 3b. (continued)

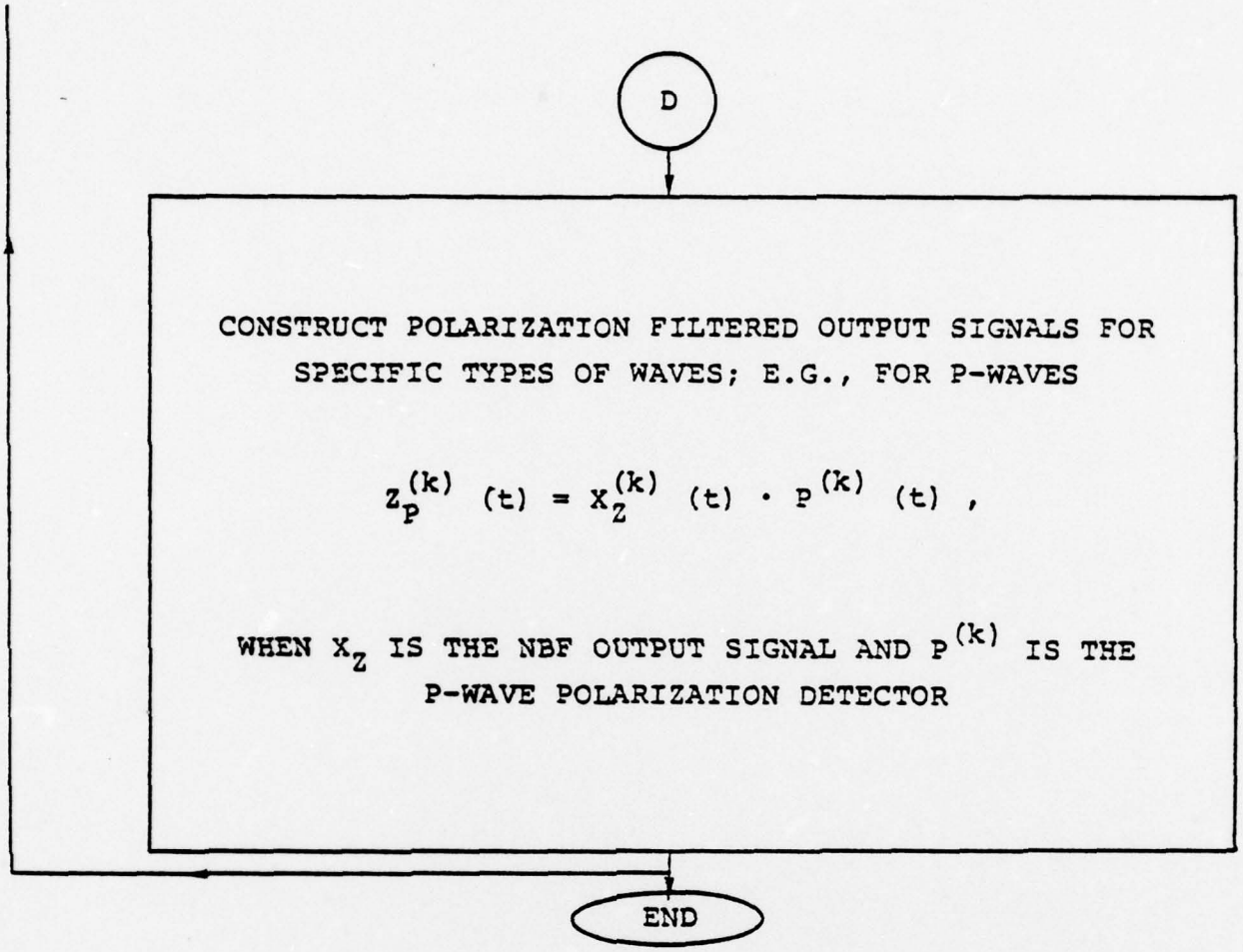

Figure 3b. (continued)

of points input and performs a discrete Fourier transform using the Cooley-Tukey algorithm. Both the original time series and the spectrum are then plotted.

Referring to Figures 3a and 3b, the signal is next filtered in the frequency domain by multiplication by a narrow band Gaussian-shaped filter. This particular filter form is selected to satisfy two goals: (1) minimum width in the frequency domain, and (2) maximum ripple suppression in the time domain. As a consequence of the sampling theorem, or uncertainty principle, one cannot simultaneously satisfy these two goals to arbitrary precision. The filter employed was selected for its optimal time and frequency domain characteristics within this basic limitation.

Once the signal has been narrow band filtered, it is corrected for the appropriate instrument response; the filtered signal transform is divided by the instrument transfer function. The resulting complex spectrum is then inverse Fourier transformed into the time domain, to produce what will hereafter be referred to as the filtered signal.

The narrow band filtered signal will appear as a quasi-sinusoidal carrier wave contained within a smooth envelope. The next step in the program (Figures 3a and 3b) is to construct the envelope function by means of the Hilbert transform. In particular, a quadrature signal is formed by multiplying the transform of the filtered signal by $-i \operatorname{sgn}(\omega)$ and then inverting this to the time domain by an inverse transformation. The envelope function is then constructed by taking the square root of the sum of the squares of the filtered signal and its quadrature. The maximum of the envelope function occurs at the time of arrival of energy at the center frequency of the filter and the amplitude of the maximum is proportional to the spectral amplitude of the filtered signal at the center frequency of the filter. The narrow band

band filtering procedure can be performed on a particular component seismogram at a number of different frequencies within some band of interest. Correlation of the resulting envelope functions indicates the arrival times of the various frequency components.

The instantaneous frequency and phase are computed from the filtered signal, and its quadrature signal as well, and are stored for subsequent use in polarization filtering with additional components of ground motion when available.

The variable frequency magnitudes used for event discrimination are based on the envelope maxima. As seen in Figure 3b (Block B), the traditional body and surface wave magnitude relationships are used in the MARS program. Given $\bar{m}_b(f)$ estimates at several frequencies within the teleseismic band (e.g., 0.3 to several Hertz), we can then construct $m_b(f_1)$ versus $m_b(f_2)$ plots, with $f_1 << f_2$, for different sensor-source region combinations and test for event discrimination. Examples of this procedure as applied to a large population of Eurasian events have been described in previous reports (Savino, et al., 1975; Bache, et al., 1976). While $\bar{m}_b(f)$ versus $\bar{M}_s(f)$ type discrimination could be easily implemented, as mentioned previously we are initially concentrating on analysis of short-period P wave recordings, or $\bar{m}_b(f)$ type discrimination.

2.4 PREVIOUS DISCRIMINATION RESULTS

Most of our previous experience with the $\bar{m}_b(f)$ discriminant has been with LASA full array beam recordings of short-period P waves from predominantly Eurasian events (Savino, et al., 1975; Bache, et al., 1976). We will briefly summarize the results of these previous studies and point out the importance for optimum discrimination of determining the various parameters

involved in the $\bar{m}_b(f)$ estimates (e.g., the particular frequencies) and the application of noise corrections.

Figure 4 shows the discrimination results obtained with the LASA data. The event data shown are only two of the frequency dependent magnitudes that characterize these events. However, for the range of teleseismic distances (Δ = 60 - 90°) and the particular type of receiver (LASA-full array beam), these two frequency dependent magnitudes at 0.45 and 2.25 Hz provide the best separation of the explosion-earthquake populations in the $\bar{m}_b(f)$ parameter space.

The events in Figure 4 are located in a variety of geologic and tectonic settings within Eurasia: two of the presumed explosions occurred in the arctic islands of Novaya Zemlya; the majority of the remaining explosions in the platform region of eastern Kazakhstan; the earthquakes originated along the Alpide and western Pacific seismic belts. Approximately 50 percent of the shallow earthquakes are located along the northern Japan, Kuril and Kamchatka arcs. We also point out that the Longshot explosion which was detonated in the Aleutian Islands is plotted on Figure 4 with coordinates $\bar{m}_b$(0.45 Hz) = 5.77 and $\bar{m}_b$(2.25 Hz) = 4.88. It has been suggested in the literature (Von Seggern and Blandford, 1977) that the locations of earthquakes in low-Q (high attenuation) zones, as opposed to presumed Eurasian explosions which are predominantly in high-Q (shield) zones, may account for the discrimination observed in Figure 4, as well as discrimination observed with other short period discriminants (Lacoss, 1969). While Q variations are important, and undoubtedly contribute to the scatter of the earthquake population in Figure 4, the results of several different studies suggest that differences in source characteristics are likely to account for short-period discrimination. For instance, Barazangi, et al. (1975) found large lateral variations in P-wave attenuation along several of the circum-Pacific arcs. In particular, they mapped

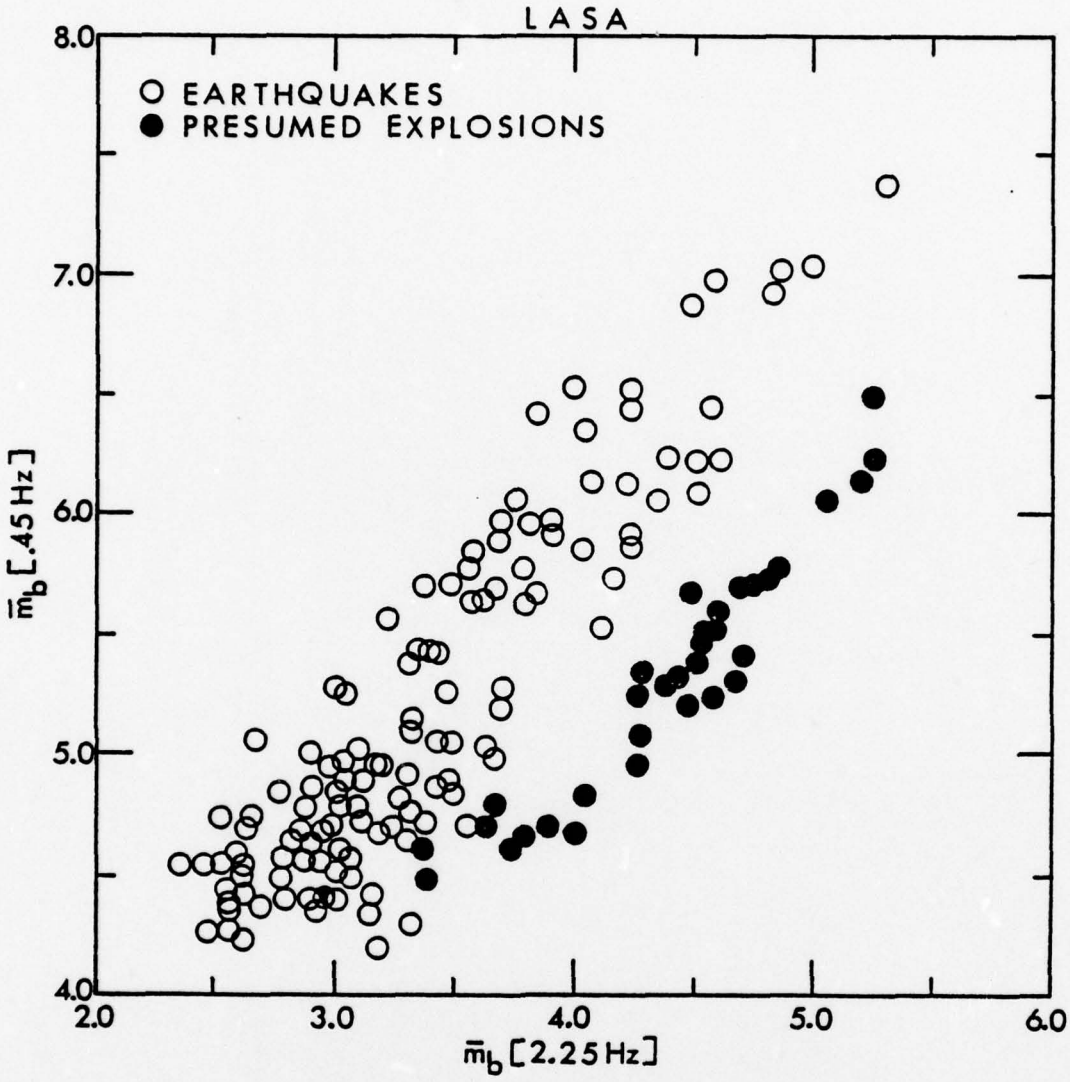

Figure 4. Variable frequency magnitude estimates at f_c = 0.45 Hz and f_c = 2.25 Hz based on short-period P waves from Eurasian events recorded at LASA (full array beam).

upper mantle regions of relatively low attenuation (Q ~ 500) beneath the shallow seismicity along the Japan, Kuril and Kamchatka arcs. The anomalously low-Q upper mantle zones were located well landward of the trench axes in three regions. As mentioned previously, a large number of the earthquakes in Figure 4 are located along these arcs over the high Q zones identified by Barazangi, et al. (1975). At a frequency of 2.25 Hz, the difference in $\overline{m}_b(2.25)$ for propagation through an upper mantle with Q of 500 versus a Q of ∞ is only 0.15 magnitude units, which is less than the separation of even those earthquakes that plot closest to the explosion population. It is also hard to imagine that the propagation paths for at least a few of the remaining earthquakes, that occurred in other seismic zones, were not in fact also along high-Q paths.

An ideal experiment that would provide conclusive evidence for the inherent effectiveness of short-period discriminants would be to compare explosions and earthquakes in the same source region, thereby minimizing the contribution from differences in propagation paths. Two such experiments were performed for events at NTS. Bakun and Johnson (1970) computed spectral ratios based on the short-period P_g phase recorded at the seismograph station at Jamestown, California (JAS), for several NTS explosions, afterevents and natural earthquakes outside NTS. The distance range considered was 250 to 500 km. These authors found that the NTS explosion spectra were significantly richer in high frequency (1.35 to 2.0 Hz) than spectra for all the natural earthquakes (located on both the near and far side of NTS with respect to JAS) and possible afterevents of the NTS Scotch explosion. On the other hand, they observed that the P-wave spectra of afterevents of the large NTS explosions (Benham, Boxcar and Jorum) resemble the explosion spectra.

At approximately the same time, Basham, et al. (1970) reported the results of spectral ratio and M_s-m_b discrimination

tests they performed on Benham and several of its afterevents, one of which was included in the experiment by Bakun and Johnson (1970). Basham, et al. (1970) used seismograms written at the Yellowknife array for their study. In this case the epicentral distance was approximately 25 degrees. In addition to complete separation on an M_s-m_b plot, they noted that the spectral ratio test produced excellent separation between the larger Benham afterevents and similar body-wave magnitude NTS explosions. Taken together, the results of these studies indicate that there are differences in the short-period P-wave spectra of closely spaced earthquakes and explosions which can be exploited by various short-period discriminants. The apparent ambiguity for the Benham afterevents may well be related to source mechanism. While seen as explosion-like at JAS (Δ = 3.5°, Az = 285°), for a take-off angle and azimuth appropriate for propagation to Yellowknife (Δ = 25°, Az = 2°) these events exhibit earthquake-like spectra. This potential problem could be overcome by the use of multi-station discrimination procedures.

As the data base for the present discrimination experiment increases, and when more accurate hypocentral information for the events becomes available, we will study our results in conjunction with known estimated variations in attenuation. The availability of data from the numerous stations in this experiment will hopefully allow us to differentiate between source and path effects on $\overline{m}_b(f)$ type discrimination.

Some of the scatter in the earthquake and explosion populations in Figure 4 is due to background seismic noise. This, of course, is relatively more important for events of small magnitude since the signal power will be low relative to the noise power, and causes some mixing, or convergence, of the two populations at the very low magnitudes. (The smallest explosions shown have conventional magnitudes, m_b, of about 4.)

The LASA time series as originally supplied to us did not include samples of the noise background preceding the signals. In order to study the effects of applying noise corrections to the $\bar{m}_b(f)$ data we obtained digital recordings of P waves for a subset of the events in Figure 4 recorded at the Oyer subarray in Norway. Each of the time series included at least 20 seconds of noise preceding the signal. Figure 5a shows the pair of $\bar{m}_b(f)$ estimates that provided the best discrimination for this source region-receiver combination. Note that the magnitude estimates in Figure 5a are not corrected for noise and, once again, we observe convergence of the event populations at lower magnitudes. The arrows on the smallest explosion data points indicate the direction in which a noise correction would move these points in this magnitude plane. Figure 5b shows the effect of the noise correction applied to <u>all</u> the events, including earthquakes as well as explosions. (In this figure, only the log of the amplitude is plotted, the $\bar{m}_b$ plot would be identical except for a scale change.) It is evident that the explosion population is now well separated from the earthquake population. The arrows on the two small explosions, both with conventional m_b magnitudes somewhat less than 4.0, indicate that it is likely that the unbiased estimate of the noise contamination is lower than that actually present and that the true event points are still lower in the direction indicated. Fortunately, all the data for the present discrimination experiment include adequate samples of background noise.

The trends of the earthquake and explosion populations in Figures 4 and 5a are approximately the same, even though the $\bar{m}_b(f)$ planes are computed for significantly different frequency combinations. Comparison of the noise corrected $\bar{m}_b(f)$ estimates plotted in Figure 5b with the $\bar{m}_b(f)$ planes in Figures 4 and 5a indicates that the major effect of the noise corrections applied to the Norway data has been to rotate both the

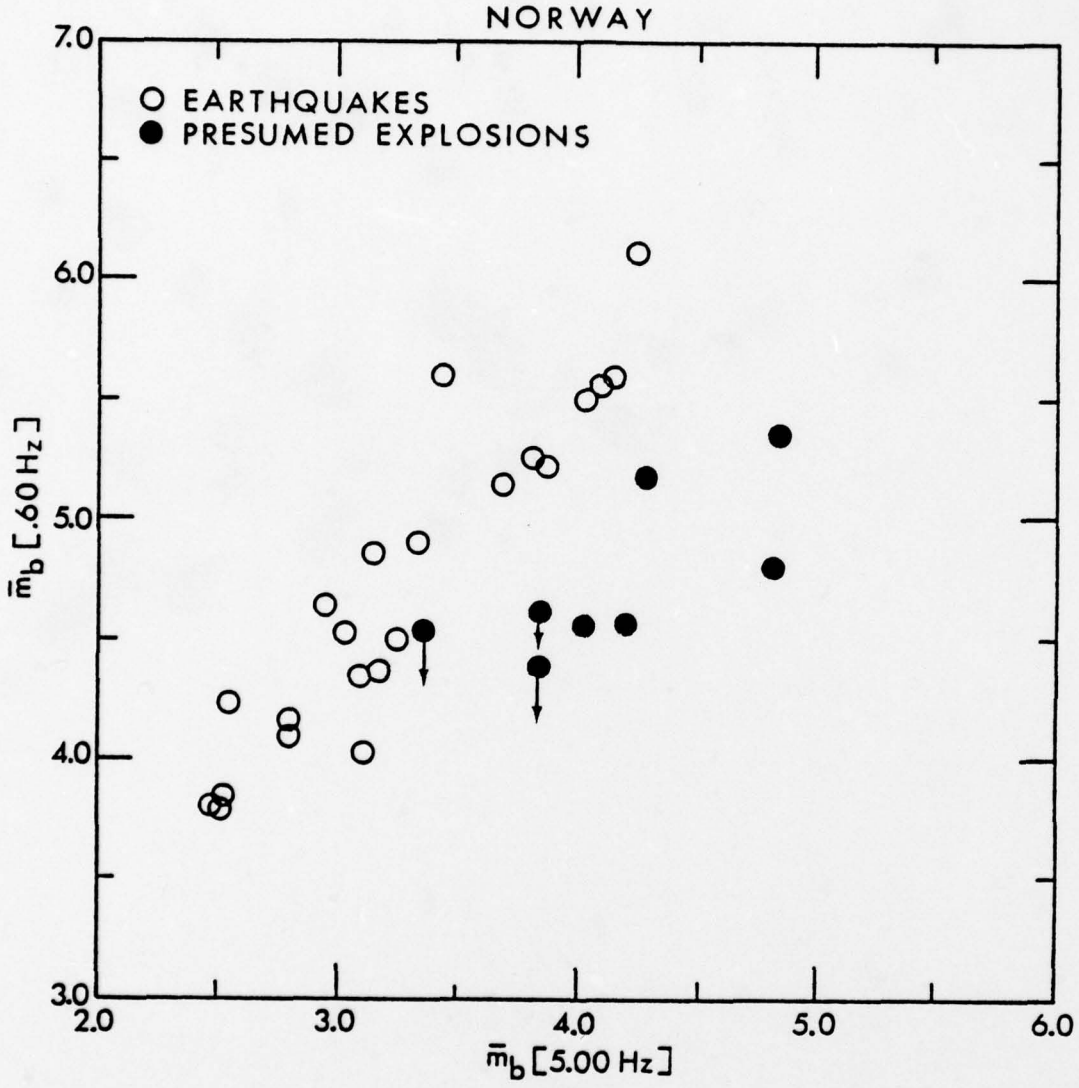

Figure 5a. Variable frequency magnitude estimates at f_c = 0.6 Hz and f_c = 5.0 Hz based on short-period P waves from Eurasian events recorded at the Oyer subarray in Norway. Arrows attached to presumed explosions indicate noise contamination of the $\bar{m}_b$ (0.6 Hz) estimates.

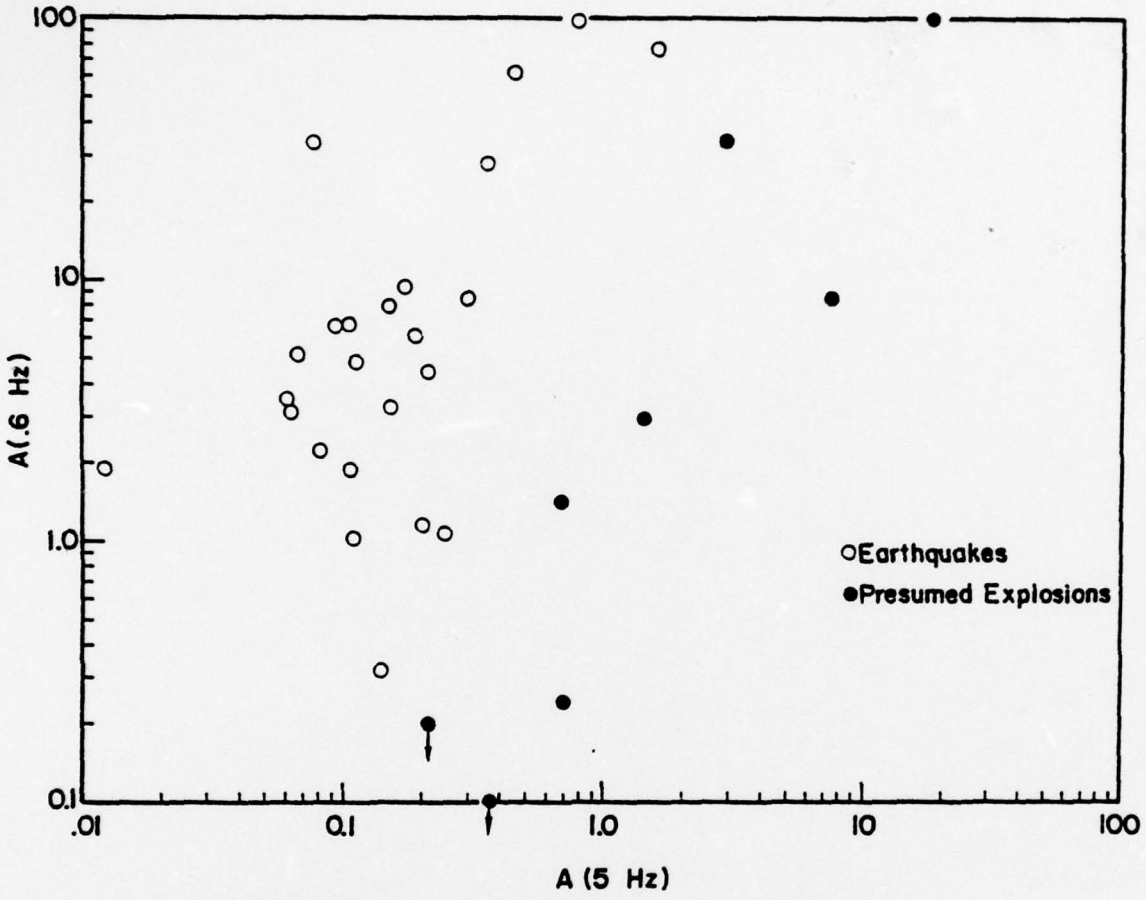

Figure 5b. Amplitudes of the narrow-band filter outputs for the same event population plotted in Figure 5a with noise corrections applied.

earthquake and explosion populations in a counterclockwise direction. The result is to increase the slope of a line separating the two event populations in Figure 5b.

2.5 PRESENT DISCRIMINATION EXPERIMENT

The approach that we have adopted at this early stage in the experiment is to build on our previous discrimination results before extending the analysis to include data from stations where we have no experience with the $\bar{m}_b(f)$ discriminant. As described in the previous subsection of this report, most of our experience has been with Eurasian events recorded at LASA and Norway. In addition, a single presumed explosion, occurring at Semipalatinsk and recorded at the SRO station in Albuquerque, New Mexico (ANMO), has been tested for discrimination with the $\bar{m}_b(f)$ technique by Lambert and Bache (1977).

A further criterion for the selection of stations for initial detailed analysis is the availability and quality of event data, particularly for the first 10 to 15 events that were received earlier in the reporting period. Table 2 summarizes the status of the short-period P wave data received to date on an event-station basis. We distinguish only three possibilities: + implying usable data; - nonusable data and; blanks for no data. Not included in this table is the fact that many of the event recordings at a particular station have very low signal-to-noise ratios. Based on Table 2 and our previous experience, the initial attempts at discrimination have concentrated on ANMO and LAO.

In Figure 6 $\bar{m}_b(f)$ estimates at 2.25 and 0.45 Hz are plotted for 12 events recorded at ANMO (closed circles) and four events recorded at LAO (open circles). The $\bar{m}_b(f)$ estimates have been corrected for nominal instrument reponses. The dashed and solid curves represent the bounds of the Eurasian earthquake and explosion populations, respectively,

TABLE 2

SUMMARY OF SHORT PERIOD DATA AVAILABILITY

EVENT	ANMO	BOCO	CHTO	CTAO	GUMO	KAAO	MAIO	MAJO	NWAO	SNZO	TATO	ZOBO	LAO	NAO	ALK	ATTU	ILPA	KSRS	RK-ON	HN-ME
1	+		+			+	+	+					-		+			+		
14	+		+			+	+	+			-		-	-	-			-		
16	+					+						+	-	+	+	+		+		
17						+								+	+		+	+		
18	+		+														+	+		
19	+		+			+		+			+		+	-			+	+	+	+
20	+		+	+		+		+	+		+	+					+	+	+	+
21	+			+		+									+		+	+		
22	+				+	+						+					+	+		
33									+				+	+	+	+	+	+		
38					+								+	+	+		+	+		
41						+	+										+	+		
47	+		+	+								+	+	+	+	+	+	+		
48						+	+				+		+	+	-		+	+		
49	+		+	+	+	+	+		+				+	+			+	+		
53	+			+		+	+	+	+				+	+	+		+	+		
55					+								+	+	+	+	+	+		
57						+					+		+	+	+	+	+	+		
59	+					+	+						+	+	+		+	+		

\+ DATA
\- BAD DATA
BLANKS - DATA UNAVAILABLE

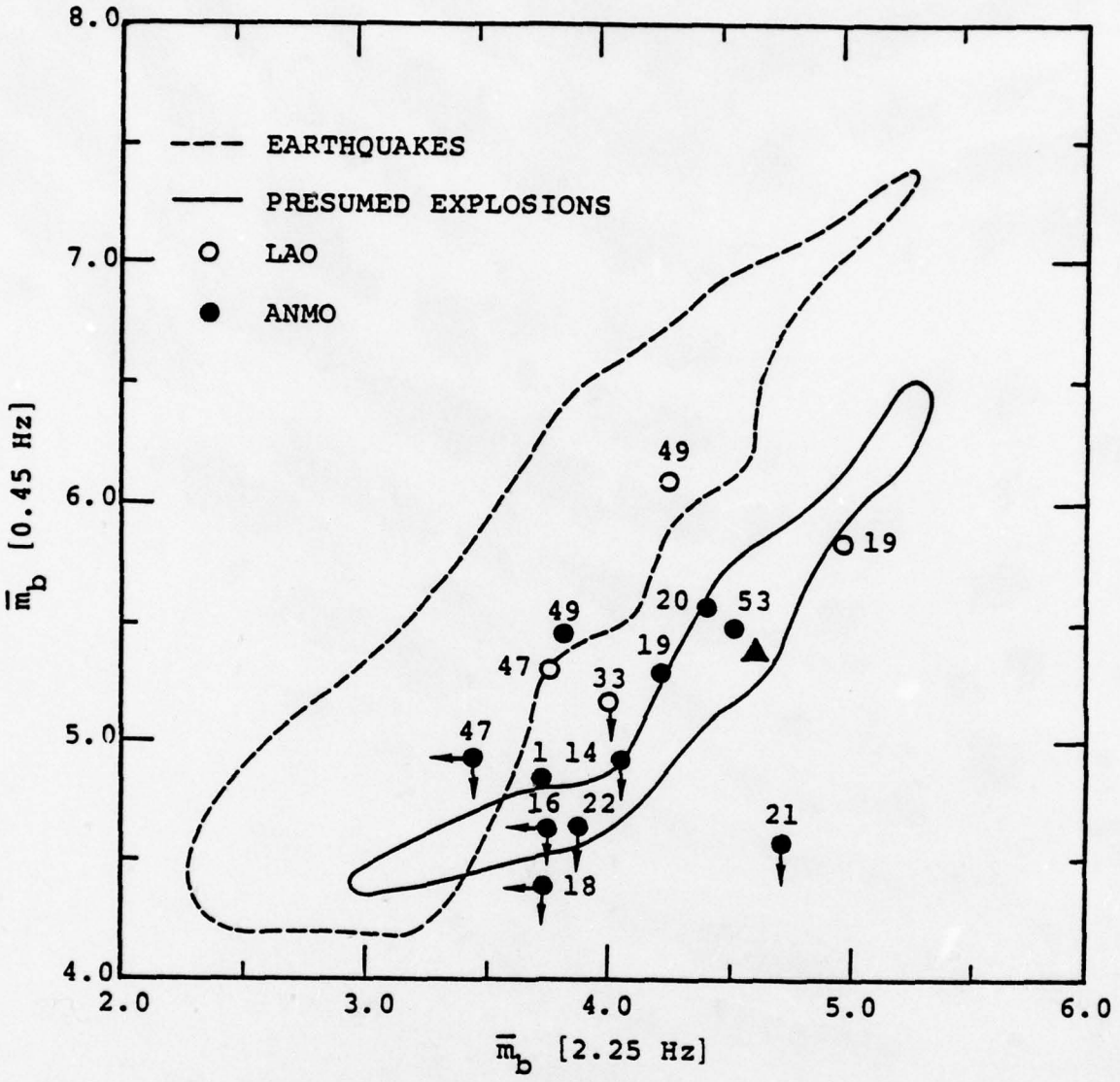

Figure 6. Variable frequency magnitude estimates at f_c = 0.45 Hz and 2.25 Hz based on short-period P waves recorded at ANMO and LAO for several of the Eurasian events in the discrimination experiment. These estimates are compared to populations defined in Figure 4.

plotted in Figure 4. Recall that the $\bar{m}_b(f)$ plotted in Figure 4 were based on the full array beam recordings from LASA, whereas the open circles in Figure 6 are magnitude estimates from the LAO subarray (AO) recordings. Finally, the solid triangle denotes a presumed explosion located at Semipalatinsk and recorded at ANMO. This event was the subject of a special study by Lambert and Bache (1977) wherein a multiple explosion scenario, simulated with the ANMO time series, was successfully decomposed.

Considering the results for ANMO in Figure 6, we tentatively identify events 47 and 49 as earthquakes and events 14, 19, 20, 21, 22 and 53 as explosion-like. Both the high and low frequency m_b estimates for events 16 and 18 are contaminated by background noise and will require corrections before more positive identification can be made. Note, however, that at this point these two events are likely to remain explosion-like since it was not possible to make noise corrections for the small earthquakes previously studied at LASA (the dashed population) with the net effect that the high-frequency estimates, in particular, were biased high. Had we been able to make noise corrections, similar to those for Norway in Figure 5b, we would expect the low magnitude portion of the dashed earthquake population to preferentially move to the left in Figure 6. Based on the same argument we identify event 1 as explosion like.

The results for Station LAO, while more limited (see Table 2), agree with those for ANMO for common events (19, 47, 49) and indicate that event 33 is explosion-like.

The epicentral distance range for the events in Figure 6 to ANMO and LAO is about 60 to 98 degrees. Thus, it is of interest to examine the $\bar{m}_b(f)$ behavior of these events at smaller epicentral distances. Figure 7 shows magnitude estimates for 11 events recorded at the SRO station KAAO in Kabul,

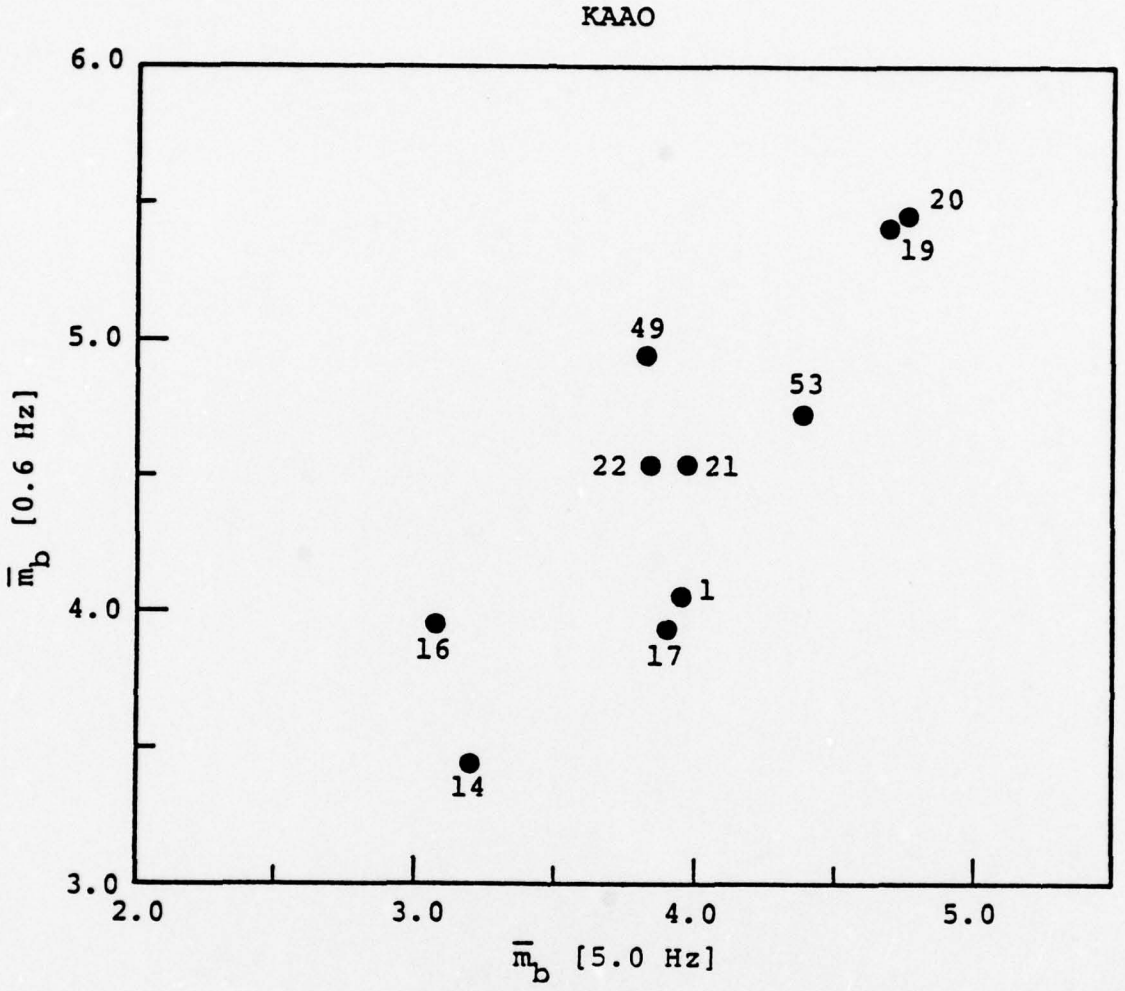

Figure 7. Variable frequency magnitude estimates at f_c = 0.6 Hz and f_c = 5.0 Hz for a subset of the Eurasian events in the discrimination experiment recorded at KAAO.

Afghanistan. The distance range is 16° to 65°. We selected the $\bar{m}_b(f)$ estimates that were least contaminated by noise and span the widest frequency range sampled. Given these criteria, the two narrow-band filter center frequencies selected are 0.6 Hz and 5 Hz.

Based on the results of ANMO and LAO (Figure 6), several of the events plotted in Figure 7 (1, 14, 16, 17, 19, 20, 21, 22 and 53) were tentatively identified as explosion-like; while event 49 was called an earthquake. Note that no short-period P-wave data are available for event 47 at KAAO (Table 2). The tentative event identification based on ANMO and LAO data is supported by the results from KAAO for all but possibly one event, number 16, which is on the border line in Figure 7. Obviously, we will have to analyze more events at KAAO and establish the boundaries of the earthquake and explosion populations before we can make more definitive statements.

The next station that we analyzed data from is in Bluff, Alaska (BFAK). Six events, with epicentral distances between 33° and 61° were available for study and their $\bar{m}_b(f)$ estimates at filter center frequencies of 0.6 Hz and 4.0 Hz are shown in Figure 8. The results, while restricted in number, are quite striking. Event 47, which was called an earthquake at ANMO and LAO, is well separated from the remaining five events which appeared explosion-like at ANMO and LAO (Figure 6). In addition, a noise correction for the m_b (4.0 Hz) estimate for event 47 would further increase the separation. The final point to be noted is the near linearity of the explosion-like events in Figure 8. We will be particularly interested in seeing how the populations fill in at this station as more events are analyzed.

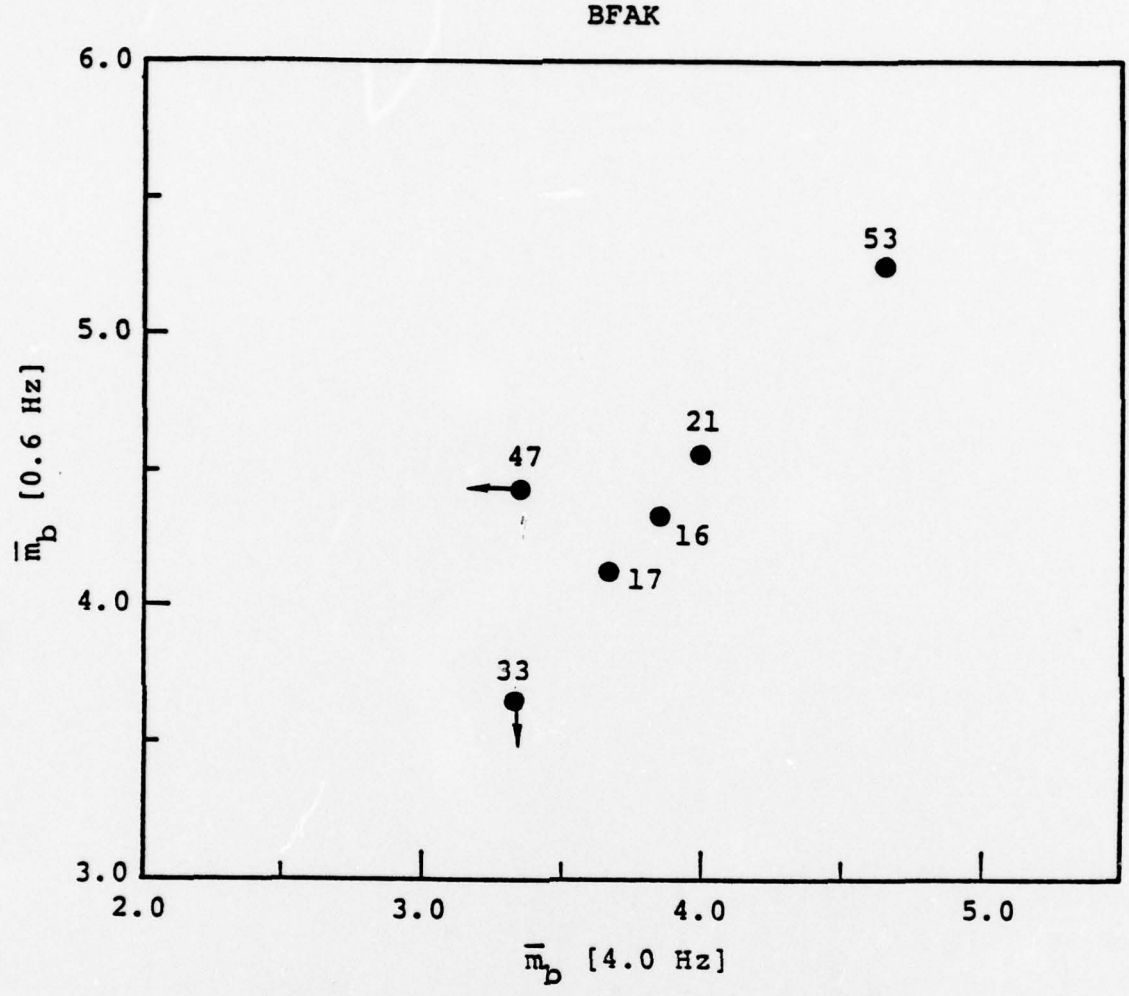

Figure 8. Variable frequency magnitude estimates at f_c = 0.6 Hz and f_c = 4.0 Hz for a subset of the Eurasian events recorded at BFAK.

2.6 SUMMARY

During this reporting period, we received seismic waveforms for nineteen Eurasian events and initiated an event identification study based on variable frequency magnitude estimates. Table 3 summarizes the preliminary identifications made for thirteen of the larger events recorded at four different stations. At this point in the experiment we are unable to assign probabilities to the event identifications in Table 3. To do so will require the addition of more events so that the extent of the earthquake and explosion populations can be better defined at each of the stations.

Our plans for the future are the following:

1. Define the event populations at all the stations contributing short-period P-wave seismograms.

2. Apply noise corrections to the $\overline{m}_b(f)$ estimates.

3. Test automated single- and multi-station discrimination techniques once the data sets are adequate.

TABLE 3

PRELIMINARY EVENT IDENTIFICATION

Earthquakes (Event Number)				Explosion-Like Events (Event Number)			
ANMO	LAO	KAAO	EURO	ANMO	LAO	KAAO	EURO
47	47		47	1		1	
49	49	49		14		14	
				16			16
						17	17
				18			
				19	19	19	
				20		20	
				21		21	21
				22		22	
					33		33
				53		53	53

III. ANALYTIC CONTINUATION OF THE ELASTIC FIELD FROM A COMPLEX SOURCE IN A HALFSPACE

An important problem in nuclear explosion and earthquake seismology is the development of a capability for linking detailed numerical source calculations with efficient analytical techniques for propagating elastic waves in layered media. If the source is in a homogeneous wholespace, techniques employing an expansion of the outgoing waves in spherical harmonics work very well and have been employed to study earthquakes (Bache, et al., 1976) and complex nuclear explosions (Cherry, et al., 1975, 1976; Bache and Masso, 1978). However, these techniques are not rigorously valid when a material boundary is present in the source region. Bache, et al. (1977) introduced some ad hoc approximations and applied the whole space technique to study near-surface explosions in a halfspace. Even though this worked fairly well for the case studied, it has some serious drawbacks and better methods are needed.

In this section, we present some mathematical results outlining a method for analytically continuing the output of a finite difference simulation of a source in a layered halfspace. The source calculations may include arbitrary nonlinearity in a portion of the grid. It is also necessary that the waves be computed out into the region where the material response is linearly elastic.

The particular case discussed here is the computation of the body waves at an arbitrary range in a layered earth model from an axisymmetric source in a halfspace. Following a similar procedure, the surface waves can also be computed, though this is not worked out here. The method used may be generalized to other geometries.

The mathematical basis of our approach is the elastodynamic integral representation given by Burridge and Knopoff (1964). This is a rigorous expression for the displacement in an elastic medium in terms of a surface integral over a (non-physical) boundary Σ which entirely encloses the source volume (including all inelastic regions). Two elements are required to form this integral solution. First, we must have the time histories of the displacement vector $\underline{U}\ (\underline{x}_o,t)$ and the stress vector $\underline{\tau}\ (\underline{x}_o,t)$ on Σ. These are obtained from the finite difference source calculation. Second, the Green's tensor $\underline{\underline{g}}\ (\underline{x}, \underline{x}_o; t-t_o)$ and its spatial derivatives (for the appropriate elastic medium) must be evaluated for the prospective receiver point $\underline{x}$, for all $\underline{x}_o$ on Σ. The elastic medium used to compute $\underline{U}\ (\underline{x}_o,t)$ and $\underline{\tau}\ (\underline{x}_o,t)$ must be the same as that used to compute $\underline{\underline{g}}\ (\underline{x}, \underline{x}_o; t-t_o)$.

The general form of the integral representation (assuming isotropy) is

$$\underline{U}\ (\underline{x},t) = \int dt \int_{\Sigma} ds\ [\underline{\underline{g}}(\underline{x}, \underline{x}_o; t-t_o) \cdot \underline{\tau}\ (\underline{x}_o, t_o) - \underline{\underline{g}}\ \underline{\nabla}\ (\underline{x},\underline{x}_o; t-t_o) : \underline{\underline{M}}\ (\underline{x}_o,t_o)] \qquad (3.1)$$

where

$$\underline{\underline{M}}(\underline{x}_o,t_o) \equiv \lambda \underline{\underline{I}}\ \hat{n} \cdot \underline{U}(\underline{x}_o,t_o) + \mu[\hat{n}\ \underline{U}(\underline{x}_o,t_o) + \underline{U}(\underline{x}_o,t_o)\hat{n}].$$

$\underline{x}$ and t are receiver position and time,
λ and μ are elastic constants,
$\hat{n}$ is the normal to Σ, directed into the source volume,
$\underline{U}$ is the displacement vector,
$\underline{\tau}$ is the stress vector on Σ,
$\underline{\underline{g}}$ is the Green's tensor solution,
$\underline{\underline{I}}$ is the identity tensor.

This formulation is entirely general. However, we will now specialize to the case of an axisymmetric source and assume that the geologic structure is represented by some plane-layered earth model.

We assume that the elastic medium occupies the halfspace $z > o$. We introduce the cylindrical coordinates r, θ, z, and assume that the elastic properties of the medium and the r and z components of displacement are independent of θ and that the θ component of displacement is zero. Finally, we specify the surface Σ to be a cylinder of radius a extending from $z = 0$ to $z = b$. The geometry is shown in Figure 9. In this special case, Equation (3.1) can be written in terms of cylindrical components as

$$
\begin{aligned}
U_j(r,z,t) = &- a\,[G_r^{j*}{}_{t,z}\,\sigma_{rr} + G_z^{j*}{}_{t,z}\,\sigma_{rz}] \\
&- [G_r^{j*}{}_{t,r}\,\sigma_{rz} + G_z^{j*}{}_{t,r}\,\sigma_{zz}] \\
&+ a\,(\lambda+2\mu)\left(\frac{\partial}{\partial r_0} G_r^j\right) + \lambda \frac{\partial}{\partial z_0} G_z^j + \frac{1}{a} G_r^j \;*_{t,z}\, U_r \\
&+ a\mu\left(\frac{\partial}{\partial r_0} G_z^j + \frac{\partial}{\partial z_0} G_r^j\right) *_{t,z}\, U_z \\
&+ \left[\lambda \frac{\partial}{\partial r_0} G_z^j + (\lambda+2\mu) \frac{\partial}{\partial z_0} G_z^j + \frac{\lambda}{r_0}\right] *_{t,r}\, U_z \\
&+ \mu\left(\frac{\partial}{\partial r_0} G_z^j + \frac{\partial}{\partial z_0} G_r^j\right) *_{t,r}\, U_r . \qquad (3.2)
\end{aligned}
$$

where G_i^j is the azimuthally averaged Green's tensor component

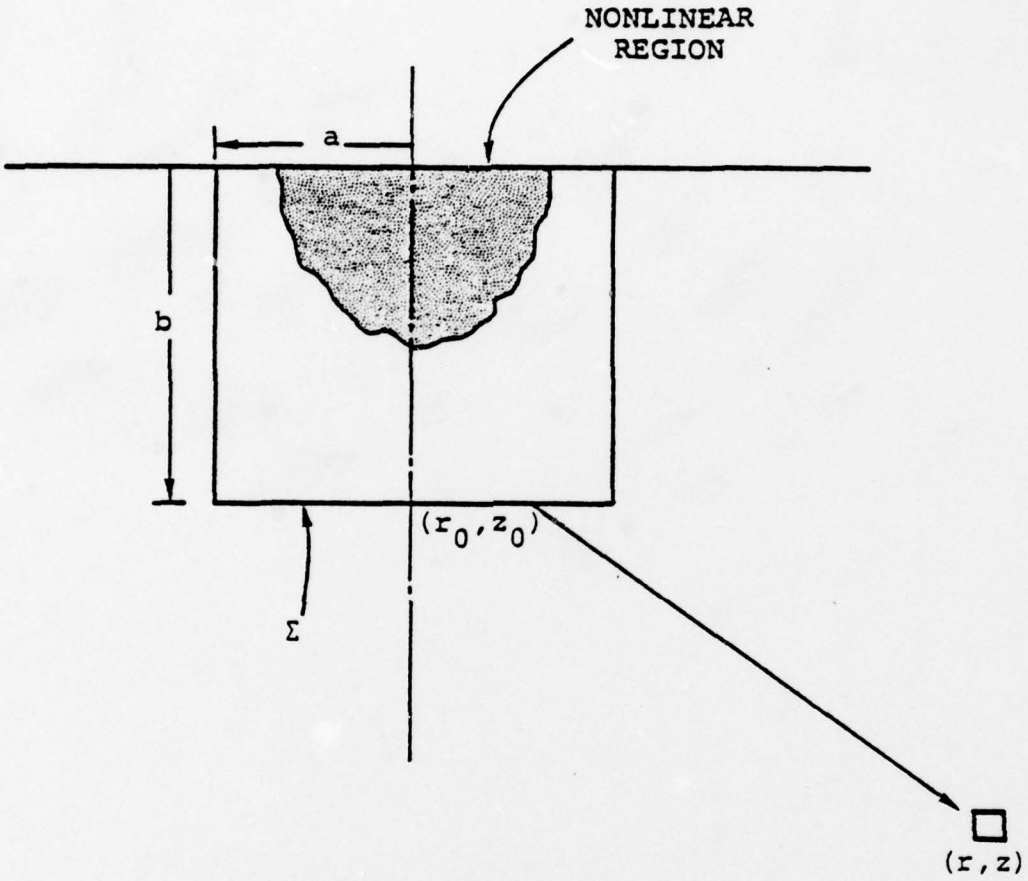

Figure 9. The source-receiver geometry is shown for the axially symmetric case. The monitoring surface Σ is a cylinder of radius a and height b.

$$G_i^j(r_0,r,z_0,z,t-t_0) = \int_0^{2\pi} g_i^j(r_0,r,z_0,z,\phi-\phi_0,t-t_0)\,d\phi \qquad (3.3)$$

and the operators $*_{t,z}$ and $*_{t,r}$ are defined by

$$G_i^j *_{t,z} f = \int_{-\infty}^{\infty} dt_0 \int_0^b dz_0 \left\{G_i^j(a,r,z_0,z,t-t_0)\, f(a,z_0,t_0)\right\},$$

$$G_i^j *_{t,r} f = \int_{-\infty}^{\infty} dt_0 \int_0^a dr_0 \left\{r_0 G_i^j(r_0,r,b,z,t-t_0)\, f(r_0,b,t_0)\right\} \qquad (3.4)$$

Equation (3.2), while lengthy, is a sum of similar terms. Each term has the form

$$G_i^j(r,r_o,z_o,z,t-t_o) *_{t,\Sigma} v_i(r_o,z_o,t_o)$$

where v_i is a displacement or traction component monitored on Σ. Thus, the procedure is to solve for the Green's function for a point on Σ, carry out the integrals (Equation 3.4) with the stress and displacement time histories at that point and then sum the integrals according to Equation (3.2).

The form of the Green's functions depends on the range and type of seismic wave to be propagated. In the following, we present the Green's functions that are compatible with far-field surface wave methods and with near-field and far-field body wave methods.

We begin with the integral solutions for the displacement due to a point force embedded in a homogeneous, linearly elastic space:

$$g_i^j(r,z,\omega) = \frac{1}{4\pi\rho\omega^2} \int_0^{\infty} dk \left\{k\,[A_{ij}^{\alpha}(k,\omega) + A_{ij}^{\beta}(k,\omega)]\right\} \qquad (3.5)$$

where

$$A_{ij}^{\alpha} = \frac{e^{-\nu_\alpha z}}{\nu_\alpha} \begin{bmatrix} k^2 J_0(kr) & -k\nu_\alpha J_1(kr) \\ -k\nu_\alpha J_1(kr) & -\nu_\alpha^2 J_0(kr) \end{bmatrix} ,$$

$$A_{ij}^{\beta} = \frac{e^{-\nu_\beta z}}{\nu_\beta} \begin{bmatrix} -\nu_\beta^2 J_0(kr) & k\nu_\beta J_1(kr) \\ k\nu_\beta J_1(kr) & k^2 J_0(kr) \end{bmatrix} , \qquad (3.6)$$

and

$$\nu_\gamma = \left(k^2 - \frac{\omega}{\gamma}^2 \right)^{1/2} .$$

The azimuthally averaged Green's tensor, Equation (3.3), is required. As is shown in Figure 10, we introduce the dimensions a, the cylinder radius and r_T, the horizontal distance from the center of the cylinder to the observer, while r is the horizontal distance from a point on the cylinder to the observer. The only functions in Equation (3.5) which depend on r are the Bessel functions. Now, from Watson (1944),

$$J_\nu(kr) e^{\nu i\phi} = \sum_{m=-\infty}^{\infty} J_{\nu+m}(kr_T) \; J_m(ka) e^{im\phi} ,$$

and, taking the azimuthal average, we have

$$\int_0^{2\pi} J_\nu(kr) \, d\phi = \sum_{m=-\infty}^{\infty} J_{\nu+m}(kr_T) \; J_m(ka) \int_0^{2\pi} e^{i(m-\nu)\phi} d\phi$$

$$= 2\pi \; J_{2\nu}(kr_T) \; J_\nu(ka) .$$

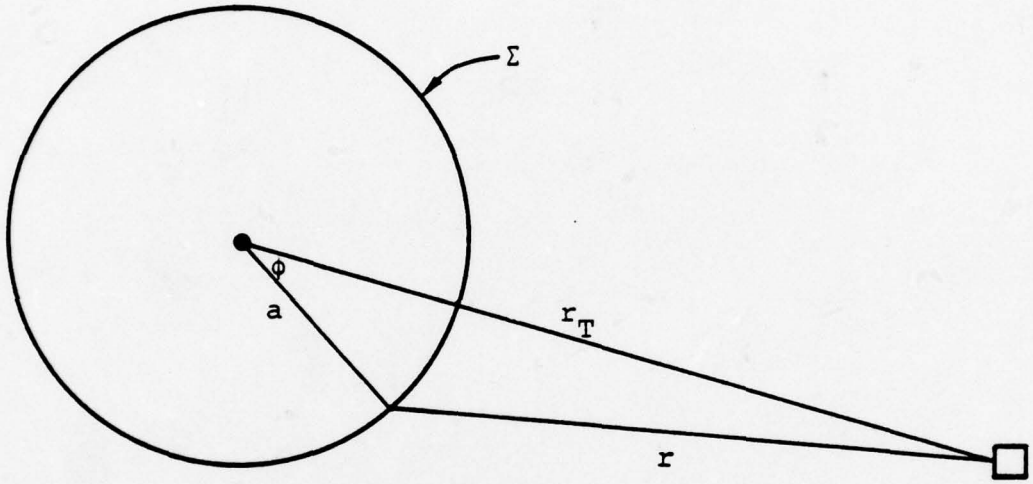

Figure 10. The monitoring cylinder Σ is shown from directly above the free surface. The geometry for computing the azimuthal average of the Green's function is also shown.

The azimuthally integrated Green's tensor is then

$$G_i^j(\omega) = \frac{1}{\rho\omega^2} \int_0^\infty dk \left\{ k \left[B_{ij}^\alpha + B_{ij}^\beta \right] \right\}, \tag{3.7}$$

where

$$B_{ij}^\alpha = e^{\frac{-\nu_\alpha z}{\nu_\alpha}} \begin{bmatrix} k^2 J_0(kr_T)\ J_0(ka) & -k\nu_\alpha J_2(kr_T) J_1(ka) \\ -k\nu_\alpha J_2(kr_T) J_1(ka) & -\nu_\alpha^2 J_0(kr_T) J_0(ka) \end{bmatrix},$$

and

$$B_{ij}^\beta = e^{\frac{-\nu_\beta z}{\nu_\beta}} \begin{bmatrix} -\nu_\beta^2 J_0(kr_T) J_0(ka) & k\nu_\beta J_2(kr_T) J_1(ka) \\ k\nu_\beta J_2(kr_T) J_1(ka) & k^2 J_0(kr_T) J_0(ka) \end{bmatrix},$$

Equation (3.7) may be combined with layer matrices to develop the theory for surface waves.

To compute body waves, we have chosen to use generalized ray methods and the Cagniard-de Hoop inversion technique. To cast the solutions in the form compatible with these methods, we return to Equation (3.5). We make the substitutions $\omega = -is$ and $k = -isp$. This separates the s and p dependence and takes us from Fourier to Laplace transform space. The solutions for the point forces are now

$$g_i^j(r,z,s) = -\frac{s}{2\rho\pi^2} \operatorname{Im} \int_0^{i\infty} dp\ p \left[e^{-s\eta_\alpha z}\ C_{ij}^\alpha(p,s) + e^{-s\eta_\beta z}\ C_{ij}^\beta(p,s) \right] \tag{3.8}$$

where

$$C_{ij}^{\alpha}(p,s) = \frac{1}{\eta_\alpha}\begin{bmatrix} p^2K_0(spr) & -\varepsilon p\eta_\alpha K_1(spr) \\ -\varepsilon\eta_\alpha p K_1(spr) & \eta_\alpha^2 K_0(spr) \end{bmatrix},$$

$$C_{ij}^{\beta}(p,s) = \frac{1}{\eta_\beta}\begin{bmatrix} \eta_\beta^2 K_0(spr) & \varepsilon p\eta_\beta K_1(spr) \\ \varepsilon p\eta_\beta K_1(spr) & p^2 K_0(spr) \end{bmatrix},$$

and

$$\eta_\gamma = \left(\frac{1}{\gamma^2} - p^2\right)^{1/2},$$

$$\varepsilon = \begin{cases} +1 & \text{for upgoing wave,} \\ -1 & \text{for downgoing wave.} \end{cases}$$

It can be shown (e.g., Cisternas, Betancourt and Leiva, 1973) that the response of a layered medium with L layers with thickness h_ℓ and elastic properties α_ℓ, β_ℓ, ρ_ℓ is given by

$$g_i(r,z,s) = -\frac{s}{2\rho\pi^2}\sum_{n=1}^{\infty} \mathrm{Im}\int_0^{i\infty} dp\; p\left[C_{ij}^{\alpha}(p,s)\; T_n^{\alpha}(p)\exp(-st_n^{\alpha})\right.$$

$$\left. + C_{ij}^{\beta}(p,s)\; T_n^{\beta}(p)\exp(-st_n^{\beta})\right] \qquad (3.9)$$

Each element of the sum in Equation (3.9) represents a "generalized ray" prescribed by the layers a ray traverses and its mode (p or s) in each layer. A ray has a vertical phase shift

$$t_n^\gamma = (\eta_\gamma h)_s + \sum_{\ell=1}^{N_n} h_\ell \eta_{\gamma_\ell}$$

(the subscript s denotes properties in the source layer) and amplitude factor T_n^γ, the product of reflection and transmission coefficients due to the impedance contrasts between the layers. Although the sum in Equation (3.9) is infinite for problems related to the work proposed here, the solution is dominated by a few rays.

Before we can use Equations (3.8) and (3.2), we must perform an inverse Laplace transform and compute the azimuthal average. First transforming, we obtain the time-domain Green's tensor for the n^{th} generalized ray. This is

$$g_{i_n}^j(r,z,t) = -\frac{1}{2\rho\pi^2}\frac{\partial}{\partial t}\left\{ \mathrm{Im} \int_{t_{on}^\alpha}^{t} d\tau\, p\, C_{ij}^\alpha(p,t)\; T_n^\alpha(p)\, \frac{dp}{d\tau}\, [(t-\tau)(t-\tau+2pr)]^{1/2} \right.$$

$$\left. + \mathrm{Im} \int_{t_{on}^\beta}^{t} d\tau\, p\, C_{ij}^\beta(p,t)\; T_n^\beta(p)\, \frac{dp}{d\tau}\, [(t-\tau)(t-\tau+2pr)]^{1/2} \right\} \tag{3.10}$$

where the path of integration is defined by

$$\mathrm{Im}\ \tau = \mathrm{Im}\left[pr + \sum_{\ell=1}^{N} h_\ell \eta_\ell + h_s \eta_s \right] = 0, \tag{3.11}$$

and t_{on}^γ is the ray arrival time. The matrices C in the time domain are given by

$$C^{\alpha}_{ij}(p,t) = \frac{1}{\eta_\alpha}\begin{bmatrix} p^2 & -\varepsilon p \eta_\alpha \zeta(p,t) \\ -\varepsilon \eta p \zeta(p) & \eta_\alpha^2 \end{bmatrix},$$

$$C^{\beta}_{ij}(p,t) = \frac{1}{\eta_\beta}\begin{bmatrix} \eta_\beta^2 & \varepsilon p \eta_\beta \zeta(p,t) \\ \varepsilon p \eta_\beta \zeta(p) & p^2 \end{bmatrix},$$

where

$$\zeta(p,t) = \frac{t-\tau+pr}{pr} .$$

In the near-field (where the periods of interest and the travel time are of the same order), the integrals in Equation (3.10) must be done numerically. The results for different azimuths (ϕ) must then be summed to compute the azimuthal averages.

In the far-field, the computation of (s) can be simplified by invoking the approximation $t-\tau << pr$. In this case $\zeta(p,t) \approx 1$, and Equation (3.10) can be written as

$$g^{j}_{i_n}(t) \approx -\frac{1}{2\rho\pi^2}\sqrt{\frac{\pi}{2r}}\left\{ \mathrm{Im}\left[\sqrt{p}\; C^{\alpha}_{ij}(p,t)\; T^{\alpha}_{n}(p)\; \frac{dp}{d\tau}\right] + \mathrm{Im}\left[\sqrt{p}\; C^{\beta}_{ij}(p,t)\; T^{\beta}_{n}(p)\; \frac{dp}{d\tau}\right]\right\} * \frac{1}{\sqrt{t}} \qquad (3.12)$$

where the functions of p are evaluated along the Carniard contour (Equation 3.11). The convolution may now be done after all the rays are summed, which greatly reduces the computing time.

The far-field regime allows another time saving approximation in addition to the one just described. At distances large compared to the cylinder dimensions, the amplitude and

frequency content of Green's functions due to rays coming from various parts of Σ are nearly equal. The greatest variation is in their relative arrival times. Thus, it is necessary to compute only one or perhaps a few Green's functions rather than one for each point on Σ. This feature makes the azimuthal average quite easy to compute.

The theory presented above is now being programmed and tested. With the program we will be able to continue the output of axisymmetric finite difference calculations to any range of interest in plane-layered earth models. The analytic continuation is done entirely in the time domain, obviating the need to compute Fourier transforms which can sometimes be rather difficult. A similar theory can be developed for computing the surface waves excited by the finite difference output. Having the results presented here, the development of this theory is rather straightforward and will be done during this quarter.

IV. THEORETICAL COMPUTATION OF Lg

In this section we summarize the results of a brief study of the excitation of the regional phase Lg. The study was conducted at VSC request and the results were presented orally at an ARPA Program review covering seismic detection and discrimination at regional distances and held in Dallas on 11 and 12 January 1978.

Knopoff, Schwab, Panza and several others at UCLA and elsewhere have demonstrated that waves having the observed characteristics of Lg are present in plane-layered models (e.g., Panza, Schwab and Knopoff, 1972; Knopoff, Schwab and Kausel, 1973; Panza and Calcagnile, 1975). Higher modes for both Rayleigh and Love waves in continental structures have stationary phases at about 3.5 km/sec.

To illustrate the theoretical behavior of Lg, synthetic seismograms were computed for a double-couple source in an earth model meant to represent an average continental structure. The earth model was provided by VSC (Michael J. Shore, personal communication). The shear wave velocity-depth profile for this model is plotted in Figure 11. Also plotted in the figure is the low velocity zone (LVZ) model for which the Lg phase was studied extensively by Knopoff, Schwab and Kausel (1973), Knopoff, et al., (1974) and Panza and Calcagnile (1975). The most important difference between the two is that the VSC model has no sedimentary layers at the top. Instead, the top 12 kilometers are uniform with β = 3.58 km/sec. Otherwise, the two models are sufficiently similar for the trends reported by Knopoff and coauthors to remain valid. Also provided by VSC was a Q model which takes a simple form. The Q is 1500 to a depth of 300 km and increases at greater depth. For our purpose this is essentially a constant Q model.

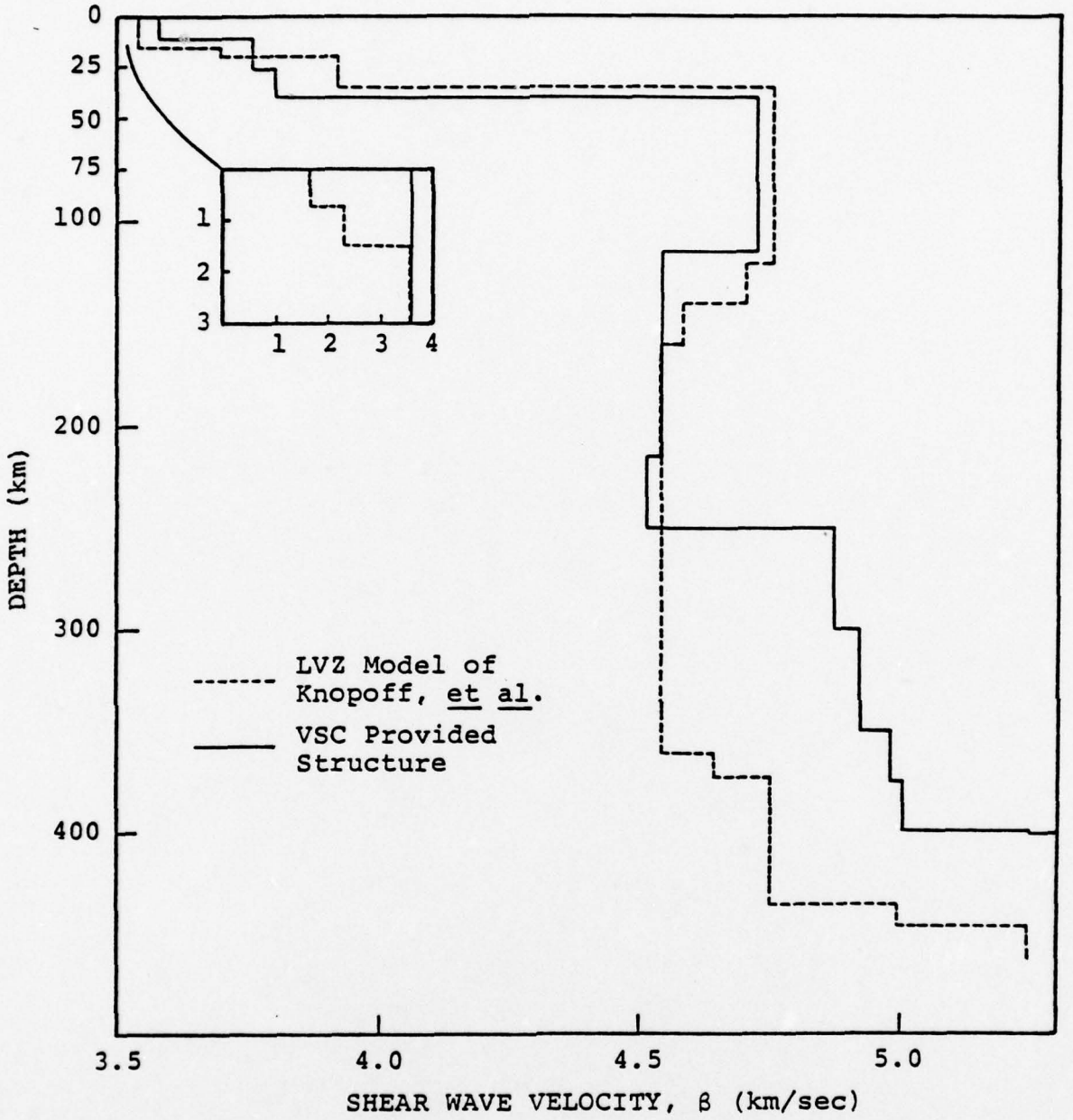

Figure 11. The shear wave velocity-depth profile is plotted for two earth models.

The Love wave phase and group velocities and source-depth independent amplification $\underset{\sim}{A}_L$ (Harkrider, 1964) for the VSC structure of Figure 11 are plotted in Figure 12 for periods down to one second. There is also a depth and frequency dependent term which is not plotted here. In Figure 12 the group velocity stationary phase at about 3.5 km/sec is clearly apparent. Associated with the sudden drop in the group velocity from 4.5 to 3.5 km/sec is a sudden increase in the $\underset{\sim}{A}_L$. Thus, the higher group velocity waves are much less strongly excited.

Similar plots are shown for Rayleigh waves in Figure 13. These plots point out a difficulty with the structure used for the calculations. At short periods the fundamental mode has a group velocity that is not much smaller than 3.5 km/sec. Adding slower sedimentary layers near the surface would cause the fundamental mode to drop to substantially lower velocities at short periods.

Some typical theoretical seismogram calculations for transverse Lg are shown in Figures 14 and 15. The modes computed are those for which the phase and group velocities and amplification are shown in Figure 12. The source is a strike-slip double-couple and the azimuth is 22.5° from the strike. The ground motion is filtered by a WWSSN long period seismometer which peaks at 15 seconds. On each seismogram is given the peak-to-peak amplitude in microns at 15 seconds.

In Figure 14 we compare the Lg at two distances and two source depths. We notice that at these shallow depths the seismogram is dominated by the fundamental mode. The amplitudes of the higher modes decrease rapidly with increasing mode number. The rate of attenuation of the peak amplitude for each mode between these two distances is shown on the figure. The distance attenuation is generally more rapid for the higher modes, though this is not always the case for these examples. Unfortunately, the final summed seismograms do not look very

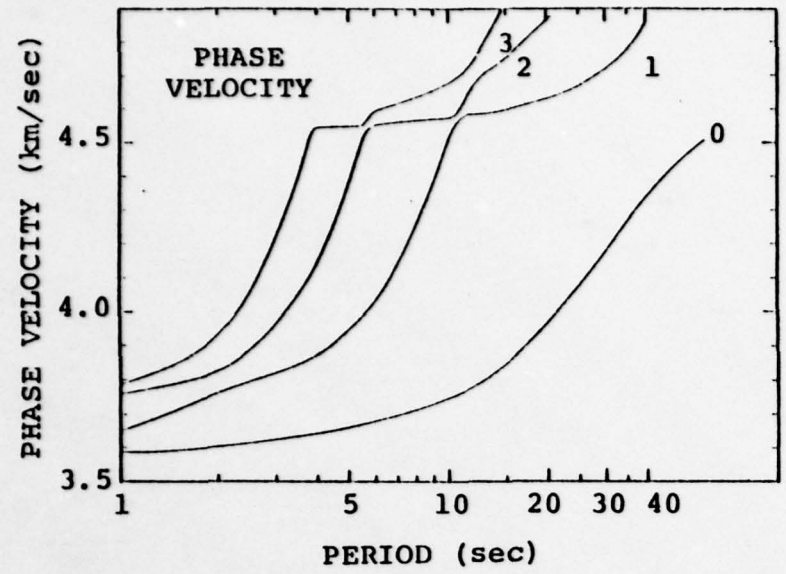

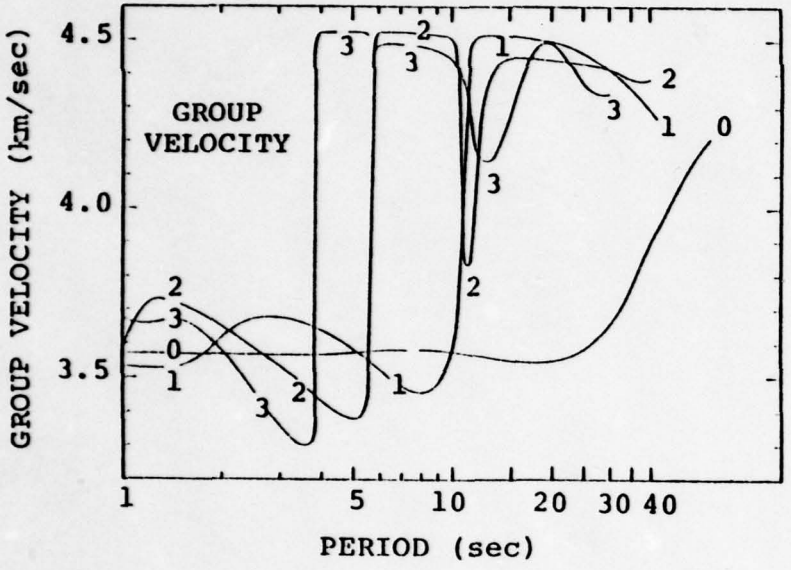

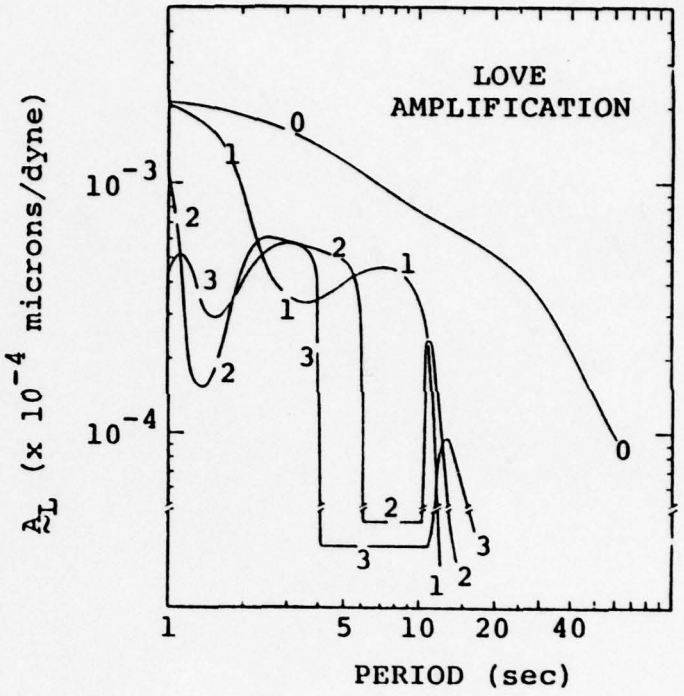

Figure 12. The Love phase and group velocities and depth-independent amplification are plotted for the VSC provided structure of Figure 13. The fundamental (0) and first three higher modes are plotted.

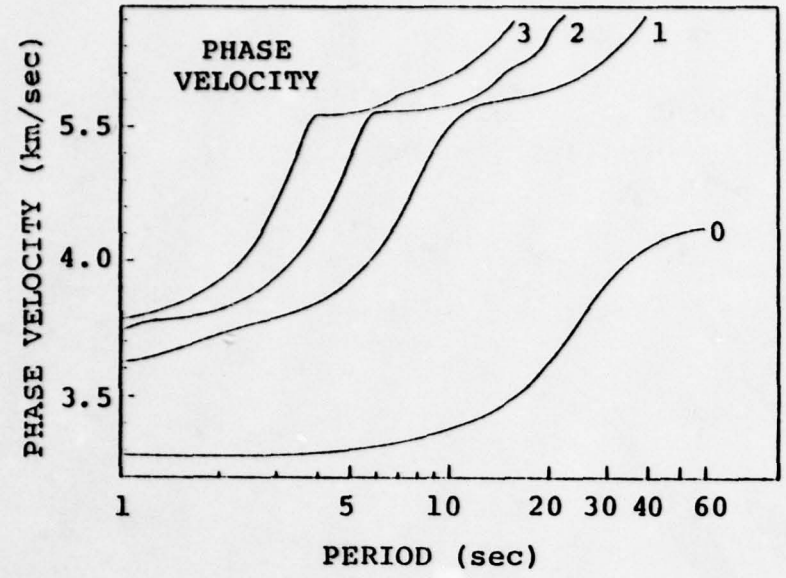

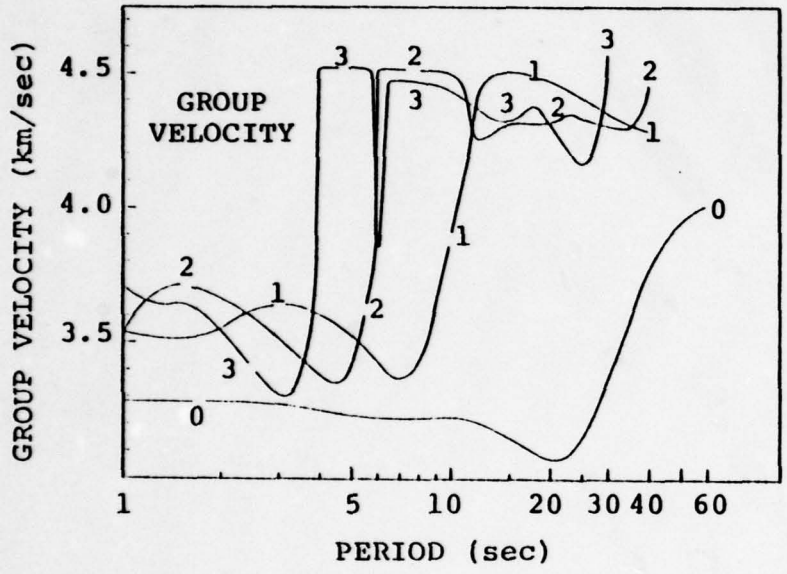

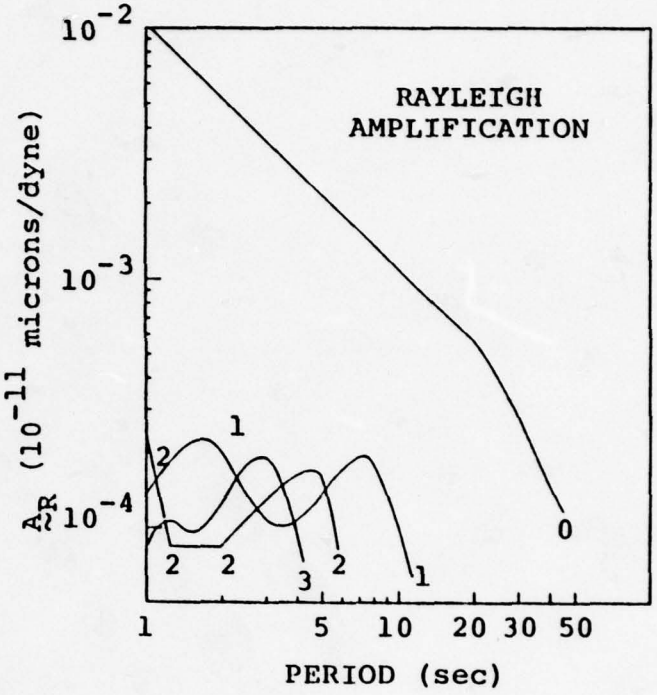

Figure 13. The Rayleigh phase and group velocities and depth-independent amplification are plotted for the VSC provided structure of Figure 13. The fundamental (0) and first three higher modes are plotted.

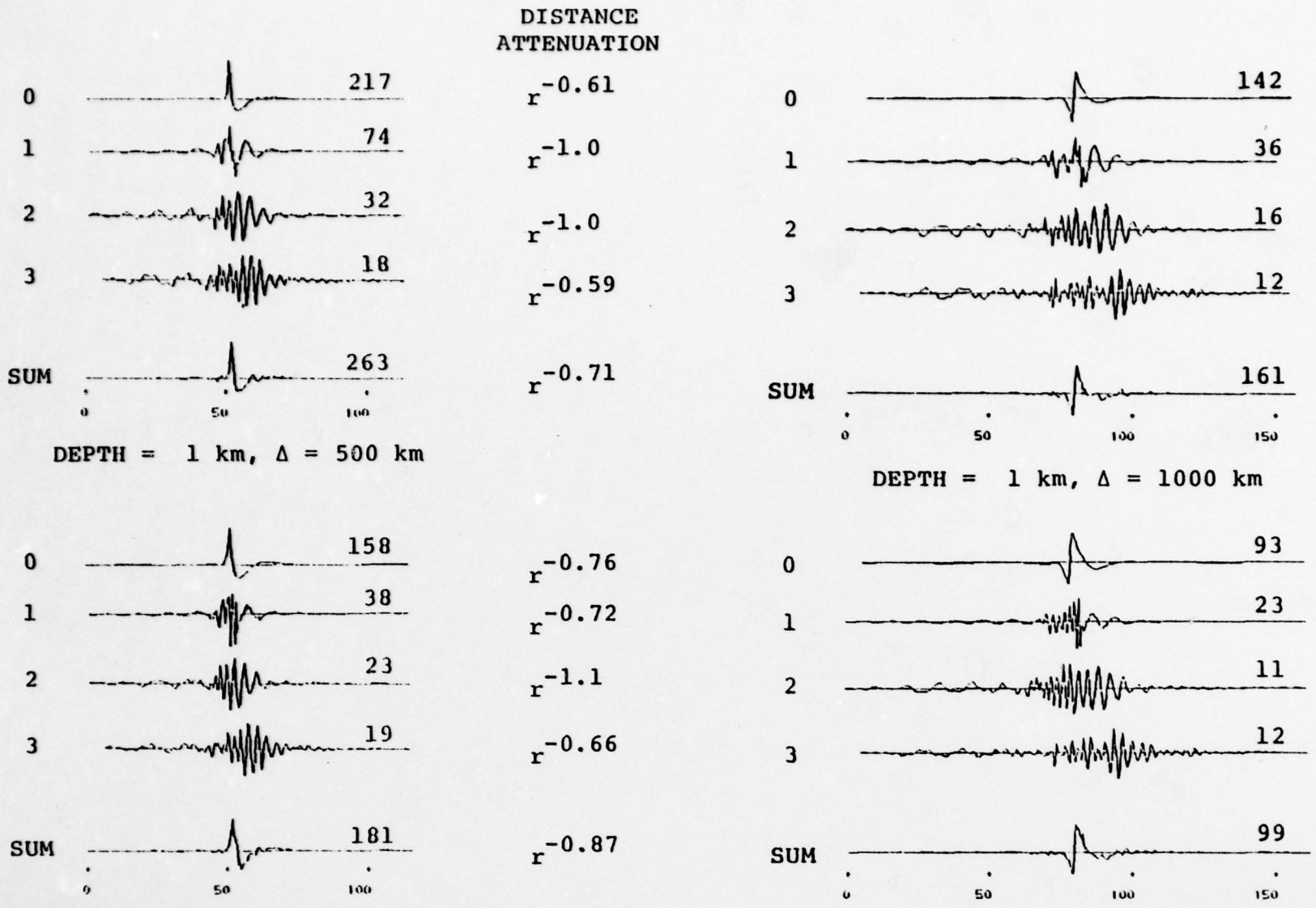

Figure 14. Transverse Lg component seismograms for the fundamental (0) and first three higher modes are compared for two depths and two distances. The motion has been filtered by a WWSSN-LP seismometer and the peak-to-peak amplitudes in microns at 15 seconds are shown on each record. The distance attenuation computed from the two peak amplitudes at each depth is shown in the center.

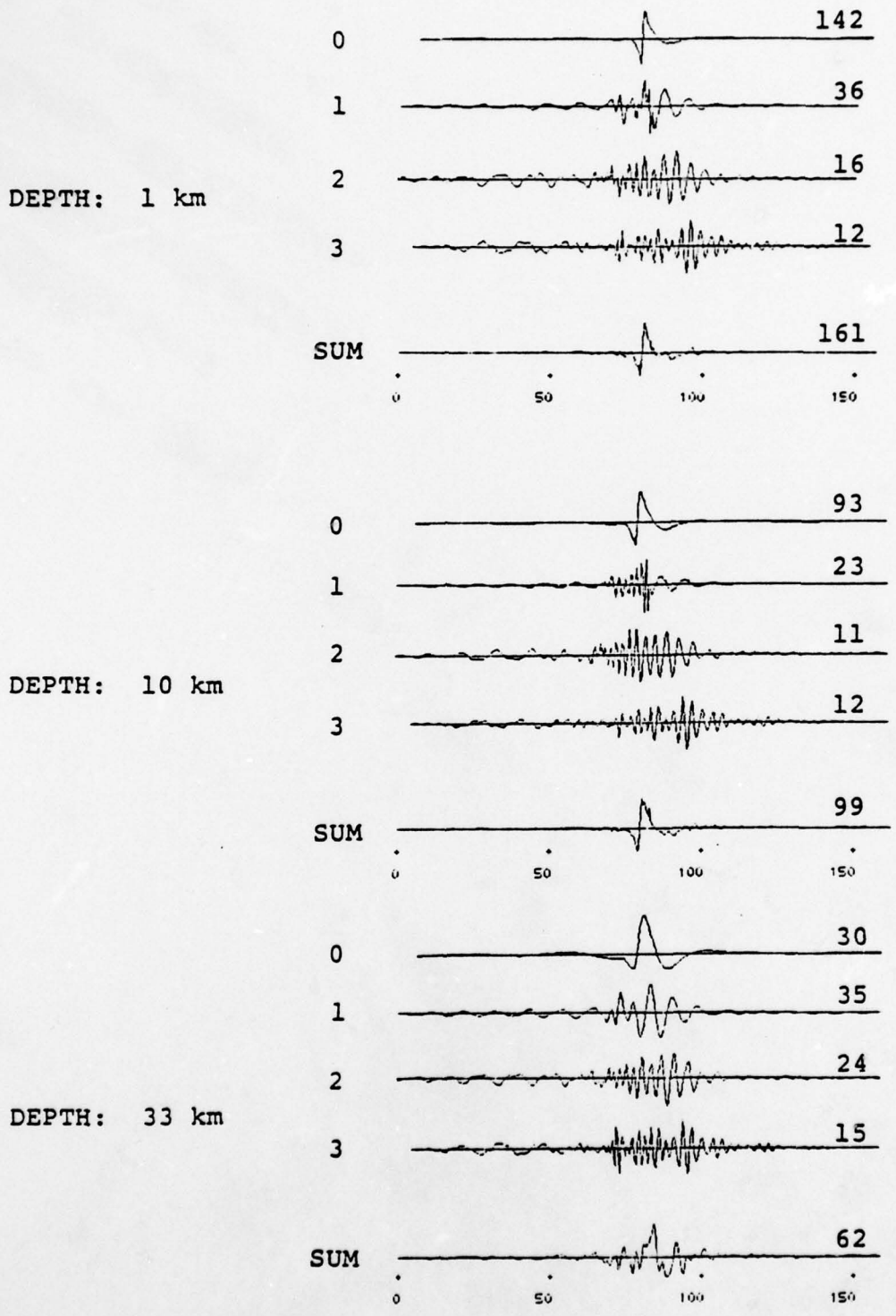

Figure 15. Transverse Lg component seismograms are compared for three source depths at a range of 1000 km.

much like observed data. Much of this can be attributed to the overly simple crustal model used.

In Figure 15 we compare the transverse Lg seismograms at 1000 km for three depths. At 33 km depth the fundamental mode no longer is the largest and the four modes computed are roughly the same size. The summed seismogram is a bit more complex, but still bears little resemblance to observations of the surface waves from earthquakes.

The actual source used for the seismograms of Figures 14 and 15 was the double-couple contribution to a composite source made up of an explosion plus a tectonic release component. The ratio between the two components is that derived by Toksöz and Kehrer (1972) for the PILEDRIVER event; that is, F = 3, where the F factor represents the ratio between the explosion and double-couple portions of the field. With F this large, the double-couple radiation dominates at most azimuths.

In Figure 16 we show the Rayleigh waves from the composite source. Again, the azimuth is 22.5° from the strike of the double-couple. They are compared to the Rayleigh waves from the explosion (spherically symmetric) portion of the field alone. Addition of the double-couple makes some difference in the waveforms. However, in either case the higher modes make almost no contribution.

The examples in Figures 14 through 16 are not particularly interesting because of the overly simple crustal model used in the calculations. Therefore, the scaling properties of the Lg phase on these theoretical records are not very useful. However, they do demonstrate the capability to compute synthetic seismograms at this range. This capability could be exercised with more realistic earth models to determine the theoretical dependence of Lg on the source and path parameters.

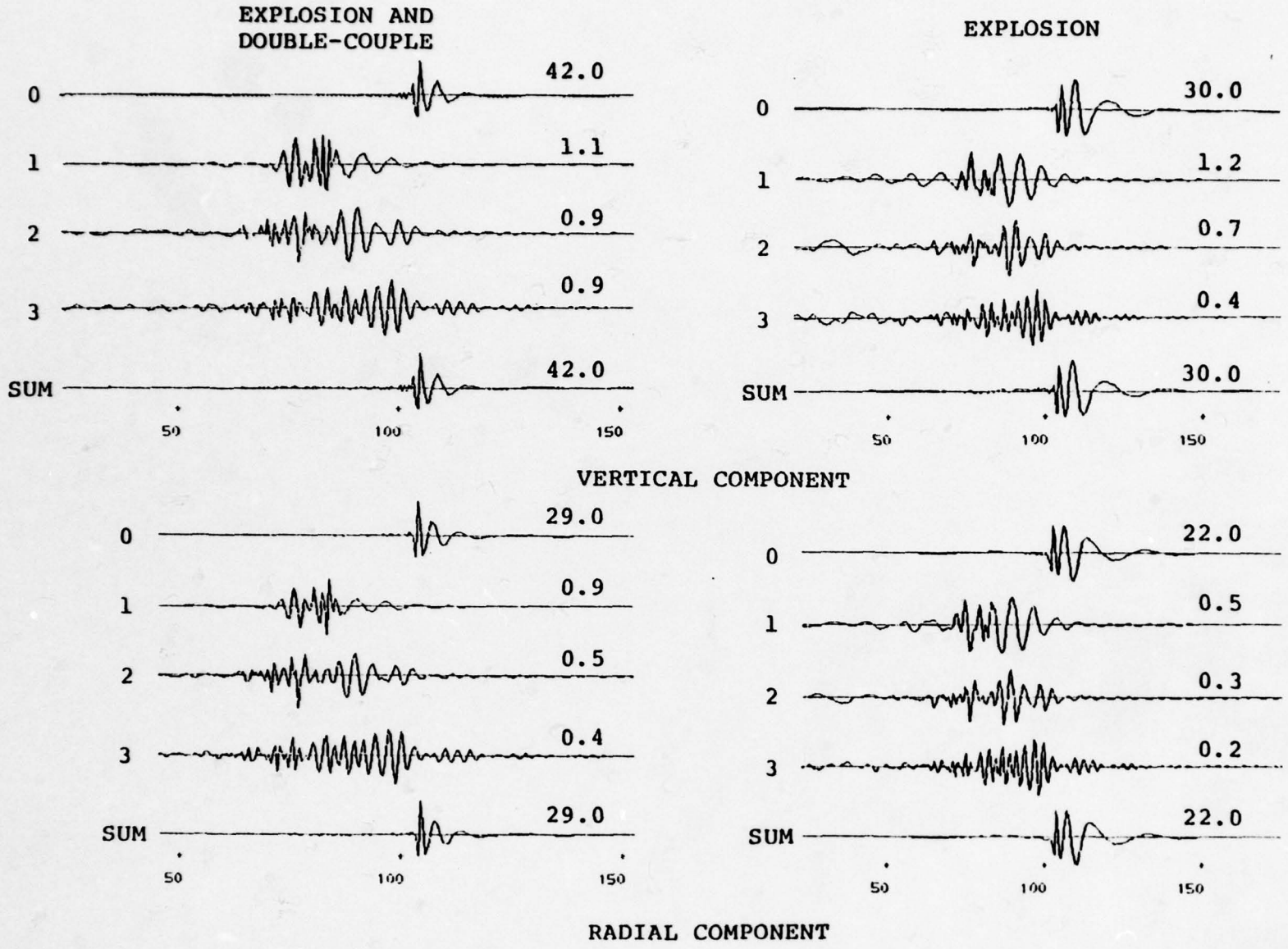

Figure 16. The Rayleigh waves from a composite source made up of an explosion plus a tectonic release generated double-couple are compared to the waves from the explosion alone. The range is 1000 km and the source depth is 1 km.

V. ANALYSIS OF SURFACE WAVES FROM THE FRENCH TEST SITE IN THE SAHARA

5.1 INTRODUCTION

Surface wave recordings from stations in and near Africa were used to study the French Sahara underground event SAPHIRE (27 February 1965). The objective of this study is to better understand the factors that control the amplitude and waveform of explosion-generated surface waves at regional and teleseismic distances. A thorough understanding of these factors is required if surface wave signatures are to be a reliable source of information about seismic source parameters.

The approach taken in this study is the same as in an earlier study under this contract (Bache, Rodi and Harkrider, 1978) in which we modeled Rayleigh waves from NTS explosions. To model the effects of earth structure, we invert the observed dispersion for each path to obtain a model of the average crust and upper mantle structure along the path. These path models and a model of the structure near the source should largely account for the waveforms of the observed surface waves if the theory we use is appropriate. To test this, we compare the observed waveforms to synthetic seismograms generated from our earth models and a trial model of the source. If the waveforms are matched successfully, we can then interpret the surface wave amplitudes at the stations in terms of the source function.

This approach and its theoretical basis are described in more detail in the next subsection. Subsequent subsections present the surface wave data, inversion results and seismogram synthesis results for the SAPHIRE event.

5.2 MODELING PROCEDURE

The time-domain amplitude and waveform of surface waves depend on the characteristics of both the source and

propagation path. To model this dependence we use a modification of Harkrider's (1964, 1970) theory of surface wave generation by point sources in plane-layered media. The modification accounts, in an approximate way, for the transmission across the boundary between the source region and the rest of the path to the receiver. Thus, the earth may be approximated by two one-dimensional models, the first representing the structure near the source and the second representing the average structure along most of the path.

According to the theory, the major contributions to surface wave spectra can be broken down as follows (see Harkrider, 1964, 1970 and Bache, Rodi and Harkrider, 1978 for notation and further details):

Amplitude Spectrum

A1. Source-independent amplitude response of path structure ($\underset{\sim}{A}_{R2}$ for Rayleigh waves, $\underset{\sim}{A}_{L2}$ for Love waves).

A2. Dissipative attenuation along path ($e^{-\gamma_2 r}$).

A3. Source-independent amplitude response of source-region structure ($\underset{\sim}{A}_{R1}$ and $\underset{\sim}{A}_{L1}$).

A4. Source-depth-dependent modal excitation (K_{S1} for explosive source).

A5. Radiation pattern of source (depends on source size, time history and geometry).

Phase Spectrum

P1. Dispersion along path ($\omega r/c_2$).

P2. Initial phase of source (depends on same factors as A5).

These phenomena are most easily understood in the frequency

domain where they are nearly separable. To understand them in the time domain, we must rely on Fourier transform theory.

The biggest task in our modeling procedure is the estimation of the average crust and upper mantle structure for each source-receiver path. This is accomplished by inverting the observed dispersion for each path using other data such as refraction results as constraints. With certain assumptions about the initial phase of the source, path dispersion can be determined nearly independently of other contributions to the surface wave spectra. Specifically, we assume small phase and group delay at the source. Rayleigh and Love wave group velocities are then obtained by narrow-band filtering and Hilbert transform techniques. To determine Rayleigh wave phase velocities, we assume the spectra are dominated by the explosive component of the source which has a very small initial phase. However, the phase spectrum is indeterminate by a multiple of 2π and there are a multiplicity of phase velocity curves for each path. To determine Love wave phase velocities requires a more complete knowledge of the source radiation pattern.

We invert the phase and group velocity data for each path by formal linear inversion techniques to determine models of seismic velocity and density. A first test of the applicability of our theory is whether reasonable plane-layered models can be found that fit the observed dispersion and whether the models for different paths describe a consistent picture of the entire region of study.

A source-region model is derived from one or more of the path models, modified as necessary to agree with any available information about the near-surface structure of the source region. As a result, the models we invert from the observed dispersion (P1) are expected to account for spectral contributions A1, A3 and A4 as well. (The depth of the

source is assumed known.) A Q or γ model is determined from global or regional (if available) attenuation data and is used to account for A2. These contributions (all but A5 and P2) determine the waveform of the surface waves. Using our path and source-region models plus a trial model for the source, we synthesize seismograms for comparison with the observations. The agreement in waveform is a test of our modeling procedures and the theory they are based on. Furthermore, if our modeling is adequate, the observed and synthetic amplitude spectra at each station should differ at long periods only by a constant factor. The values of this factor at the various stations can be used to infer the difference between the true source parameters and the parameters of the trial source model.

5.3 SURFACE WAVE OBSERVATIONS

Figure 17 shows the location of the Hoggar (HOG) test site in Algeria, together with the paths to eleven WWSSN stations in and near Africa. Reported here are the results from modeling the SAPHIRE surface waves recorded at four of these stations (HLW, SHI, AAE and NAI) plus another not plotted (X). Table 4 gives a description of the five paths studied. In Figure 18 are plotted the seven seismograms analyzed for this report. These include the vertical component from each station and the transverse component from HLW and AAE. All of these data were hand-digitized from film-chip reproductions. The transverse component data were obtained by rotating the horizontal recordings with respect to the great circle path from source to receiver.

The dispersed surface wave is easily identifiable on most of the seismograms in Figure 18, but some are clearly contaminated by noise or other arrivals. In particular the AAE transverse component is very complex. Also, the Rayleigh

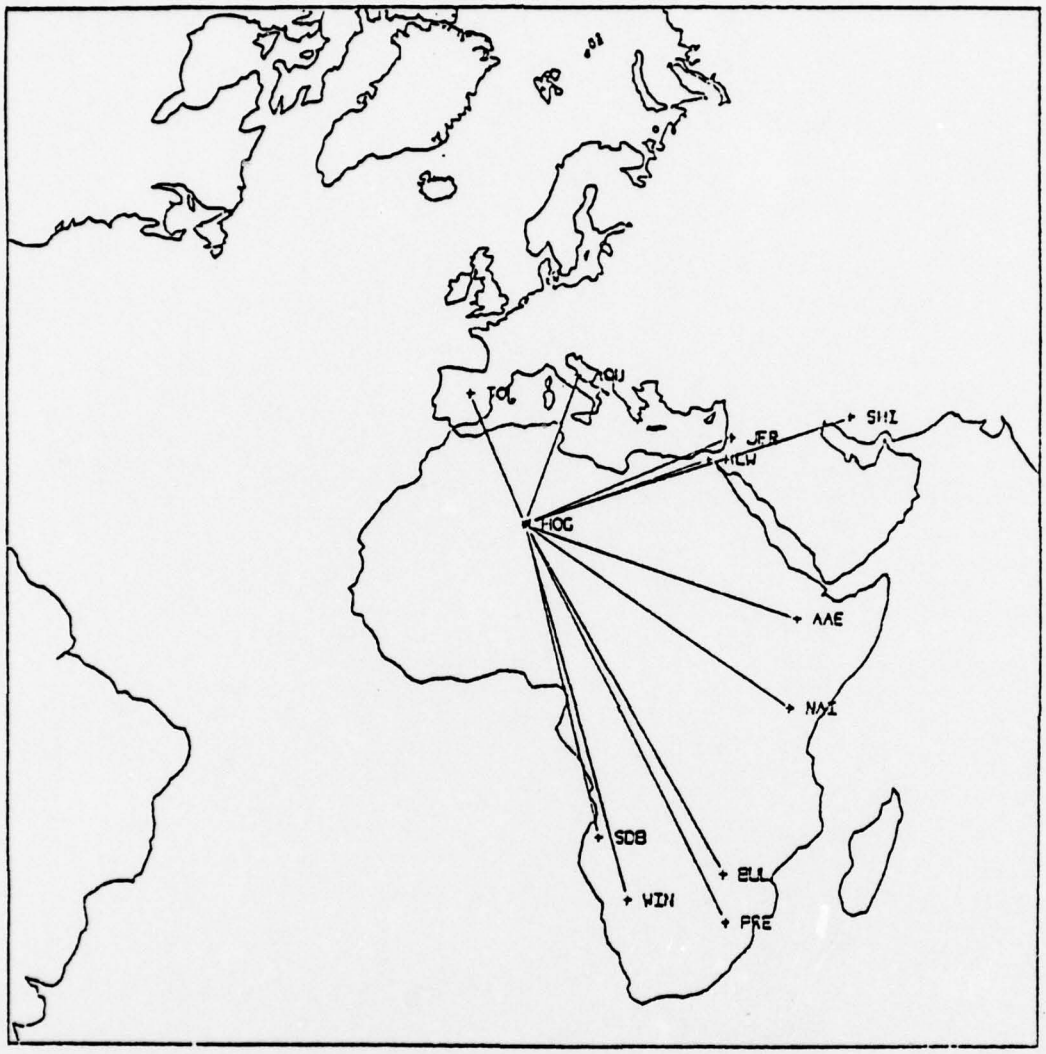

Figure 17. The location of the Hoggar test site and the paths to eleven WWSSN stations are shown in a polar projection centered on the test site.

TABLE 4

STATIONS USED IN THIS STUDY

Station Code	Location	Distance from Event	Azimuth from Event	Instrument
HLW	Helwan, Egypt	2688 km	70	WWSSN (15-100)
SHI	Shiraz, Iran	4729	72	WWSSN (30-100)
AAE	Addis Ababa, Ethiopia	3948	109	WWSSN (15-100)
NAI	Nairobi, Kenya	4426	125	WWSSN (15-100)
X	Unidentified	---	---	---

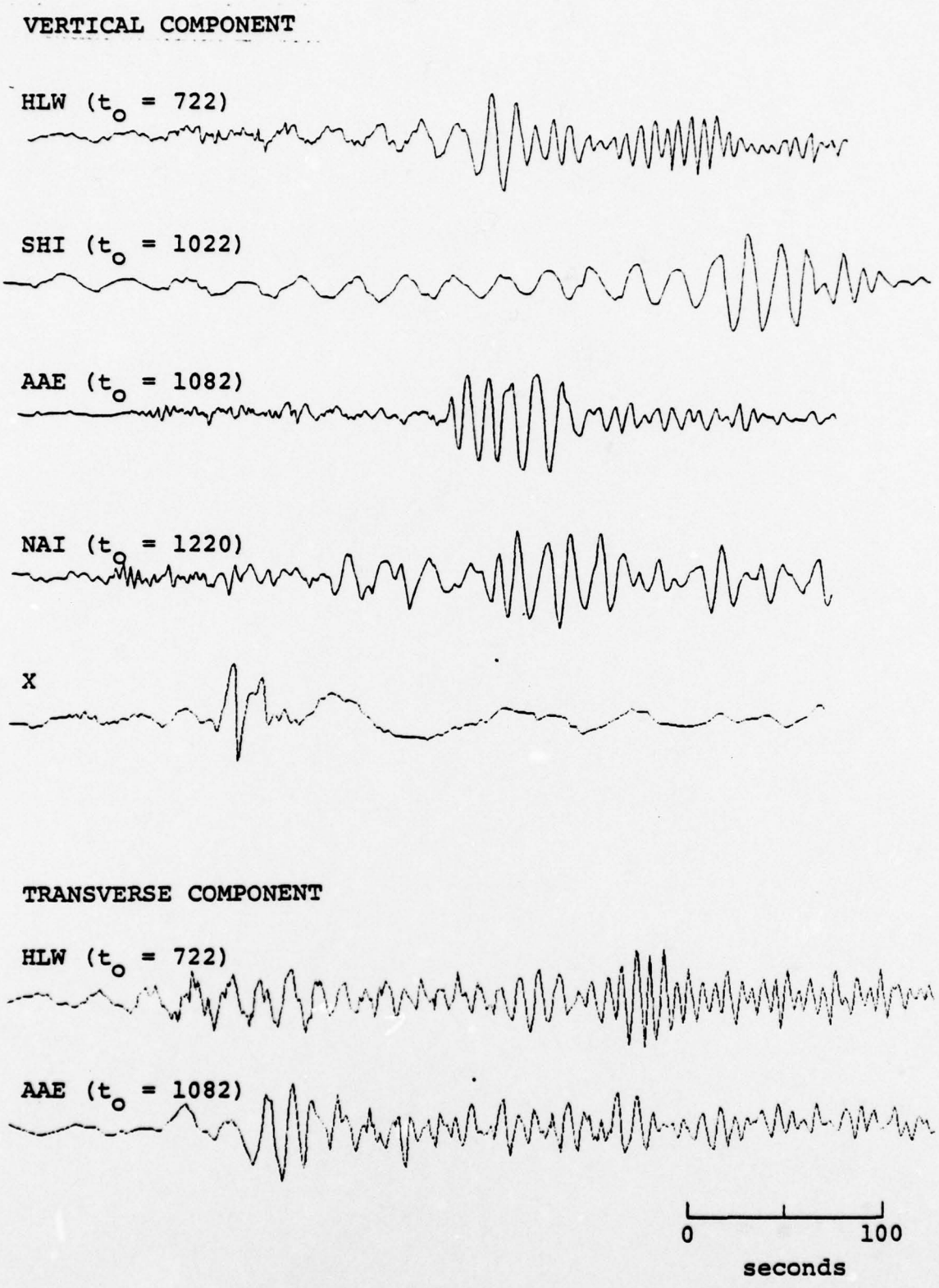

Figure 18. The SAPHIRE seismograms analyzed in this study are shown, with t_o denoting the start time (in seconds) of each record relative to the origin time.

wave has obviously leaked onto the HLW transverse component, suggesting that the direction of propagation for the HOG-HLW path is not great-circle. Another example of contamination is the very long-period trail behind the peak arrival on the X vertical component.

Group velocities were determined from all seven seismograms with narrow-band Gaussian filtering. For the Rayleigh waves, clear fundamental-mode group arrivals could be obtained at periods as low as 5 and as high as 35 s, but mainly in the 7 to 25 s range. Love wave group velocities for HLW and AAE were obtained from 12 to 25 s. Figure 19 compares the group velocities determined for the five paths and used in the inversion for the path structures.

The determination of phase velocities presented much more difficulty, but was pursued because they add substantially to the resolving power for earth structure. Phase velocity (c) is derived directly from the surface wave phase spectrum (ϕ) through the relation

$$\frac{\omega r}{c(\omega)} = \phi_s(\omega) - \phi(\omega) + n2\pi, \qquad (5.1)$$

where r is the source-receiver distance and ϕ_s is the initial phase of the source, including radiation pattern effects. For Rayleigh waves we assumed $\phi_s = -3\pi/4$, a close approximation to the initial phase of the vertical Rayleigh wave displacement due to an explosive source. In the case of Love waves, we did not feel confident in assuming ϕ_s, so no Love wave phase velocities were used for the inversions reported in this report.

A difficulty with deriving phase velocity from Equation (5.1) is the possible contamination of the phase spectrum by noise, body waves or higher modes. This problem was handled by time-domain windowing before obtaining the Fourier spectrum in order to insure that the spectrum at the periods of interest (5 to 30 s) was dominated by fundamental-mode Rayleigh wave.

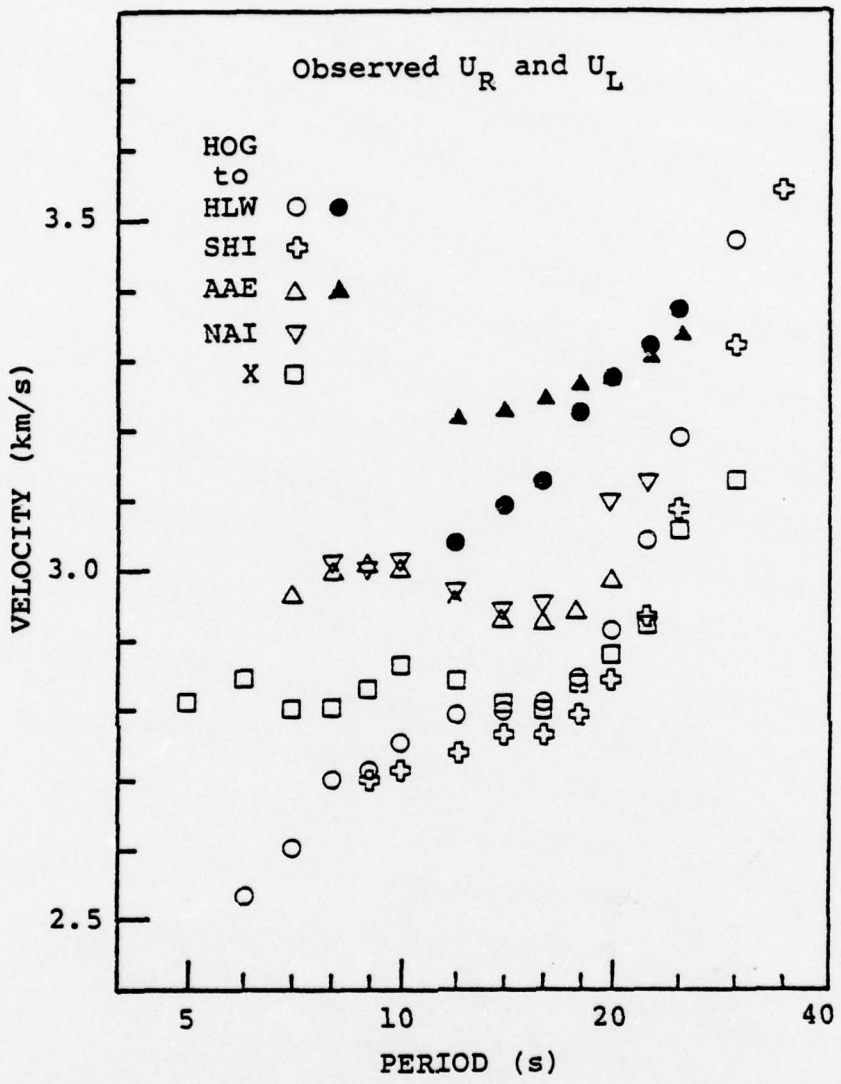

Figure 19. The Rayleigh-wave group velocities (U_R) determined for five paths from Hoggar test site are plotted as open symbols. Love-wave group velocities (U_L) are plotted as solid symbols.

We checked this by comparing the group velocities implied by our phase velocity estimates with the narrow-band group velocities. (This can be done independently of the value of n in Equation (5.1)). Phase velocities at periods for which the agreement was poor or for which the spectral amplitude was small were rejected.

A second problem with determining phase velocities is the fact that the integer n in Equation (5.1) is indeterminate from the seismograms alone. Other information is needed to ascertain which of the possible phase velocity curves implied by Equation (5.1) is most nearly correct. For the long paths and short periods available for this study, the possible curves do not differ a great deal. However, we were able to choose n with some confidence for the HOG-X path. Implausible mantle shear velocities (> 5 km/s at 70 km depth) resulted from inverting the HOG-X phase-velocity curve adjacent to the one chosen (n differing by 1). For the other paths, we chose n such that the phase velocity curves for all the paths were most nearly aligned at the longest available periods.

The final phase velocities determined for the five paths are plotted in Figure 20. Table 5 gives the approximate shifts to these data that result from altering n by $\pm$ 1 from the values chosen. Our final phase velocity data are consistent with long period surface wave observations reported from previous studies of east African paths. Knopoff and Schlue (1972) found c(20s) $\doteq$ 3.6 km/s for a path from AAE to NAI. Gumper and Pomeroy (1970) found c(30s) $\doteq$ 3.92 for a north-south path from HLW to Lwiro, Republic of the Congo (west of NAI).

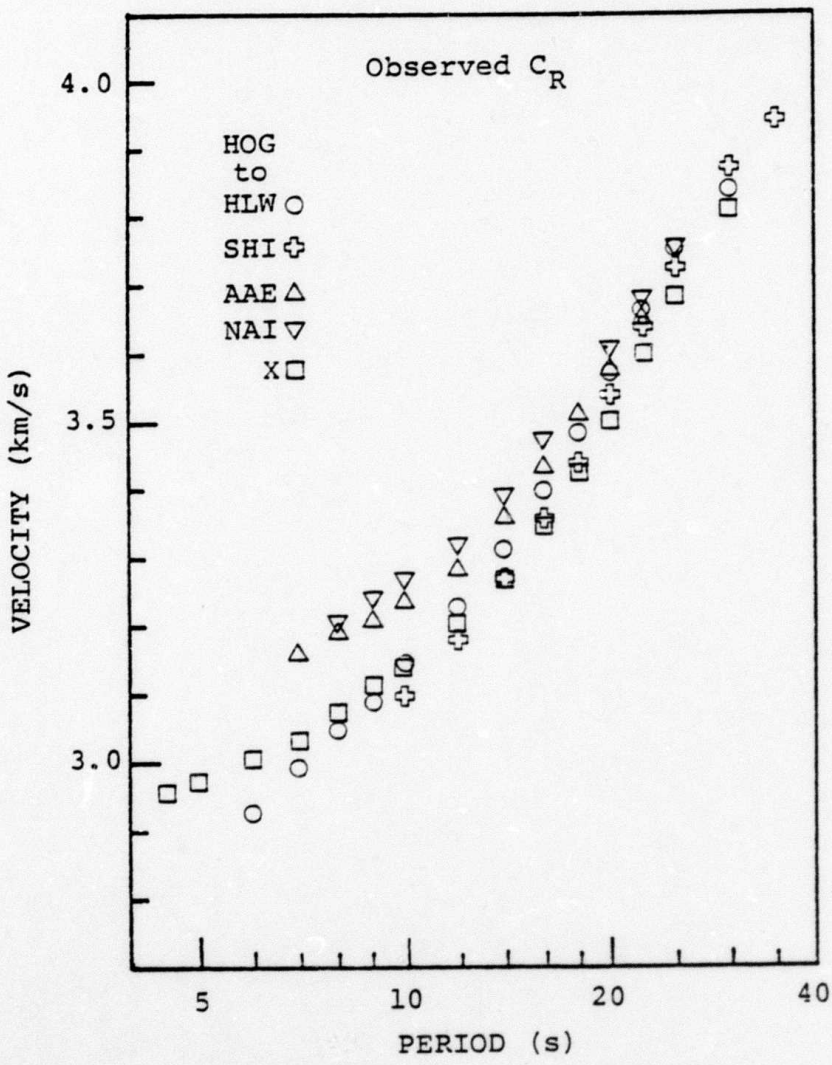

Figure 20. The observed Rayleigh-wave phase velocities (C_R) are shown for five paths from Hoggar test site.

TABLE 5

APPROXIMATE PHASE VELOCITY UNCERTAINTIES
DUE TO 2π AMBIGUITY IN PHASE

	Phase Velocity Uncertainty (km/s)		
Station	Period = 20s	25s	30s
HLW	0.10	0.13	0.16
SHI	0.05	0.07	0.10
AAE	0.07		
NAI	0.06	0.08	

5.4 INVERSION RESULTS

The dispersion data for each of the five African paths were inverted with the iterative linear inversion technique employed in an earlier study of NTS surface waves (Bache, et al., 1978). With this technique, phase and group velocities are simultaneously fit with a smooth plane-layered model of crustal and upper mantle shear velocity (β), compressional velocity (α) and density (ρ). The inversion model obtained for a given path represents an estimate for the average structure along that path.

It is desirable to build additional constraints into the inversion of dispersion data in order to supplement their resolving power. In addition to the smoothness requirement, our inversion algorithm allows for two types of constraints. First, linear α-β and ρ-β relationships may be imposed to compensate for the fact that phase and group velocities are only weakly dependent on α and ρ. Second, the depth to discontinuities (such as the crust-mantle boundary) may be incorporated into the model. In general, dispersion data cannot distinguish a sharp discontinuity from a gradual variation in β with depth. These were the only constraints used to invert the African data. No "guess models" were used.

The model constraints employed are well-suited for incorporating results from previous geophysical surveys, such as Pn velocities and crustal thicknesses determined from refraction studies. While some information of this type is available for the African paths studied here, it was not sufficient for confidently fixing the constraints. Instead, we employed "default" constraints whose primary purpose was to ensure self-consistent and reasonable inversion models. For each of the five paths we constrained α and ρ in both the crust and mantle by

$$\alpha = 1.732\ \beta \qquad \text{(Poisson's ratio = 0.25)}$$

$$\rho = 0.3\ \alpha + 0.9 \qquad \text{(a form of Birch's law).} \qquad (5.2)$$

Using Equation (5.2), the data for each path were inverted for β with and without assuming a crustal thickness. For some paths two or more crustal thicknesses were tried (30, 35 or 40 km). In addition, a 2 km sedimentary layer was incorporated into the inversion models for the HOG-HLW and HOG-X paths because their dispersion data seemed to require low shear velocities near the surface.

Figures 21 through 25 show two or more inversion models obtained for each of the five African paths. The different models shown for each path, corresponding to different assumptions about the crustal thickness, predict only slightly different dispersion. The model dispersion is compared to the observations in each figure.

With the exception of the HOG-AAE models, the inversion models closely agree with all the observed velocity points except those that cannot be fit by a smooth curve. For the HOG-AAE path the inversion models do not simultaneously fit the Rayleigh and Love wave data. Figure 23a shows three inversion models determined from only the AAE Rayleigh phase and group velocity data. They match these data well, but systematically misfit the Love wave group velocities. An inversion of both data sets together (Figure 23b) produces a model that fits the Love wave data slightly better, but the Rayleigh wave data much worse. We do not know the reason for this incompatibility between the Love and Rayleigh data from AAE, but an apparent anisotropy due to lateral variations along the HOG-AAE path is a plausible possibility. In contrast, a simultaneous inversion of Rayleigh and Love wave data from the HOG-HLW path was quite successful.

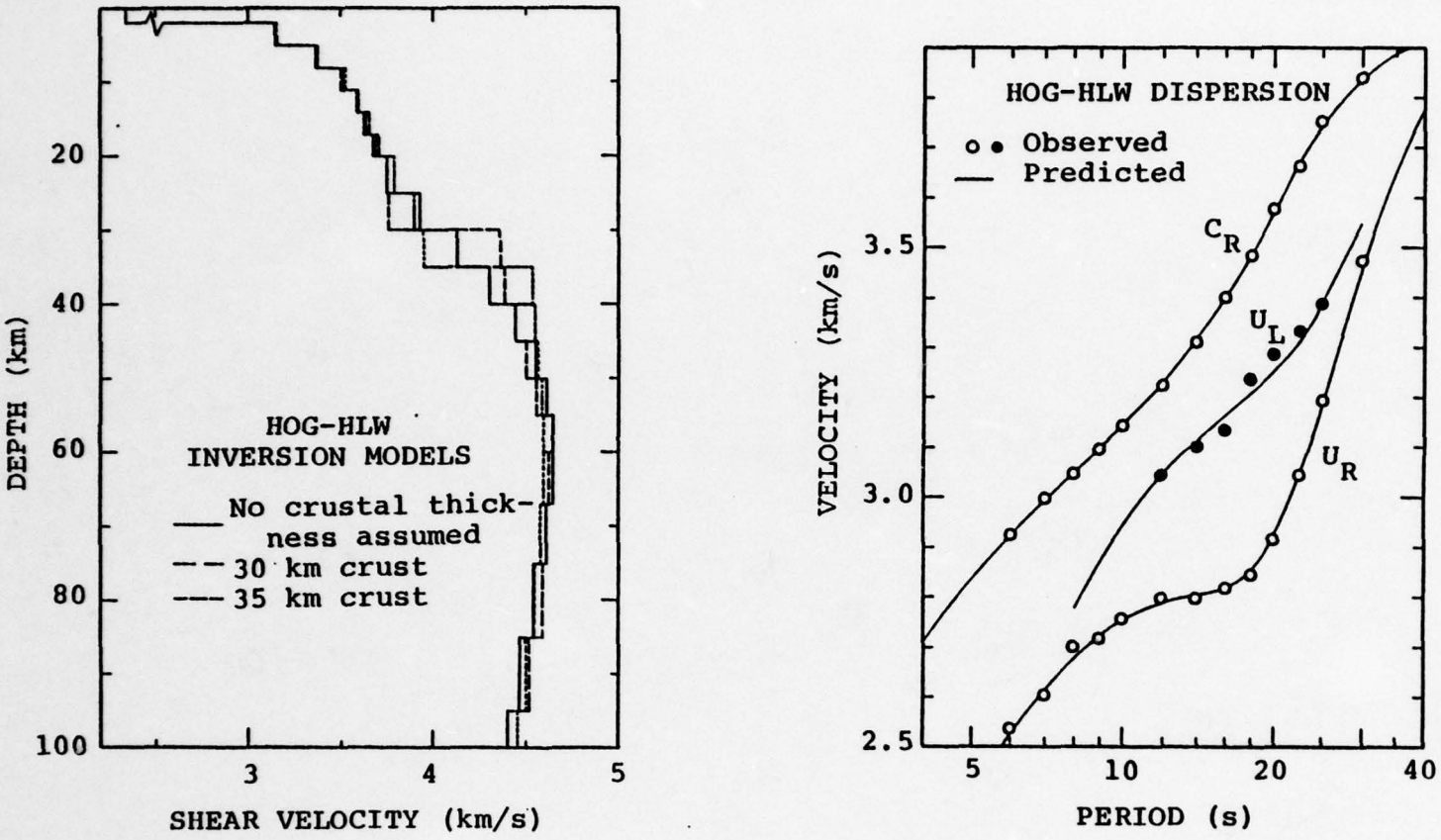

Figure 21. Three models inverted from the HOG-HLW Rayleigh and Love wave dispersion data are shown at left. At right, the dispersion predicted by the model with 35 km crustal thickness is compared to the observed dispersion.

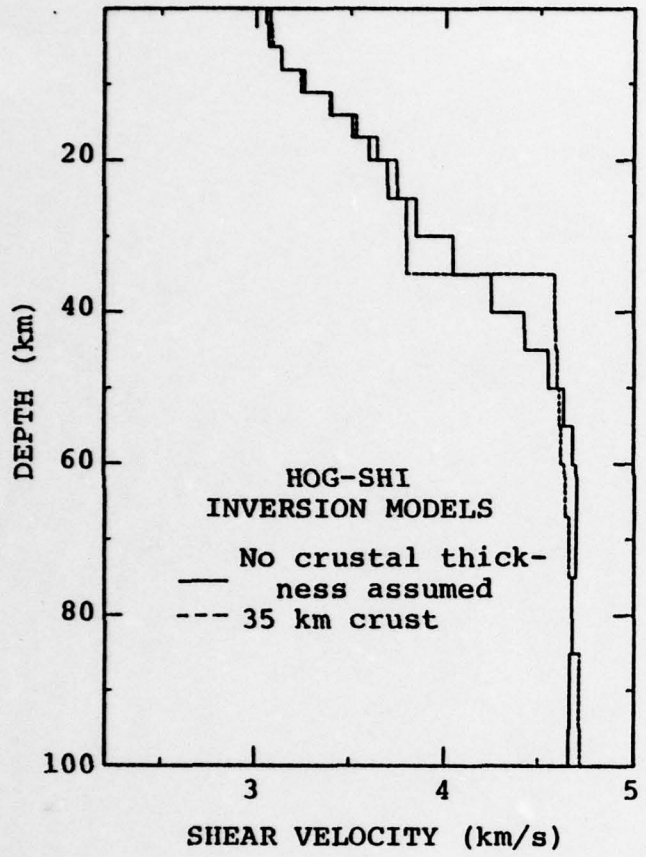

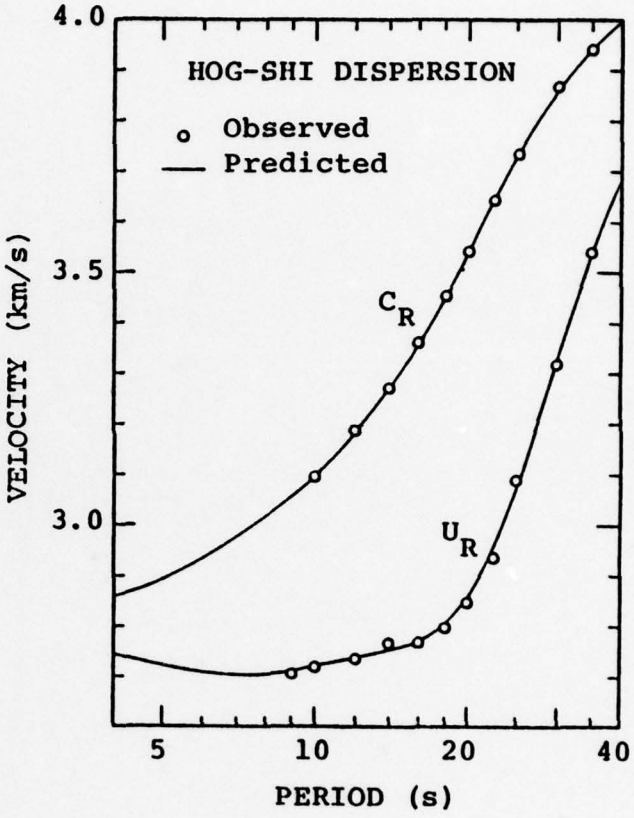

Figure 22. Two inversion models for the HOG-SHI path are shown (left) together with a comparison of the observed dispersion with the predicted dispersion for the model for which crustal thickness was not assumed.

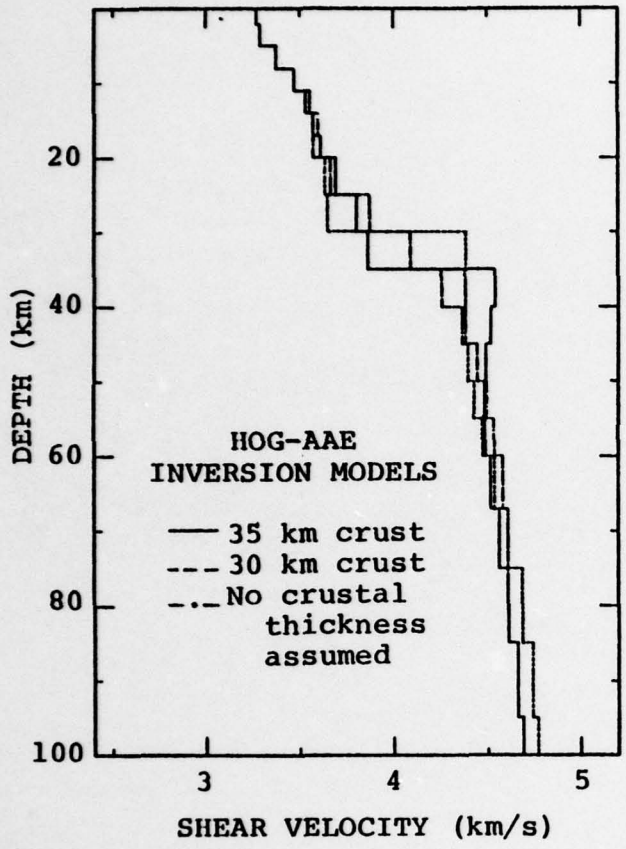

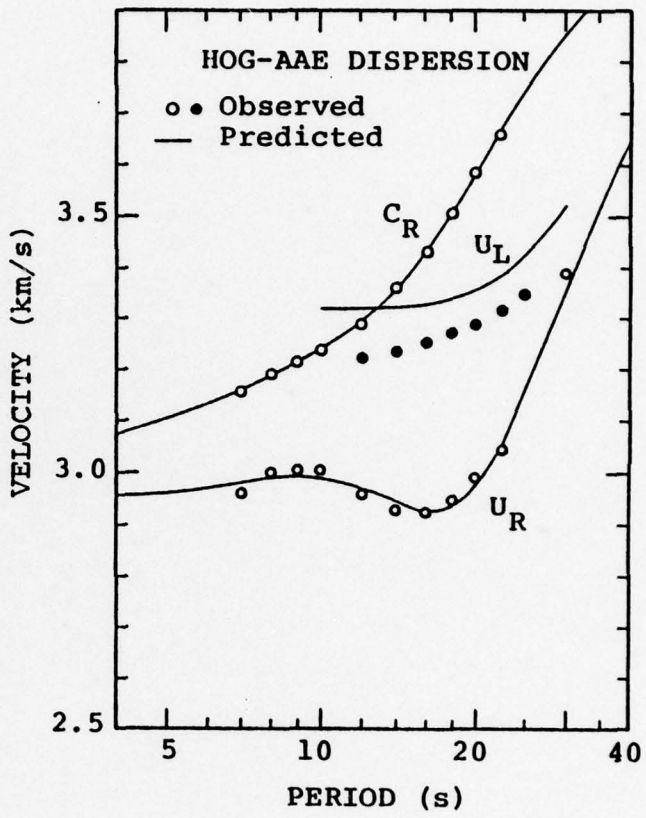

Figure 23a. Three inversion models inverted from the HOG-AAE Rayleigh wave dispersion data are shown at left. At right, the predicted dispersion (Rayleigh and Love) for the model with a 35 km crust is compared to the observed dispersion.

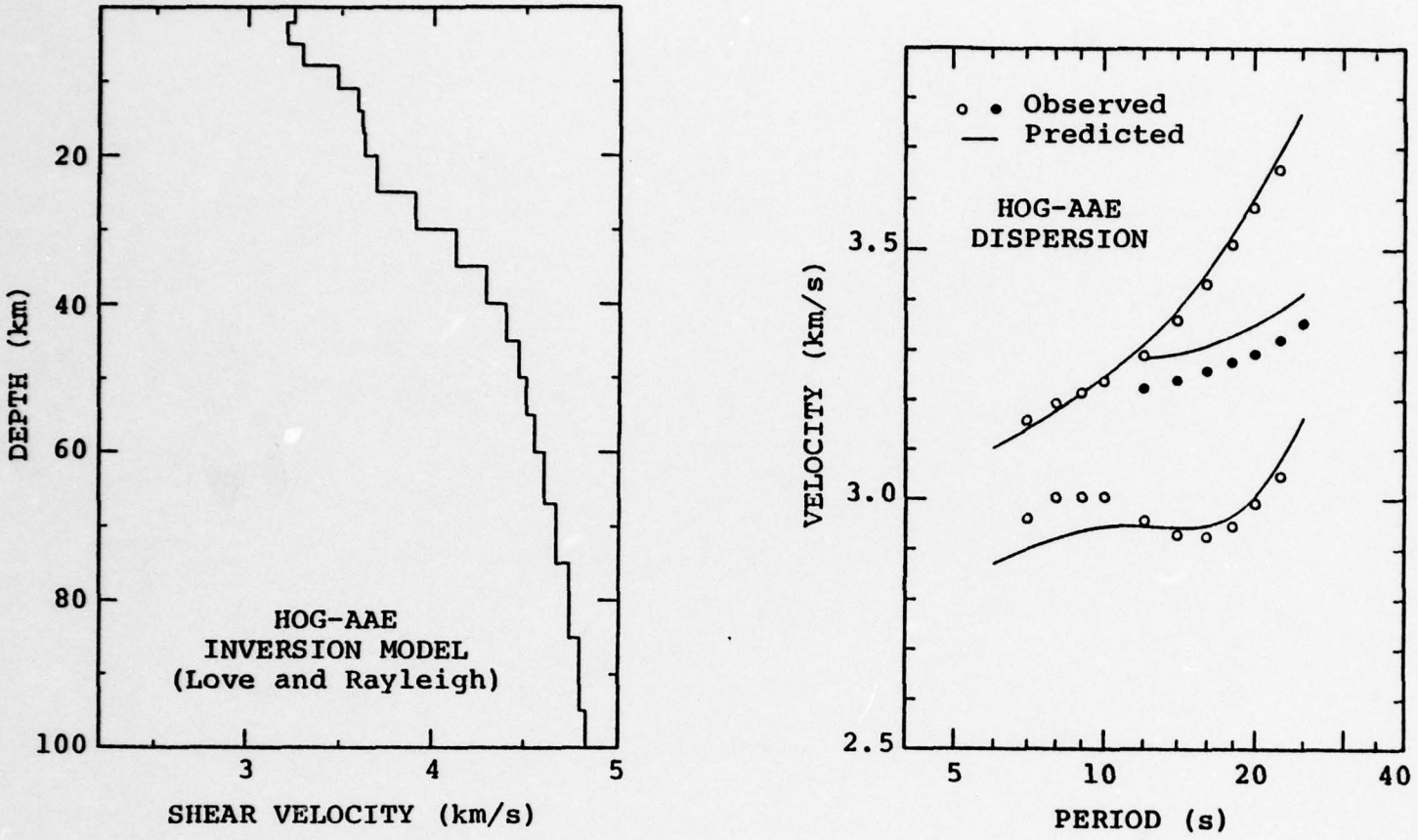

Figure 23b. A model inverted from the HOG-AAE Rayleigh and Love dispersion data with no crustal thickness assumed is shown (left) together with a comparison of its predicted dispersion to the observed dispersion.

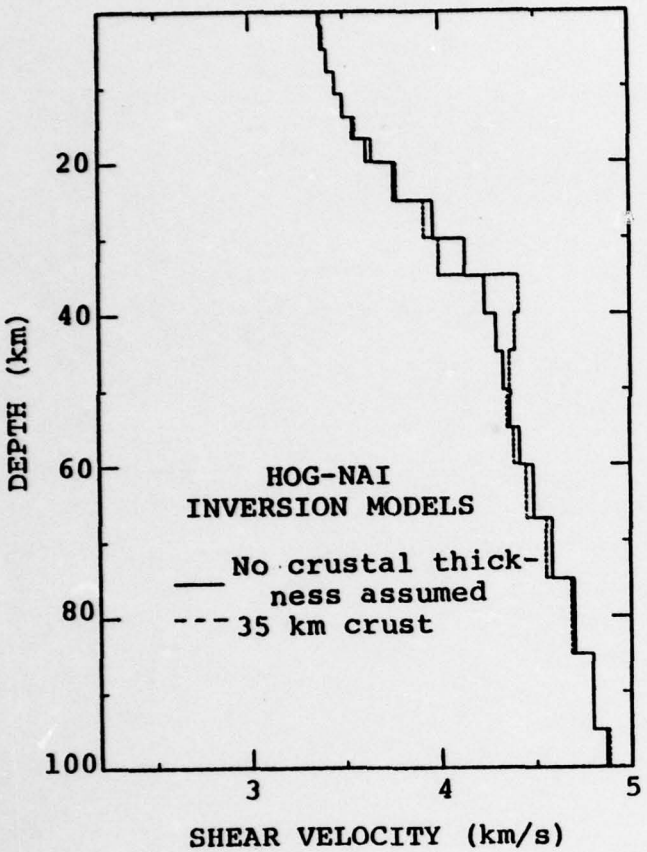

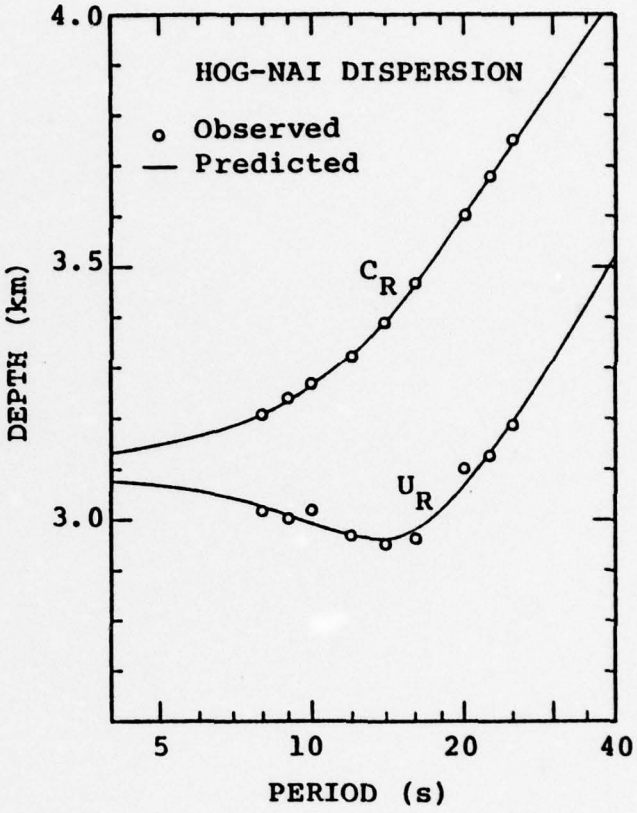

Figure 24. Two inversion models for the HOG-NAI path are shown (left) together with a comparison of the observed dispersion to the predicted dispersion for the model with no crustal thickness assumed.

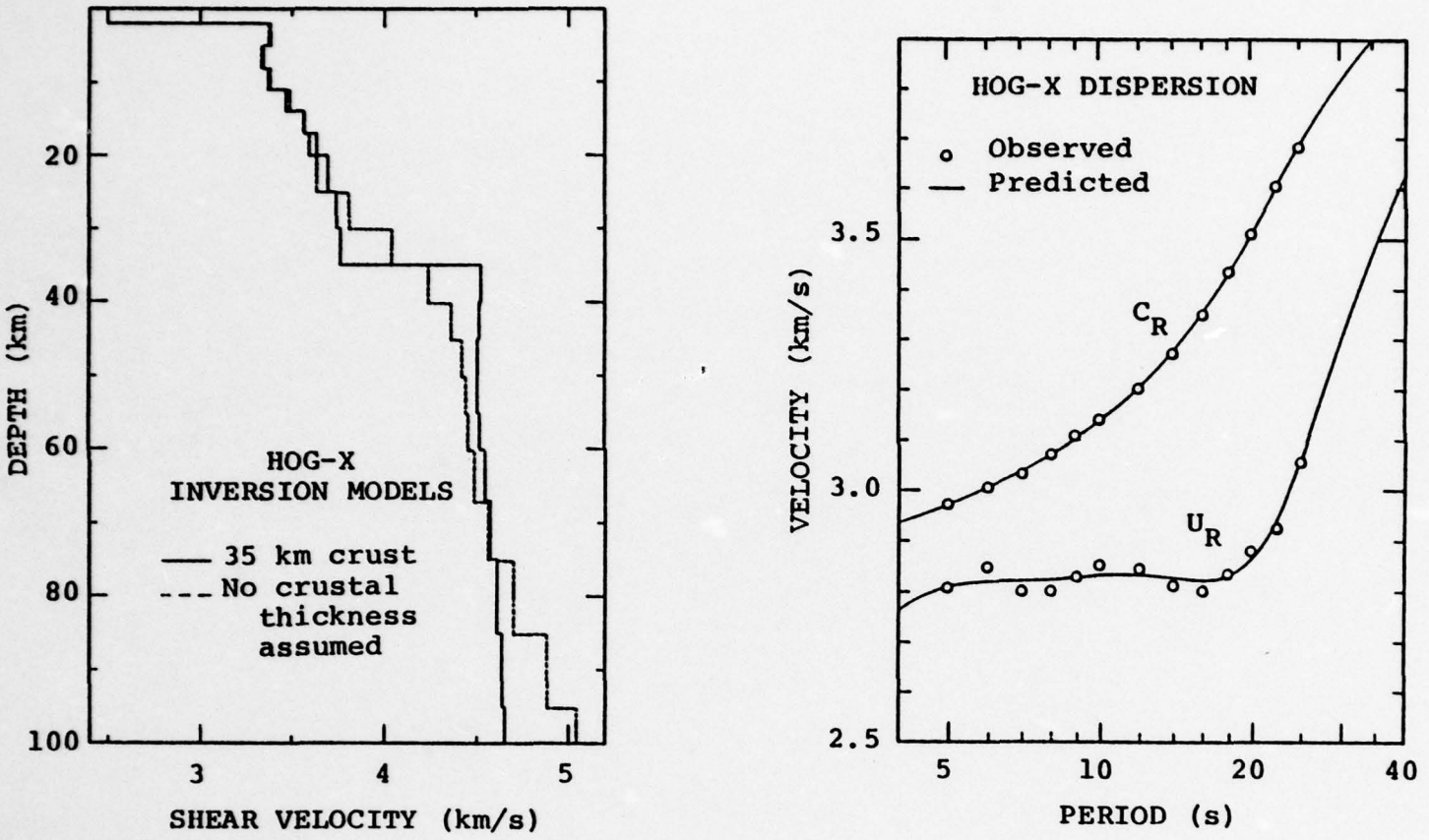

Figure 25. Two inversion models for the HOG-X path are shown (left) together with a comparison of the observed dispersion to the predicted dispersion for the model with the 35 km crust.

We found that models with either no sharp crust-mantle transition or a crustal thickness of 35 km could fit the data for each path. For the HLW and AAE paths, crustal thicknesses of 30 and 40 km also fit the data and we would expect this to be the case for the other paths as well. However, different crustal thicknesses imply different shear velocities at the base of the crust and top of the mantle (e.g., Figures 21 and 23a). Therefore, independent information about lower crustal velocity, Sn velocity, or velocity gradients in the crust and mantle would allow one to narrow the range of plausible crustal thicknesses.

The results of previous studies of African structure provide some basis for judging the inversion models in Figures 21 through 25. Gumper and Pomeroy (1970) analyzed surface waves and short period body waves from numerous African paths, with many in eastern Africa. Their inferred crustal and upper mantle model (AFRIC) is listed in Table 6. Gumper and Pomeroy reported Lg velocities between 3.48 and 3.72 km/s. Lg velocity is an estimate for average crustal shear velocity and our models are consistent with the wide range they observed. Their body-wave observations indicated Sn velocities ranging from 4.55 to 4.72 km/s. For comparison, the approximate Sn velocities from our inversion models are given in Table 7. Our Sn velocities seem to be low for some of the paths. However, Gumper and Pomeroy noted that Sn did not propagate efficiently along paths crossing the African rift, near which AAE and NAI are located. Furthermore, Knopoff and Schlue (1972) inferred low Sn velocities (4.25 to 4.55 km/s) for a surface-wave path from AAE to NAI. In addition, refraction studies near AAE by Searle and Gouin (1971) found Sn = 4.29 km/s. The latter study also reported a very thick crust, up to 48 km, under AAE. A crust this thick will violate our HOG-AAE data. While these studies suggest anomalous structures near the African rift, we must keep in mind that only a small portion of the HOG-AAE and HOG-NAI paths traverses the rift zone.

TABLE 6

AFRIC MODEL OF GUMPER AND POMEROY (1970)

Layer Thickness	Depth to Layer Bottom	α	β	ρ
7.0	7.0	5.90	3.35	2.70
10.5	17.5	6.15	3.55	2.80
18.7	36.2	6.60	3.72	2.85
80.0	116.2	8.05	4.63	3.30

TABLE 7

APPROXIMATE Sn VELOCITIES FROM INVERSION MODELS WITH 35 KM THICK CRUST

Path	Sn (km/s)
HOG-HLW	4.6
HOG-SHI	4.6
HOG-AAE	4.5
HOG-NAI	4.4
HOG-X	4.5

While the inversion models found for each path are reasonable, they have not yet been integrated to give a consistent picture of crustal and upper mantle structure in northern Africa. For example even though the HOG-AAE and HOG-NAI paths are fairly close (Figure 17), the inversion models for these two paths are more different than we would expect. However, it may be that very similar models would fit both sets of data just as well considering the errors in the data. From Figure 17 we also note that the HOG-HLW path is essentially the first half of the HOG-SHI path. This fact should be taken into account.

In summary, the models presented in this section represent the results of the initial inversion of the dispersion data. With the exception of the Love-Rayleigh inconsistency for the HOG-AAE path which requires more study, these data are fit quite well by smooth and reasonable crust and upper mantle models. The next step is to introduce as a kind of side constraint the requirement that the models present a coherent picture of the structure in North Africa. This will lead to our final models for the paths studied.

5.5 SEISMOGRAM SYNTHESIS

At this point in our study of surface waves from SAPHIRE, synthetic seismograms generated from our inversion models serve mainly as a check on our data analysis and inversion results, and as a test of whether the observed waveforms are explainable by plane-layer propagation effects. Before we can analyze the observed amplitudes and infer source parameters, we must resolve certain problems with propagation effects and obtain a more consistent set of path models.

Figure 26 compares the observed SAPHIRE seismograms from Figure 18 to synthetic surface waves generated from one of the inversion models for each path. In each comparison,

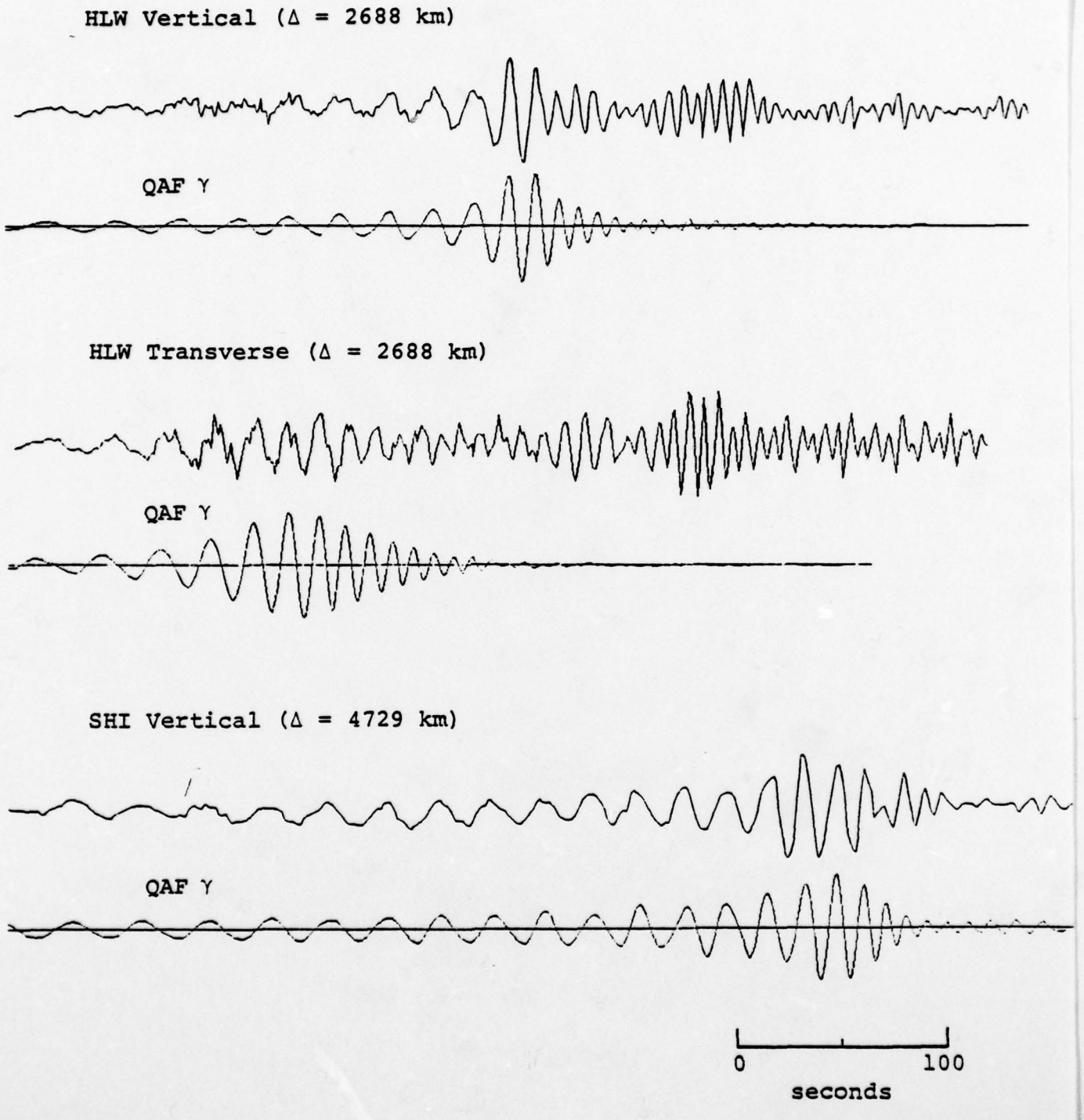

Figure 26. The synthetic seismograms computed from the inversion models are compared to the observed seismograms from each of the five stations. For AAE and NAI, the synthetics obtained from two $\gamma(\omega)$ models (QAF and QAAE) are shown.

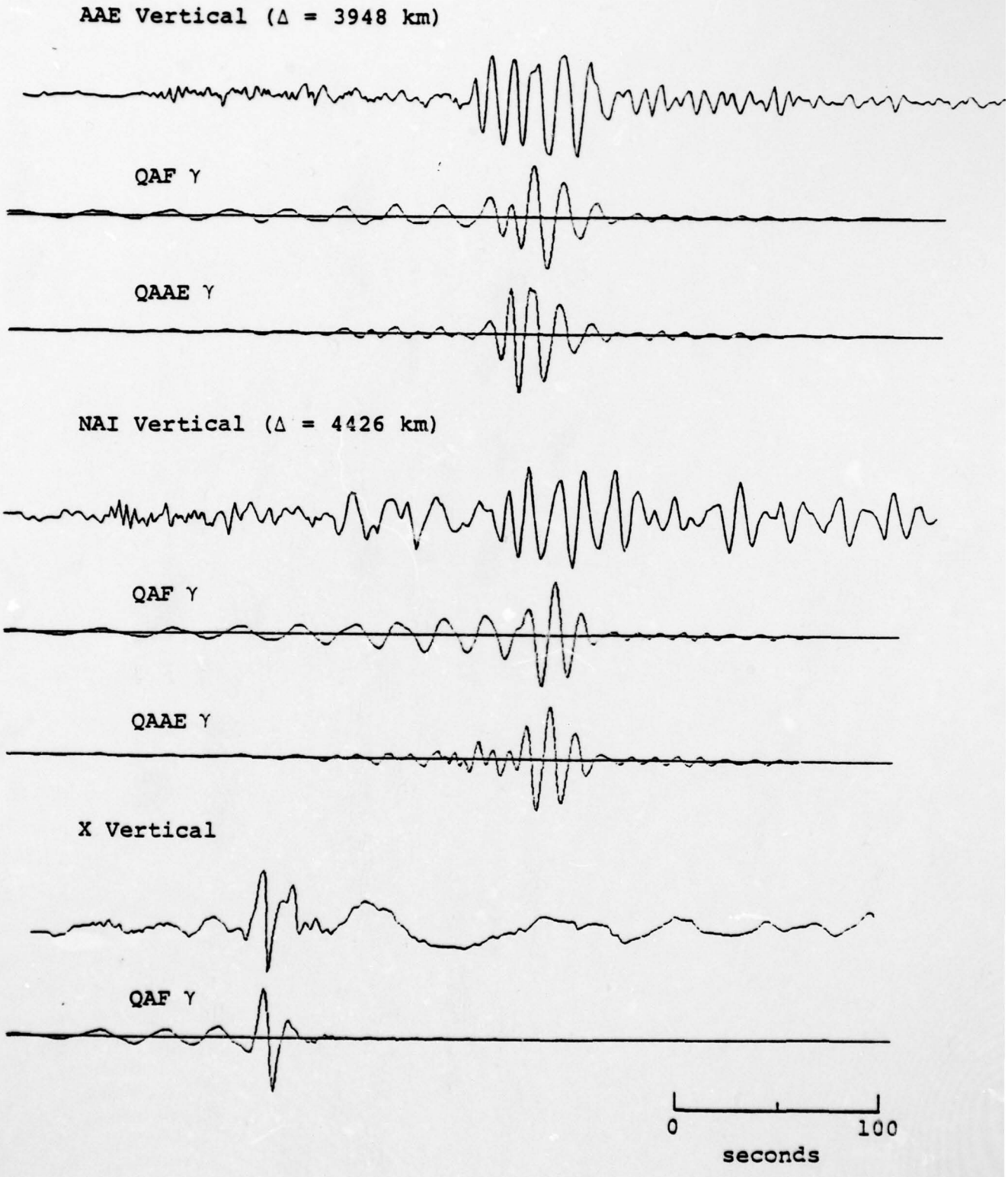

Figure 26. (continued)

the observed and synthetic seismograms are correctly aligned in time. The AAE transverse component was not synthesized since we did not fit the AAE Love wave dispersion data.

We match the waveforms of the HLW, SHI and X seismograms very well. (The latter part of the observed HLW transverse component is probably the Rayleigh wave.) Our HLW vertical synthetic does not match the short period wave group arriving about 75 seconds after the peak, but this may be due to the attenuation model. Otherwise the agreement is good in a large time window.

The agreement between the observed and synthetic seismograms for AAE and NAI is much poorer. Because of the Airy phases in the AAE and NAI dispersion curves (Figures 23 and 24), the shape of these seismograms is very dependent on the interference of different frequency arrivals. Therefore, we must look more carefully at how accurately we have determined and fit the dispersion for these two paths. This is particularly important for the HOG-NAI path, since the NAI seismogram shows evidence of contamination by noise or multipathing.

The attenuation function $\gamma(\omega)$ may also have a big effect on the interference in the AAE and NAI seismograms. To illustrate this, we show two synthetics for these stations, for the two γ models labeled QAF and QAAE. The two γ models are compared in Table 8. The QAF model is based on an average continental attenuation curve (Tryggvason, 1965). This attenuation model was also used to generate the HLW, SHI and X synthetics. The QAAE γ model was adjusted to improve the fit to the amplitude spectrum of the AAE seismogram and is not necessarily a reasonable model of anelastic surface-wave attenuation. In Figure 26 we can see how both the amplitude and frequency content of the AAE and NAI synthetics can depend on γ.

TABLE 8

GAMMA MODELS USED IN SURFACE-WAVE SYNTHESIS

	γ_R (10^4/km)		γ_L
Period	QAF	QAAE	QAF
40	0.63	4.00	1.65
30	0.591	4.00	1.30
25	0.597	4.00	0.98
20	0.70	3.15	0.85
18	0.84	2.59	1.03
16	1.10	1.96	1.40
14	1.40	1.25	1.90
12	1.80	0.83	2.90
10	3.00	2.20	6.00
8	8.00	4.44	15.40
6	12.00	6.50	22.20
4	20.00	9.00	36.00

We are not now certain whether reasonable plane-layered velocity and attenuation models can account for the waveforms of the AAE and NAI seismograms. The proximity of a major tectonic feature, the African rift, may play an important role.

In summary, the synthetic seismograms computed with a simple source show good agreement with the observations at most of the stations, though further work is required. As we mentioned at the end of Section 5.4, we first need to complete our development of consistent structural models for this region. We also need to develop reasonable and consistent Q or γ models to account for the attenuation. Having done this we will use the comparison between observed and synthetic seismograms to infer the source characteristics.

REFERENCES

Archambeau, C. B., D. G. Harkrider, and D. V. Helmberger (1974), "Studies of Multiple Seismic Events," California Institute of Technology, Final Contract Report (Draft) prepared for U. S. Arms Control and Disarmament Agency.

Bache, T. C., Cherry, J. T., Lambert, D. G., Masso, J. F. and J. M. Savino (1976), "A Deterministic Methodology for Discriminating Between Earthquakes and Underground Nuclear Explosions," Systems, Science and Software Report SSS-R-76-2925, July 1976.

Bache, T. C., J. M. Masso and B. F. Mason, "Theoretical Body and Surface Wave Magnitudes for Twelve Numerically Simulated Cratering Explosions," Systems, Science and Software Report SSS-R-77-3119, submitted to ARPA, VSC, January 1977.

Bache, T. C. and J. F. Masso (1978), "Analysis of Two Decoupled Explosion Simulations," Systems, Science and Software Technical Report (Draft), SSS-R-78-3627, April 1978.

Bache, T. C., W. L. Rodi and D. G. Harkrider (1978), "Crustal Structures Inferred from Rayleigh Wave Signatures of NTS Explosions," to appear in BSSA.

Bakun, W. H. and L. R. Johnson (1970), "Short Period Spectral Discriminants for Explosions," Geophys. J. R. Astr. Soc., 22, pp. 139-152.

Barazangi, M., W. Pennington and B. Isacks (1975), "Global Study of Seismic Wave Attenuation in the Upper Mantle Behind Island Arcs Using pP Waves," J. Geophys. Res., 80, pp. 1079-1092.

Basham, P. W., D. H. Weichert and F. M. Anglin (1970), "An Analysis of the 'Benham' Aftershock Sequence Using Canadian Recordings," J. Geophys. Res., 75, pp. 1545-1556.

Burridge, R. and L. Knopoff (1964), "Body Force Equivalent for Seismic Dislocation," BSSA, 54, pp. 1875-1888.

Cherry, J. T., T. C. Bache and D. B. Patch (1975), "The Teleseismic Ground Motion Generated by an Explosion in a Tunnel and Its Effect on the M_s/m_b Discriminant," Systems, Science and Software Final Contract Report to the Defense Nuclear Agency, DNA 3645F, May 1975.

Cherry, J. T., T. C. Bache, W. O. Wray and J. F. Masso (1976), "Teleseismic Coupling from the Simultaneous Detonation of an Array of Nuclear Explosions," Systems, Science and Software Technical Report SSS-R-76-2865, February 1976.

Cisternos, A., C. Betancourt and A. Leiva (1973), "Body Waves in a Real Earth," Bull. Seism. Soc. Am., 63, pp. 145-156.

Clayton, R. and B. Engquist (1977), "Absorbing Boundary Conditions for Acoustic and Elastic Wave Equations," BSSA, 67, pp. 1529-1540.

Engquist, B. and A. Majda (1977), "Absorbing Boundary Conditions for Numerical Simulation of Waves," Proc. Natl. Acad. Sci. U.S.A., 74, pp. 1765-1766.

Gumper, F. and P. W. Pomeroy (1970), "Seismic Wave Velocities and Earth Structure on the African Continent," BSSA, 60, pp. 651-668.

Harkrider, D. G. (1964), "Surface Waves in Multilayered Media I. Rayleigh and Love Waves from Buried Sources in a Multilayered Elastic Half-Space," BSSA, 54, pp. 627-679.

Harkrider, D. G. (1970), "Surface Waves in Multilayered Media II. Higher Mode Spectra and Spectral Ratios from Point Sources in Plane-Layered Earth Models," BSSA, 60, pp. 1937-1987.

Knopoff, L. and J. W. Schlue (1972), "Rayleigh Wave Phase Velocities for the Path Addis Ababa-Nairobi," R. W. Girdler (editor), East African Rifts, Tectonophysics, 15(1/2), pp. 157-163.

Knopoff, L., F. Schwab and E. Kausel (1973), "Interpretation of Lg," Geophys. J. R. Astr. Soc., 33, pp. 389-404.

Knopoff, L., F. Schwab, K. Nakanishi and F. Chang (1974) "Evaluation of Lg as a Discriminant Among Different Continental Crustal Structures," Geophys. J. R. Astr. Soc., 39, pp. 41-70.

Lacoss, R. T. (1969), "A Large-Population LASA Discrimination Experiment," Technical Note 1964-24, Lincoln Laboratory, Lexington, Massachusetts.

Lambert, D. G. and T. C. Bache (1977), "Identification of Individual Events in a Multiple Explosion from Teleseismic Short Period Body Wave Recordings," Systems, Science and Software Topical Report submitted to ARPA, SSS-R-78-3421, October 1977.

Panza, G. F. and G. Calcagnile (1975), "Lg, Li and Rg from Rayleigh Modes," Geophys. J. R. Astr. Soc., 40, pp. 475-487.

Panza, G. F., F. Schwab and L. Knopoff (1972), "Channel and Crustal Rayleigh Waves," Geophys. J. R. Astr. Soc., 30, pp. 273-280.

Savino, J. M. and C. B. Archambeau (1974), "Discrimination of Earthquakes from Single and Multiple Explosions Using Spectrally Defined Event Magnitudes," Trans. Amer. Geophys. Union, EOS, (Abstract), 56, pp. 1148.

Savino, J. M., T. C. Bache, J. T. Cherry, K. G. Hamilton, D. G. Lambert and J. F. Masso (1975), "Application of Advanced Methods for Identification and Detection of Nuclear Explosions from the Asian Continent," Systems, Science and Software Semi-Annual Technical Report SSS-R-76-2792, December 1975.

Searle, R. C. and P. Gouin (1971), "An Analysis of Some Local Earthquake Phases Originating Near the Afar Triple Junction," BSSA, 61, pp. 1060-1071.

Tryggvason, E. (1965), "Dissipation of Rayleigh Wave Energy," J. Geophys. Res., 70.

von Seggern, D. H. and R. R. Blandford (1977), "Observed Variation in the Spectral Ratio Discriminant from Short-Period P Waves," Teledyne Geotech Report SDAC-TR-76-12, September.

Watson, G. N. (1944), "A Treatise on the Theory of Bessel Functions," Cambridge University Press.